WAVE, TIDAL, AND SEASONAL DYNAMICS OF GROUNDWATER FLOW, SALTWATER-FRESHWATER MIXING, AND REACTIVE TRANSPORT IN BEACH AQUIFERS

by

James W. Heiss

A dissertation submitted to the Faculty of the University of Delaware in partial fulfillment of the requirements for the degree of Doctor of Philosophy in Geology

Winter 2017

WAVE, TIDAL, AND SEASONAL DYNAMICS OF GROUNDWATER FLOW, SALTWATER-FRESHWATER MIXING, AND REACTIVE TRANSPORT IN BEACH AQUIFERS

by

James W. Heiss

Approved: ____
Neil Sturchio, Ph.D.
Chair of the Department of Geological Sciences

Approved: ____
Mohsen Badiey, Ph.D.
Acting Dean of the College of Earth, Ocean, and Environment

Approved: ____
Ann L. Ardis, Ph.D.
Senior Vice Provost for Graduate and Professional Education

I certify that I have read this dissertation and that in my opinion it meets the academic and professional standard required by the University as a dissertation for the degree of Doctor of Philosophy.

Signed: ____

Holly A. Michael, Ph.D.
Professor in charge of dissertation

I certify that I have read this dissertation and that in my opinion it meets the academic and professional standard required by the University as a dissertation for the degree of Doctor of Philosophy.

Signed: ____

William J. Ullman, Ph.D.
Member of dissertation committee

I certify that I have read this dissertation and that in my opinion it meets the academic and professional standard required by the University as a dissertation for the degree of Doctor of Philosophy.

Signed: ____

Thomas E. McKenna, Ph.D.
Member of dissertation committee

I certify that I have read this dissertation and that in my opinion it meets the academic and professional standard required by the University as a dissertation for the degree of Doctor of Philosophy.

Signed: ____

Michel Boufadel, Ph.D.
Member of dissertation committee

ACKNOWLEDGMENTS

I would like to first thank my advisor, Dr. Holly Michael, for teaching me how to explore the natural world. Your patience and insight guided me on a remarkable journey of scientific and self-discovery with a destination that was as rewarding as the path itself. The enthusiasm and intelligence I witnessed during our conversations was inspiring and I am grateful for your all of your support, ideas, and guidance along the way.

To my committee members, Dr. William Ullman, Dr. Thomas McKenna, and Dr. Michel Boufadel, your ideas, suggestions, and comments improved these projects greatly. Bill, your fervor never failed to jumpstart my ambition. Thank you for your explanations and insightful discussions on the phone, in your office, and on the beach.

I am indebted to my lab group for their support, discussions, and encouragement both in and outside of the office, especially Chris Russoniello, Mahfuz Khan, and Kyra Kim. Mahfuz and Kyra, I cannot thank you enough for talking me through obstacles and for your emotional support. Chris, your involvement and influence on these studies has been tremendous, and I am incredibly grateful for your help, input, and friendship over the years.

To everyone who joined me in the field, I would still be on the beach if it were not for your help. Aline Pieterse, Thijs Lanckriet, Chris Russoniello, Mahfuz Khan, Kyra Kim, Lindsey Byron, Adam Dejean, Veronica Citerone, Hannah Billian, Jillian

McKenna, Nathan Veale, Kim Aviado, Dan Hubacz, Jill Harig, and Shaun Smith, thank you for donating so much of your time.

Mom and dad, thank you for always listening, your encouragement, and for supporting me in all walks of life.

TABLE OF CONTENTS

LIST OF TABLES

LIST OF FIGURES

ABSTRACT

Nutrient, metal, and carbon fluxes in submarine groundwater discharge can adversely impact the chemistry of nearshore marine ecosystems. These solutes can undergo biogeochemical transformations in saltwater-freshwater mixing zones that form when fresh groundwater flowing toward the sea meets with saline groundwater of marine origin in sandy beaches. This dissertation focuses on the driving mechanisms of flow, the time scales of mixing, and biogeochemical processes that are key in altering the fate and fluxes of nutrients prior to discharge to the sea.

A field and numerical modeling study investigated intertidal salinity dynamics in a sandy tidally-influenced beach aquifer across a wide range of temporal scales and hydrologic forcings. Seasonal variations in the terrestrial freshwater gradient were primarily responsible for controlling the shape and size of the intertidal saltwater-freshwater mixing zone, followed by spring-neap variability in tidal amplitude, and tidal stage. Intertidal salinities decreased as the seasonal freshwater hydraulic gradient increased in spring and winter, and increased as freshwater forcing decreased in summer. The effects of Hurricane Sandy and seasonal sea level anomalies on the subsurface salinity distribution were minor compared to seasonal freshwater forcing.

Coupled surface and subsurface measurements reveal for the first time the motion and areal extent of infiltration, recharge, and discharge zones at swash and tidal time scales under and across the beachface. Infiltration was controlled by the location of wave runup and occurred across a part of the beach widely accepted in literature to be a zone of groundwater discharge, while recharge occurred at both

swash and tidal time scales. The results demonstrate that identification of infiltration, recharge, and discharge zones can be achieved only through coupled measurements of the swash location and water content conditions in the beach. A more accurate conceptual model of groundwater-surface water interactions in the intertidal zone is developed that will require that sediment transport models be reevaluated to properly represent zones of groundwater-surface water exchange.

A variable-density groundwater flow and reactive solute transport model of a beach aquifer was used to investigate the influence of 5 physical factors, including tidal amplitude, freshwater flux, hydraulic conductivity, beach slope, and dispersivity on the biogeochemical reactivity of the intertidal zone for mixing-dependent and mixing-independent reactions, modeled as denitrification and sulfate reduction, respectively. A sensitivity analysis of nitrate and sulfate removal efficiencies demonstrates that tidal forcing promotes denitrification along the boundary of the intertidal saltwater circulation cell between 1 and 10 ppt. Denitrification increases with the size of the mixing zone, while sulfate supply is the main factor controlling sulfate reduction. The results reveal the type of beaches that are most chemically active and have the largest role in moderating chemical fluxes to the sea.

These studies demonstrate that hydrologic and biogeochemical processes interact across time and space, and that these interactions moderate chemical fluxes to the sea. Thus, the findings have important implications for managing marine ecosystems, and the recreational and economic resources they provide.

Chapter 1

INTRODUCTION

1.1 The Role of Beach Aquifers as a Biogeochemical Reactor

Submarine groundwater discharge (SGD) is an important transport pathway for chemicals entering the marine environment. Chemicals of terrestrial origin that enter coastal waters along groundwater flowpaths can adversely affect near-shore ecosystems and water quality. This is often the case when discharging groundwater contains high concentrations of nutrients and other chemical contaminants relative to surface water. Since nitrogen and phosphorous fluxes along this pathway often rival global river inputs [Slomp and Van Cappellen, 2004], SGD can lead to harmful algal blooms, anoxic conditions, habitat degradation, alter the structure of food webs [Paerl et al., 2003], and affect water quality [Simmons, 1992]. Nevertheless, a number of studies have identified zones of subsurface biogeochemical reactivity that can alter the fate of discharging chemicals [Moore, 1999; Ullman et al., 2003; Charette and Sholkovitz, 2002; Hays and Ullman, 2007; Santos et al., 2008; Loveless and Oldham, 2009; Santoro, 2009; Charbonnier et al., 2013]. These zones of reactivity serve as a chemical barrier by removing nutrients and other solutes in groundwater that would otherwise discharge to marine ecosystems. The formation of these zones is governed by hydrologic processes that bring together reactive solutes sourced from land and sea. Thus, understanding the hydrologic forcing mechanisms that result in mixing of terrestrial (fresh) and marine (saline) endmembers is needed to understand the biogeochemical role of sandy beaches in attenuating chemical loads from the subsurface to coastal waters.

1.2 Hydrologic Forcing Mechanisms at the Coastline

There are multiple hydrologic forcing mechanisms acting on coastal aquifers that form distinct zones of salinity in the subsurface. In this section the effects of these forcing mechanisms on the subsurface salinity distribution in coastal aquifers is discussed.

Groundwater salinity in nearshore aquifers is characterized by a Ghyben-Herzberg interface that forms due to the density difference between saltwater and freshwater [Hubbert, 1940]. Assuming static conditions, the depth of the Ghyben-Herzberg interface is related to the elevation of the water table and the density contrast between the fresh water and saltwater. This relationship assumes a sharp interface and predicts that the depth of the interface below mean sea level is 40x the elevation of the water table when the ocean salinity is 35 ppt. In real systems a terrestrial freshwater gradient drives groundwater flow from land to sea (Process 1; Figure 1.1), which drives mixing between terrestrially-derived fresh and marine-derived groundwater beneath the coastline, forming a dispersed lower saltwater-freshwater interface [Figure 1.1.; Cooper, 1959]. The density gradient across the interface establishes convective circulation of saltwater farther offshore (Process 2; Figure 1.1).

Transient forcing mechanisms in the intertidal and near-shore zones also drive seawater recirculation through coastal sediments. Oceanic forcing including tides [Ataie-Ashtiani et al., 2001; Michael et al., 2005; Robinson et al., 2006], wave set-up and set-down [Longuet-Higgins, 1983; Li et al., 1999; Boufadel et al., 2007; Xin et al., 2014], and wave swash [Xin et al., 2010; Bakhtyar et al., 2012; Geng, et al., 2014] form a shallow seawater recirculation cell beneath the intertidal zone, where saltwater infiltrates the upper swash zone and beachface and circulates downward and seaward before discharging at a point farther seaward. The circulation cell is characterized as a region of saline-brackish groundwater that overlies the region of seaward flowing fresh groundwater that discharges near the low tide mark (Figure 1.1).

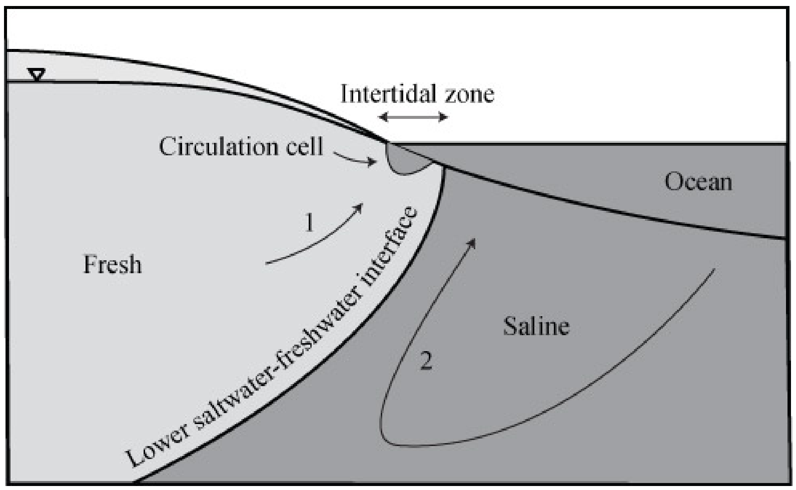

Figure 1.1 Terrestrial and density-driven flow in a coastal aquifer. Solid arrows represent flowpaths. Process 1 is terrestrially-derived fresh groundwater flow, Process 2 is density- driven circulation along the lower saltwater-freshwater interface. A circulation cell of saline-brackish groundwater overlies the region of seaward flowing fresh groundwater that discharges near the low tide mark.

Tidal oscillations drive saltwater through the intertidal circulation cell, altering flow dynamics and the salinity structure of the intertidal zone [Ataie-Ashtiani et al., 1999; Boufadel, 2000; Zhang et al., 2001; Ullman et al., 2003; Turner and Acworth, 2004; Urish and McKenna, 2004; Michael et al., 2005; Vandenbohede and Lebbe, 2005; Charette and Sholkovitz, 2006; Li et al., 2008; Henderson et al., 2009; Robinson et al., 2006, 2007a, 2007b; Kuan et al., 2012]. A number of these studies offer a snapshot of beach pore water salinity under the action of tides [e.g.Ullman, 2003; Turner and Acworth, 2004; Charette and Sholkovitz, 2006] with fewer providing insight into salinity variability over a tidal cycle [Ataie-Ashtiani et al., 1999; Robinson et al., 2007b; Henderson et al., 2009; Heiss and Michael, 2014]. Further, the intertidal salinity structure in beach aquifers and its response to hydrologic forcings at spring-neap [Robinson et al., 2007a; Abarca et al., 2013; Heiss and Michael, 2014] and seasonal [Santos et al., 2008; Heiss and Michael, 2014] time scales are less well understood. However, mixing between the terrestrial and marine endmembers at these timescales may be an important factor in influencing the fate of nutrients in nearshore aquifers.

Wave swash can also modify flow paths and the transport of solutes in nearshore aquifers [Li et al., 1999; Turner and Nielsen, 1997; Austin and Masselink, 2006; Boufadel et al., 2007; Xin et al., 2010; Steenhauer et al., 2011; Masselink and Turner, 2012; Heiss et al., 2014, 2015]. Swash-groundwater exchange can occur at the frequency of individual swash events across the saturated [e.g. Turner and Nielsen, 1997; Turner and Masselink, 1998; Butt, 2001; Heiss et al., 2015] and unsaturated [e.g. Austin and Masselink, 2006; Boufadel et al., 2007; Masselink and Turner, 2012; Turner and Masselink, 2012; Heiss et al., 2014] beachface. Unsaturated vertical infiltration has been shown to be responsible for water table oscillations in the swash zone [e.g. Austin and Masselink, 2006; Steenhauer et al., 2011; Masselink and Turner, 2012; Heiss et al., 2014]. Prior field studies have quantified swash-induced infiltration and discharge rates across the beachface in an effort to better understand the mechanisms controlling sediment transport. However, the location, areal extent, and motion of infiltration and discharge zones is also important for groundwater residence times and the mobility and degradation potential of labile organic carbon entering the beach aquifer. Thus, identifying and understanding the movement of zones of groundwater-surface water exchange at wave and tidal time scales on the exposed and submerged beachface will aid in determining reactive species entry points and transport paths, and ultimately the supply of organic carbon to the intertidal mixing zone and associated biogeochemical reactivity.

Flow paths, transport time scales, and mixing of fresh and saline groundwater are principle factors influencing the biogeochemical relevance of beach aquifer systems in recycling and removing nutrients and other contaminants prior to discharge. The flow and transport field that develops due to wave, tidal, and terrestrial freshwater forcing brings together terrestrially-derived and marine-derived groundwater that have contrasting geochemical characteristics. Mixing between these endmembers sets up redox gradients that lead to geochemical transformations the nearshore aquifer that depend on the hydrologic framework [Charette and Sholkovitz, 2002; Ullman et al., 2003; Slomp and Van Cappellen, 2004; Kroeger and Charette, 2008; Santos et al., 2009; Meile et al., 2010; McAllister et al., 2015]. Convective circulation [Process 1; Figure 1.1] driven by gravity and buoyant forces acting on porewater mixed by hydrodynamic dispersion along the lower freshwater-saltwater interface leads to long residence times and low levels of dissolved oxygen along circulating flow paths.. As a result, these waters tend to be anoxic and become more reducing along groundwater flow paths [Slomp and Van Cappellen, 2004]. In contrast, rapid circulation and flushing of near-surface porewater in the intertidal zone of sandy beaches by waves and tides can result in short residence times [e.g. Michael et al., 2005; Heiss and Michael, 2014] and oxic conditions [e.g. Robinson et al., 2009; Anwar et al., 2014; Charbonnier et al., 2013]. Once oxygen is consumed, mixing between the freshwater and seawater endmembers driven by tidal forcing can promote a reactive environment [McAllister et al., 2015] unlike that along the lower interface. Combined with a presence of reactive organic matter, hydrologic and geochemical conditions in beach aquifers have been shown to support high rates of nitrification [Ullman et al., 2003]. Beaches can also contain hotspots of denitrification where seawater, rich in organic matter, percolates downward to mix with through-flowing anoxic fresh groundwater with high concentrations of nitrate [Santos et al., 2008]. The results of these studies suggest that the driving mechanisms of flow, mixing, and solute and organic matter availability are important to controlling the type, spatial extent, and rates of biogeochemical processes occurring within these systems.

1.3 Broader Significance

A clearer understanding of the role of physical forcing mechanisms on groundwater flow, saltwater-freshwater mixing, and reactive transport in shallow coastal aquifers will be beneficial for developing management strategies that can be implemented to promote healthy marine ecosystems. Aquifer properties along with wave, tidal, and terrestrial forcing conditions control flow rates, residence times, dynamics of infiltration and discharge zones, and time scales of mixing between saltwater and freshwater. These factors directly control chemical reactivity. Because the forcing mechanisms control the surface and subsurface hydrology of the beach, they are central to the biogeochemical relevance of sandy beaches in altering the fate and fluxes of chemicals in discharging groundwater. If a more permeable beach aquifer promotes greater seawater infiltration across the intertidal zone and a larger saltwater-freshwater mixing zone, it may lead to a more favorable subsurface biogeochemical environment for redox reactions that attenuate meaningful quantities of contaminants that would otherwise enter nearshore marine ecosystems. Knowledge of the role of sandy beaches in altering the fate of contaminants prior to discharge will aid beach managers in predicting the ecological, environmental, and economic value of these unseen and underappreciated, yet nearly ubiquitous features of the world's coastline.

Sandy beaches and healthy nearshore waters have significant ecological, recreational, and economic value. Beaches attract millions of people for recreational purposes and often serve as an important revenue stream for local and state governments and act as a backbone to tourism-based economies. It is unsurprising, then, that beach closures set in place to protect human health from unnatural abundances of bacteria, viruses, and parasites in surface water can be detrimental to economies that rely on tourism. While many sources of chemical contaminants on the land surface that cause outbreaks of organisms harmful to human health can be identified with relative ease, similar contaminants can enter marine ecosystems along groundwater flow paths that pass through beach aquifers. Unlike the majority of sources of contaminants on land, fluxes of contaminants from the seabed are highly heterogeneous and diffuse and thus difficult to quantify. An important and necessary step in quantifying fluxes of chemicals from the seabed is to first understand how the mechanisms that drive flow and transport control chemical reactions that alter the fate of chemicals in discharging groundwater.

The overarching objective of this thesis is to demonstrate the effects of land-sea forcing on physical flow, transport, and biogeochemical processes in beach aquifers. Field investigations were used in combination with density-dependent numerical flow and reactive transport models to examine linkages between each of these processes. This thesis is organized as follows:

Chapter 2 presents results from a field and numerical modeling study that reveals the physical forcing conditions and time scales that are most responsible for controlling the structure and areal extent of the mixing zone between saltwater and freshwater in the intertidal zone of sandy beaches under tidal influence. Chapter 2 primarily focuses on the effects of tides and seasonal inland water table fluctuations on the salinity dynamics in the intertidal zone [Heiss and Michael., 2014].

Chapter 3 presents results from a field study demonstrating the extent to which saturated and unsaturated flow processes in the intertidal zone are coupled to swash and tidal forcing and provides new insight into the dynamics of infiltration, recharge, and discharge zones on beaches. Chapter 3 primarily deals with the effects of wave swash on groundwater-surface water interactions in the shallow beach [Heiss et al., 2015].

Chapter 4 presents results of a numerical modeling study that illustrates the importance of key physical factors in regulating the biogeochemical framework in sandy beaches subjected to tides. Chapter 4 links the physical processes of flow and transport with biogeochemistry, demonstrating the effects of tidal amplitude, hydraulic conductivity, freshwater flux, beach slope and dispersivity on contaminant reactivity and fluxes of biogeochemically active chemicals across the aquifer-ocean interface.

Chapter 5 synthesizes the results of chapters 2-4, discusses the findings in a broader context, and provides recommendations for future work.

REFERENCES

Abarca, E., H. Karam, H. F. Hemond, and C. F. Harvey (2013), Transient groundwater dynamics in a coastal aquifer: The effects of tides, the lunar cycle, and the beach profile, *Water Resour. Res.*, *49*, 1–16, doi:10.1002/wrcr.20075.

Ataie-Ashtiani, B., R. E. Volker, and D. A. Lockington (1999), Tidal effects on sea water intrusion in unconfined aquifers, *J. Hydrol*., 216, 17–31

Ataie-Ashtiani, B., R. E. Volker, and D. A. Lockington (2001), Tidal effects on groundwater dynamics in unconfined aquifers, *Hydrol. Processes*, 15(4), 655-669.

Anwar, N., C. Robinson, and D. A. Barry (2014), Influence of tides and waves on the fate of nutrients in a nearshore aquifer: Numerical simulations, *Adv. Water Resour.*, *73*(2014), 203–213, doi:10.1016/j.advwatres.2014.08.015.

Austin, M. J., and G. Masselink (2006), Swash–groundwater interaction on a steep gravel beach, *Cont. Shelf Res*., 20, 2503-2519.

Bakhtyar, R., D. A. Barry, and A. Brovelli (2012), Numerical experiments on interactions between wave motion and variable-density coastal aquifers, *Coastal Engineering*, 60, 95–108, http://doi.org/10.1016/j.coastaleng.2011.09.001.

Boufadel, M. C. (2000), A mechanistic study of nonlinear solute transport in a groundwater-surface water system under steady state and transient hydraulic conditions, *Water Resour. Res*., 36(9), 2549–2565.

Boufadel, M. C., H. Li, M. T. Suidan, and A. D. Venosa (2007), Tracer Studies in a Laboratory Beach Subjected to Waves, *J. Environ. Eng.*, 133, 722–732, doi:10.1061/(ASCE)0733-9372(2007)133:7(722).

Boufadel, M. C., Y. Xia, and H. Li (2011), Modeling solute transport and transient seepage in a laboratory beach under tidal influence, *Environ. Model. Softw.*, *26*(7), 899–912, doi:10.1016/j.envsoft.2011.02.005.

Butt, T., P. Russell, I. Turner (2001) The influence of swash infiltration–exfiltration on beach face sediment transport: onshore or offshore? *Coastal Engineering* 42, 35–52.

Charbonnier, C., P. Anschutz, D. Poirier, S. Bujan, and P. Lecroart (2013), Aerobic respiration in a high-energy sandy beach, *Mar. Chem.*, *155*, 10–21, doi:10.1016/j.marchem.2013.05.003.

Charette, M. A., and E. R. Sholkovitz (2002), Oxidative precipitation of groundwater-derived ferrous iron in the subterranean estuary of a coastal bay, Geophys. Res. Lett., 29(10), 1444, doi:10.1029/2001GL014512.

Charette, M.A., and E.R. Sholkovitz (2006), Trace element cycling in a subterranean estuary: Part 2. Geochemistry of the pore water, *Geochim. Cosmochim. Acta*, *70*(4), 811–826, doi:10.1016/j.gca.2005.10.019.

Cooper, H. H. (1959) A hypothesis concerning the dynamic balance of fresh water and salt water in a coastal aquifer, *Journal of Geophysical Research*, 64(4), 461-467.

Geng, X., Boufadel, M. C., Xia, Y., Li, H., Zhao, L., Jackson, N. L., & Miller, R. S. (2014), Numerical study of wave effects on groundwater flow and solute transport in a laboratory beach, *Journal of Contaminant Hydrology*, 165, 37–52. http://doi.org/10.1016/j.jconhyd.2014.07.001.

Hays, R. L., and W. J. Ullman (2007), Direct determination of total and fresh groundwater discharge and nutrient loads from a sandy beachface at low tide (Cape Henlopen , Delaware), *Limnol. Oceanogr.*, *52*(1), 240–247.

Heiss, J. W., and H. A. Michael (2014), Saltwater-freshwater mixing dynamics in a sandy beach aquifer over tidal, spring-neap, and seasonal cycles, *Water Resour. Res.*, *50*, 6747–6766, doi:10.1002/2014WR015574.

Heiss, J. W., J. A. Puleo, W. J. Ullman, and H. A. Michael (2015), Coupled surface-subsurface hydrologic measurements reveal infiltration, recharge, and discharge dynamics across the swash zone of a sandy beach, Water Resour. Res., 51, 8834–8853, doi:10.1002/2015WR017395.

Heiss, J. W., W. J. Ullman, and H. A. Michael (2014), Swash zone moisture dynamics and unsaturated infiltration in two sandy beach aquifers, *Estuar. Coast. Shelf Sci.*, *143*, 20–31, doi:10.1016/j.ecss.2014.03.015.

Hubbert, M. K. (1940) The theory of ground-water motion, Journal of Geoogy, 48(8), 785-944.

Henderson, R. D., F. D. Day-Lewis, E. Abarca, C. F. Harvey, H. N. Karam, L. Liu, and J. W. Lane (2009), Marine electrical resistivity imaging of submarine groundwater discharge: sensitivity analysis and application in Waquoit Bay, Massachusetts, USA, *Hydrogeol. J.*, *18*(1), 173–185, doi:10.1007/s10040-009-0498-z.

Kroeger, K. D., and M. A. Charette (2008), Nitrogen biogeochemistry of submarine groundwater discharge, *Limnol. Oceanogr.*, *53*(3), 1025–1039, doi:10.4319/lo.2008.53.3.1025.

Kuan, W. K., G. Jin, P. Xin, C. Robinson, B. Gibbes, and L. Li (2012), Tidal influence on seawater intrusion in unconfined coastal aquifers, *Water Resour. Res.*, *48*(2), 1–11, doi:10.1029/2011WR010678.

Li, L., D. A. Barry, F. Stagnitti, and J. Y. Parlange (1999), Submarine groundwater discharge and associated chemical input to the coastal sea, *Water Resources Research*, (35)11, 3253-3259.

Li, L., D. A. Barry, F. Stagnitti, J.-Y. Parlange, and D. S. Jeng (2000), Beach water table fluctuations due to spring-neap tides: Moving boundary effects, *Adv. Water Resour*., 23(8), 817–824, doi:10.1016/s0309-1708(00)00017-8.

Li, H., M.C. Boufadel, and J. W. Weaver (2008). Tide-induced seawater-groundwater circulation in shallow beach aquifers, *Journal of Hydrology*, 352, 211–224.

Longuet-Higgins, M. S. (1983), Wave set-up, percolation and undertow in the surf zone, Proceedings of the Royal Society of London. Series A, Mathematical, Physical and Engineering Sciences, 390(1799), 283-291, doi:10.1098/rspa.1983.0132.

Loveless, A.M., and C.E. Oldham (2009), Natural attenuation of nitrogen in groundwater discharging through a sandy beach, *Biogeochemistry*, *98*(1-3), 75–87, doi:10.1007/s10533-009-9377-x.

Masselink, G., and I. L. Turner (2012), Large-scale laboratory investigation into the effect of varying back-barrier lagoon water levels on gravel beach morphology and swash zone sediment transport, *Coast. Eng.*, *63*, 23–38, doi:10.1016/j.coastaleng.2011.12.007.

McAllister, S. M., J.M. Barnett, J.W. Heiss, A.J. Findlay, D.J. Macdonald, C.L. Dow, G.W. Luther, H. A. Michael, and C. S. Chan (2015), Dynamic hydrologic and biogeochemical processes drive microbially enhanced iron and sulfur cycling within the intertidal mixing zone of a beach aquifer, *Limnol. Oceanogr.*, *60*(1), 329–345, doi:10.1111/lno.10029.

Meile, C., W. P. Porubsky, R. L. Walker, and K. Payne (2010), Natural attenuation of nitrogen loading from septic effluents: Spatial and environmental controls., *Water Res.*, *44*(5), 1399–408, doi:10.1016/j.watres.2009.11.019.

Michael, H. A., Mulligan, A.E., and Harvey, C.F. (2005), Seasonal oscillations in water exchange between aquifers and the coastal ocean. Nature 436, 1145–1148.

Moore, W. S. (1999), The subterranean estuary: A reaction zone of ground water and sea water, Mar. Chem., 65, 111–125.

Paerl, H. W., L. M. Valdes, J. L. Pinckney, M. F. Piehler, J. Dyble, and P. H. Moisander (2003), Phytoplankton Photopigments as Indicators of Estuarine and Coastal Eutrophication, *Bioscience*, *53*(10).

Robinson, C., B. Gibbes, and L. Li (2006), Driving mechanisms for groundwater flow and salt transport in a subterranean estuary, *Geophys. Res. Lett*., 33, L03402, doi:10.1029/2005GL025247.

Robinson, C., B. Gibbes, H. Carey, and L. Li (2007a), Salt-freshwater dynamics in a subterranean estuary over a spring-neap tidal cycle, *J. Geophys. Res.*, *112*(C9), 1–15, doi:10.1029/2006JC003888.

Robinson, C., L. Li, and D. A. Barry (2007b), Effect of tidal forcing on a subterranean estuary, *Adv. Water Resour.*, *30*(4), 851–865, doi:10.1016/j.advwatres.2006.07.006.

Robinson, C., A. Brovelli,, D.A. Barry, and L. Li (2009), Tidal influence on BTEX biodegradation in sandy coastal aquifers, *Advances in Water Resources*, *32*(1), 16–28. doi:10.1016/j.advwatres.2008.09.008.

Santoro, A. E. (2009), Microbial nitrogen cycling at the saltwater–freshwater interface, *Hydrogeol. J.*, *18*(1), 187–202, doi:10.1007/s10040-009-0526-z.

Santos, I.R., Burnett, W.C., Chanton, J., Mwashote, B., Suryaputra, I G. N. A., Dittmar, T., (2008), Nutrient biogeochemistry in a Gulf of Mexico subterranean estuary and groundwater-derived fluxes to the coastal ocean. *Limnology and Oceanography* 53, 705-718, doi:10.4319/lo.2008.53.2.0705.

Simmons, G. M. (1992), Importance of submarine groundwater discharge (SGWD) and seawater cycling to material flux across the sediment/water interfaces in marine environments, *Mar. Ecol. Prog. Ser*., 84, 173–184.

Slomp, C. P. and P. Van Cappellen (2004), Nutrient inputs to the coastal ocean through submarine groundwater discharge: controls and potential impact, *Journal of Hydrology* 295:64-86.

Steenhauer, K., D. Pokrajac, T.O'Donoghue, and G. A. Kikkert (2011), Subsurface processes generated by bore-driven swash on coarse-grained beaches, J. Geophys. Res., 116, C04013, doi:10.1029/2010JC006789.

Turner, I. L., and R. I. Acworth (2004), Field measurements of beachface salinity structure using cross-borehole resistivity imaging, J. Coastal Res., 20(3), 753–760.

Turner, I. L., and G. Masselink (1998), Swash infiltration-exfiltration and sediment transport, *Journal of Geophysical Research*, 103 (C13), 30813–30824.

Turner, I. L., and G. Masselink (2012), Coastal gravel barrier hydrology — Observations from a prototype-scale laboratory experiment (BARDEX), *Coast. Eng.*, *63*, 13–22, doi:10.1016/j.coastaleng.2011.12.008.

Turner, I. L., and P. Nielsen (1997), Rapid water table fluctuations within the beach face: Implications for swash zone sediment mobility?, *Coastal Engineering*, 32(1), 45–59.

Ullman, W. J., B. Chang, D. C. Miller, and J. A. Madsen (2003), Groundwater mixing, nutrient diagenesis, and discharges across a sandy beachface, Cape Henlopen, Delaware (USA), *Estuarine, Coastal Shelf Sci*., 57, 539-52.

Urish, D., and T.E. McKenna (2004), Tidal effects on ground water discharge through a sandy marine beach, *Ground Water*, 42(7), 971-982.

Vandenbohede, A., and L. Lebbe (2005), Occurrence of salt water above fresh water in dynamic equilibrium in a coastal groundwater flow system near De Panne, Belgium, *Hydrogeol. J.*, *14*(4), 462–472, doi:10.1007/s10040-005-0446-5.

Xin, P., C. Robinson, L. Li, D. A. Barry, and R. Bakhtyar (2010), Effects of wave forcing on a subterranean estuary, Water Resour. Res., 46, W12505, doi:10.1029/2010WR009632.

Xin, P., S. S. J. Wang, C. Robinson, L. Li, Y.-G. Wang, D. A. Barry (2014), Memory of past random wave conditions in submarine groundwater discharge, *Geophysical Research Letters*, 41.

Zhang, Q., R. E. Volker, and D. A. Lockington (2001), Influence of seaward boundary condition on contaminant transport in unconfined coastal aquifers., *J. Contam. Hydrol.*, *49*(3-4), 201–215.

Chapter 2

SALTWATER-FRESHWATER MIXING DYNAMICS IN A SANDY BEACH AQUIFER OVER TIDAL, SPRING-NEAP, AND SEASONAL CYCLES

This work has been published as Heiss, J. W., and H. A. Michael (2014), Saltwater-freshwater mixing dynamics in a sandy beach aquifer over tidal, spring-neap, and seasonal cycles, *Water Resour. Res.*, 50, 6747–6766, doi:10.1002/2014WR015574.

ABSTRACT

The biogeochemical reactivity of sandy beach aquifers is closely linked to physical flow and solute transport processes. Thus, a clearer understanding of the hydrodynamics in the intertidal zone is needed to accurately estimate chemical fluxes to the marine environment. A field and numerical modeling study was conducted over a one-year timeframe to investigate the combined effects of tidal stage, spring-neap variability in tidal amplitude, and seasonal inland water table oscillations on intertidal salinity and flow dynamics within a tide-dominated micro-tidal sandy beach aquifer. Measured and simulated salinities revealed an intertidal saline circulation cell with a structure and cross-sectional mixing zone area that varied over tidal, spring-neap and seasonal timescales. The size of the circulation cell and area of the mixing zone were shown for the first time to be most affected by seasonal water table oscillations, followed by tidal amplitude and tidal stage. The intertidal circulation cell expanded horizontally and vertically as the inland water table declined, displacing the fresh discharge zone and lower interface seaward. Over monthly spring-neap cycles, the center of the circulation cell shifted from beneath the backshore and upper beachface

to the base of the beach. Salinity variations in the intertidal zone over semidiurnal tidal cycles were minimal. The dynamics of the circulation cell were similar in simulations with and without a berm. The highly transient nature of intertidal salinity over multiple time scales may have important implications for the types and rates of chemical transformations that occur in groundwater prior to discharge to the ocean.

2.1 Introduction

Surface water discharge to the sea has historically been thought to be the primary source of land-derived nutrients and other contaminants entering near-shore marine ecosystems. More recently however, submarine groundwater discharge (SGD) has been identified as an important transport pathway [Johannes, 1980; Simmons, 1992; Moore, 1996; Taniguchi et al., 2002; Moore et al., 2008]. SGD is composed of freshwater from terrestrial sources and seawater circulated across the aquifer-ocean interface. A significant proportion of total SGD discharges through intertidal and nearshore zones of beach aquifers [Li et al. 1999; Bokuniewicz et al., 2004; Robinson et al., 2007c], which are biogeochemically active mixing zones [Charette and Sholkovitz, 2002; Beck et al., 2007; Roy et al., 2013].

Groundwater flow and solute transport in coastal aquifers is influenced by multiple forcing mechanisms that operate over a wide range of temporal and spatial scales, leading to a complex and dynamic intertidal subsurface environment. There are four primary forcing mechanisms that affect freshwater-saltwater dynamics in coastal aquifers (Figure 2.1). Fresh groundwater exits the aquifer through a narrow discharge zone between the shoreline and the intersection of the lower interface and the seabed [Process 1, Figure 2.1; Glover, 1959]. The fresh discharge zone is bounded seaward by the lower interface and landward by an intertidal brackish-saline circulation cell [Robinson et al., 1998; Michael et al., 2005]. Saltwater-freshwater mixing along the lower interface creates a density gradient that drives convective saltwater circulation [Process 2, Figure 2.1; Cooper, 1959; Kohout, 1960]. In the intertidal zone, tidal and wave action drive seawater into the beach aquifer, forming a saltwater circulation cell above the zone of seaward-flowing freshwater [Processes 3 and 4, Figure 2.1; Lebbe, 1999; Boufadel et al., 2000; Robinson et al., 2006; Bakhtyar et al., 2012]. Resulting hydraulic head gradients cause seawater to circulate downward and seaward, discharging near the base of the beach [e.g., Michael et al., 2005; Robinson et al., 2006]. A saltwater-freshwater mixing zone forms along the perimeter of this intertidal circulation cell [e.g. Ullman et al., 2003; Turner and Acworth, 2004; Vandenbohede and Lebbe, 2005, Xin et al., 2010; Abarca et al., 2013].

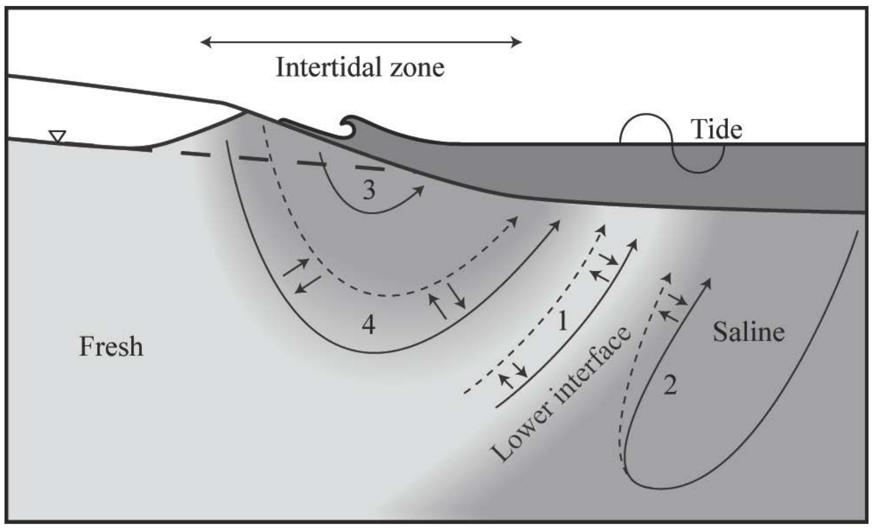

Figure 2.1. Forcing mechanisms of freshwater flow and saline groundwater recirculation in a coastal aquifer system. Solid and dashed lines represent flowpaths. Process 1 is freshwater discharge driven by the inland hydraulic gradient, Process 2 is density driven circulation along the lower saltwater-freshwater interface, Process 3 is saltwater exchange driven by wave set-up and swash infiltration, and Process 4 is tide-induced circulation. Flowpaths marked by a solid and dashed line represent conditions under a weak and strong inland hydraulic gradient, respectively.

The mixing of saltwater and freshwater caused by the processes discussed above creates zones of biogeochemical reactivity in the nearshore aquifer [Charette and Sholkovitz, 2002; Kroeger and Charette, 2008; Spiteri et al., 2008; Robinson et al., 2009]. These zones have implications for the fate of land-derived contaminants discharging to coastal surface waters [see review in Slomp and Van Cappellen, 2004], including transformation of nutrients prior to discharge [Bratton et al., 2004; Kroeger and Charette, 2008; Santos et al., 2008; Santoro, 2010; Charbonnier et al., 2013]. The biogeochemical processes are closely tied to the subsurface salinity distribution in the intertidal zone [Ullman et al., 2003; Charette and Sholkovitz, 2006]. Thus, a more comprehensive understanding of the dynamics and size of the mixing zone and the variability of discharge caused by both marine and terrestrial driving forces will improve prediction of chemical fluxes to the marine environment through SGD.

The saltwater circulation cell has been observed in a range of field settings under a variety of forcing conditions. The majority of previous field observations provide insight into the geometry and size of the circulation cell at one point in time [Ullman et al., 2003; Turner and Acworth, 2004; Michael et al., 2005; Charette and Sholkovitz, 2006; Robinson et al., 2006; Gibbes et al., 2007]. Other studies reveal that intertidal salinity is sensitive to tidal stage over a tidal cycle [e.g. Henderson et al., 2009; Befus et al., 2013], tidal amplitude [e.g. Robinson et al., 2007a; Abarca et al., 2013], and precipitation [e.g. Santos et al., 2008; Li et al., 2009; Jun et al., 2013]. Spring-neap variability in tidal amplitude has been shown to affect the structure of the circulation cell more than tidal stage [i.e. Robinson et al., 2007a], but the response of the circulation cell to seasonal oscillations in freshwater inflow has not been observed in the field.

The transient nature of the circulation cell when forced with tides has been simulated numerically [Boufadel, 2000; Vandenbohede and Lebbe, 2005; Robinson et al., 2006; Werner and Lockington, 2006; Li et al., 2008; Boufadel et al., 2011; Kuan et al., 2012]. Simulation results indicate that intertidal salinity can vary with tidal stage [Li et al., 2008] and is dependent on the amplitude of a sinusoidal tide [Robinson et al., 2007b]. Changes in tidal amplitude over a spring-neap cycle have also been shown to affect the structure of the circulation cell [Robinson et al., 2007a; Abarca et al., 2013]. Robinson et al. [2007b] and Kuan et al. [2012] showed that the freshwater flux is an important control on the salinity distribution under a semidiurnal tide with a steady head or freshwater flux at the landward boundary. However, transient changes in landward gradient have not been investigated numerically. While the dynamic nature of these systems is becoming clearer, the forcing conditions (i.e. tidal stage, diurnal variability in tidal amplitude, changes in tidal amplitude over a spring-neap cycle, and seasonality in the inland freshwater gradient) have yet to be combined into a continuous numerical model of flow and solute transport to understand how the physical processes interact to affect salinity and flow in the coastal aquifer.

The goal of this study is to identify the physical forcing conditions and time scales that are most important for controlling the structure and areal extent of the intertidal salinity distribution. The forcing conditions that we consider are: 1) tidal stage, 2) spring-neap variability in tidal amplitude, and 3) seasonal fluctuations in the inland water table. The effect of these processes on mixing are examined in the field along a shore-perpendicular transect of multilevel sampling wells. A density-dependent numerical model of groundwater flow and salt transport in a beach aquifer is developed to further explore the dynamics. We also investigate the significance of berm overtopping in modifying the structure and spatial extent of the upper circulation cell. The experimental and simulation results demonstrate the transient response of the intertidal mixing zones and SGD over these time scales.

2.2 Study Area Description and Methodology

2.2.1 Study Area

This study was conducted in the intertidal zone of a micro-tidal sandy beach that has been the focus of a number of hydrologic and geochemical studies [e.g., Miller and Ullman, 2004; Hays and Ullman, 2007; Heiss et al., 2014; Figure 2.2]. Cape Henlopen is a sandy spit with a regressive sequence; 12 to 18 meters of very coarse sands, pebbly sands, and gravels overlie marine silts and clays. The morphology of the beach consists of a dune, a 21 m wide backshore, a 14 m wide beachface with a 1:9 slope, and a broad tidal sandflat. A berm crest separates the backshore from the beachface, leading to a low lying area in the backshore (Figure 2.3).

The study site is partially protected by offshore breakwaters and therefore experiences little wave action except during storms. Tides are semidiurnal with a range of 1.42 m between MLLW and MHHW (NOS tidal station 8557830, Lewes, Delaware). Tidal range varies from approximately 2.0 at spring tides to 0.9 m at neap tides. Surface water salinity in the bay is typically ~28 ppt year-round based on monthly surface water measurements, whereas seawater on the ocean side of the spit is 35 ppt.

Hydrogeological characteristics of the study site were determined from sediment samples. Grain size analyses conducted using standard sieving procedures indicate that the beach is composed of predominantly coarse sand with grain sizes ranging from 540 – 668 μm. Measured hydraulic conductivity values from constant head permeameter tests ranged from 27.6 to 30.2 m/d. The hydraulic conductivity of the beach based on the effective grain size and the U.S. Bureau of Reclamation formula [Vukovic and Soro, 1992] is 30.2 m/d, consistent with the permeameter measurements.

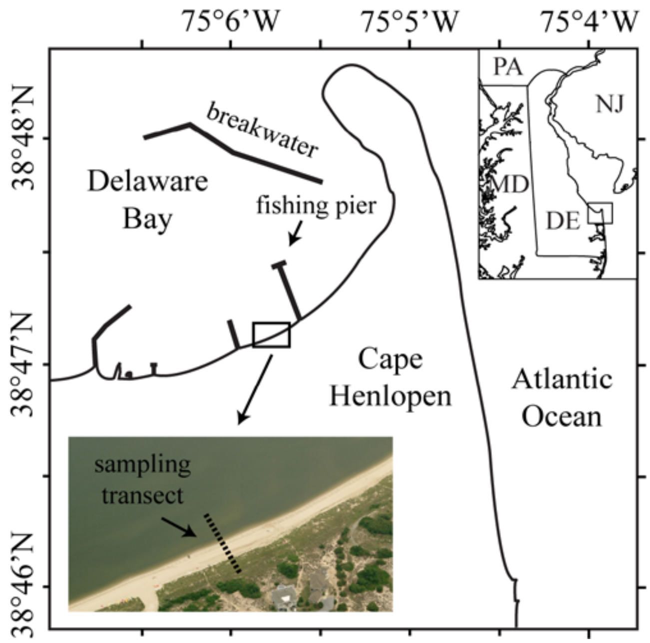

Figure 2.2. Study area and sampling transect

2.2.2 Field Measurements

Pore water was sampled for salinity along a shore-perpendicular transect of ten multilevel samplers. The samplers were constructed from three to five sections of 7 mm OD polyethylene tubing mounted to a 13 mm OD PVC pipe. Each section of tubing was screened over 3 cm and attached to the PVC pipe at depth intervals ranging from 0.5 m to 1.0 m. The samplers were installed along the intertidal transect into the beach aquifer, which we consider to extend horizontally from the dune to the base of the beachface, and vertically from the sand surface to the first confiding unit (Figure 2.3).

Pore water was sampled for salinity over a range of time scales. A profile was obtained 9 times over a tidal cycle, on average every 1.6 hours on 17 November 2012. Pore water was also collected 7 times over a lunar synodic month (29.5 days from new moon to new moon) on average every 4.6 days from 17 November to 14 December 2012 to assess spring-neap variability. Samples were collected 14 times over one year from 7 May 2012 to 7 May 2013 on average every 27 days, to examine seasonal variability in salinity. An additional salinity profile was taken on 30 October 2012, one day following the landfall of Hurricane Sandy 90 km north of the site. Pore water was sampled during the same tidal cycle and phase (at low tide during monthly spring tides) to reduce variability caused by tidal fluctuations and changes in tidal amplitude over spring-neap cycles.

The sampling procedure began with the farthest landward sampler and continued seaward along the transect, ending on the sandflat for a total of 45 pore water samples. Several tube volumes of pore water were pumped from each sample tube using a peristaltic pump before sample collection. A complete profile took no longer than 30 minutes to complete and is assumed representative of groundwater salinity at one point in time. Salinity was measured as electrical conductivity (YSI EC300) and is reported as ppt.

A conservative tracer solution was injected into the beach at the high tide mark on 28 February 2012 during high tide to determine the residence time and velocity of circulating saltwater for model calibration. The 0.18 M KBr tracer solution was designed to have the same 1.022 Kg/L density as the bay water (22 g KBr + 1 L deionized H2O). The injection took place at the shallowest port at multilevel sampler 3 prior to the tide inundating the sand surface above the injection point and continued until high tide, lasting approximately 30 minutes. Pore water was sampled twice daily from all 45 ports for 7 days for a total of 14 sample times. Bromide concentration was measured with a bromide electrode and the mV output readings were converted to concentration using a calibration curve created from molar standards. The standards were prepared by diluting the 0.18 M solution with bay water and groundwater over a range of expected salinities.

Hydrologic and meteorological data were recorded on each sampling date. The elevation of the water table 33 m behind the dune (herein referred to as the “dune water table”) was recorded at 15 minute intervals over the one-year monitoring period. The water table measurements were used to indicate changes in the inland hydraulic gradient, defined as the gradient between the dune well and the shoreline. Tide elevations at the study site were determined from the nearby Lewes, DE tide gauge station located 1 km east of the transect. Comparison of the NOS gauge station data with tide levels measured at the transect indicate that there is no time lag or amplitude variation in the tidal signal between the gauge station and the study site. Daily rainfall at the Rehoboth Beach weather station 8 km south of Cape Henlopen was used as a proxy for precipitation at the study site.

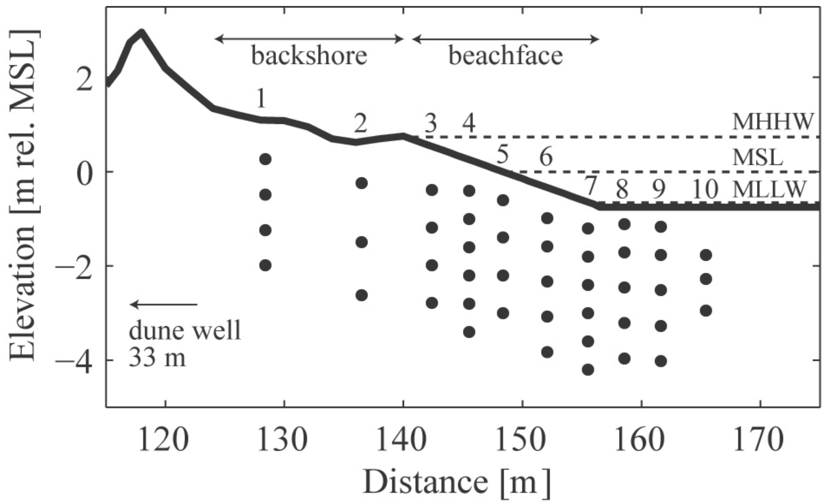

Figure 2.3. Cross section of sampling transect showing beach morphology and distribution of sampling ports. Distance is meters from landward model boundary.

2.2.3 Numerical Model

A variable-density groundwater flow and solute transport model was developed to support the interpretations of instantaneous observations and provide insight into the continuous response of the beach aquifer to tidal variations and seasonally variable inland freshwater forcing. The density-dependent groundwater flow and solute transport code SEAWAT (Langevin et al., 2008) was used to perform the simulations. The coupled flow and solute transport governing equations in SEAWAT are solved using a cell-centered finite difference approximation. The model represented a 2-D cross-section of the unconfined coastal aquifer at Cape Shores. The grid was non-uniform with higher horizontal discretization in the intertidal zone (0.3 m) where higher flow rates and concentration gradients occurred. Sensitivity tests showed that the numerical solution was independent of the grid discretization.

The model domain extended 50 m seaward of the beachface-MSL intersection and 150 meters landward (Figure 2.4). The aquifer extended 15 m below the beach surface to the first silt-clay confining unit [Kraft, 1971]. The beachface and backshore profile used in the model was the average of four profiles that were measured quarterly. The profiles varied by up to 25 cm with the largest differences occurring in the backshore between summer and winter.

2.2.3.1 Boundary Conditions

The boundary conditions used in the model were chosen to mimic natural forcing conditions. The landward boundary was set as a time-varying head boundary (Dirichlet boundary; Figure 2.4) using four stress periods to represent seasonal water table fluctuations (Figure 2.5b). The amplitude of the head fluctuation at the landward boundary was adjusted until the simulated seasonal trend in head at the dune well closely matched the measured seasonal trend in head at that location. The measured and simulated seasonal trends were calculated by fitting a first degree polynomial to the head data (Figure 2.5b). The period of the oscillating landward boundary repeated each year; this was consistent with field observations which showed similar heads during May-June 2012 and May-June 2013. The top, bottom, and seaward boundaries were set as no flow (Figure 2.4). Tidal forcing was simulated along the aquifer-ocean interface using the Periodic Boundary Condition (PBC) package [Post, 2011]. The PBC package was used to allow seepage face development along the aquifer-ocean interface and to apply a multiple-constituent tidal signal to the interface nodes as a time-varying Dirichlet boundary condition. The five tidal constituents with the greatest amplitude at our site according to the NOAA tidal station were used to develop a synthetic tidal signal to match the tide over the one-year sampling period.

The constituents used to generate the signal are the principle lunar semidiurnal (M2), principle solar semidiurnal (S2), larger lunar elliptic semidiurnal (N2), and the lunar diurnal constituents (Table 2.1;K1 and O1). The following prediction formula was used:

$$h_t = h_o + \sum_{i=1}^{5} A_i \cos(\omega_i t - \theta_i) \tag{2.1}$$

where h_t (m rel. MSL) is the predicted tidal elevation, h_o (m) is the reference water level (in this case MSL), A_i (m) is the amplitude, ω_i ($\omega_i = \frac{2\pi}{T}$) is the frequency in rad s^{-1}, and θ_i (rad) is the phase of each tidal constituent, i . The measured and predicted tides are shown in Figure 2.5c and d, respectively. The deviation between the predicted and measured tides (average of 15 cm) is due to weather conditions that are not taken into account by the predictions, which are based only on astronomical factors.

Table 2.1. Tidal constituents used in the fitting equation.

Name	Amplitude [m]	Phase [rad]	Frequency [rad s^{-1}]	Description
M_2	0.616	0.543	1.41×10^{-4}	principle lunar semidiurnal
S_2	0.108	0.991	1.45×10^{-4}	principle solar semidiurnal
N_2	0.134	0.183	1.38×10^{-4}	larger lunar elliptic semidiurnal
K_1	0.103	3.520	7.29×10^{-5}	lunar diurnal
O_1	0.074	3.292	6.76×10^{-5}	lunar diurnal

The transport boundary condition along the aquifer-ocean interface was zero-concentration gradient along the boundary for outward flow and a constant concentration of 28 for inward flow. The salinity of inflowing water was thus equal to that of the surface water and the salinity of the discharging groundwater was equal to the concentration of groundwater in the adjacent cell. A constant concentration of 0 was set along the landward vertical boundary, and zero mass flux across the no-flow boundaries.

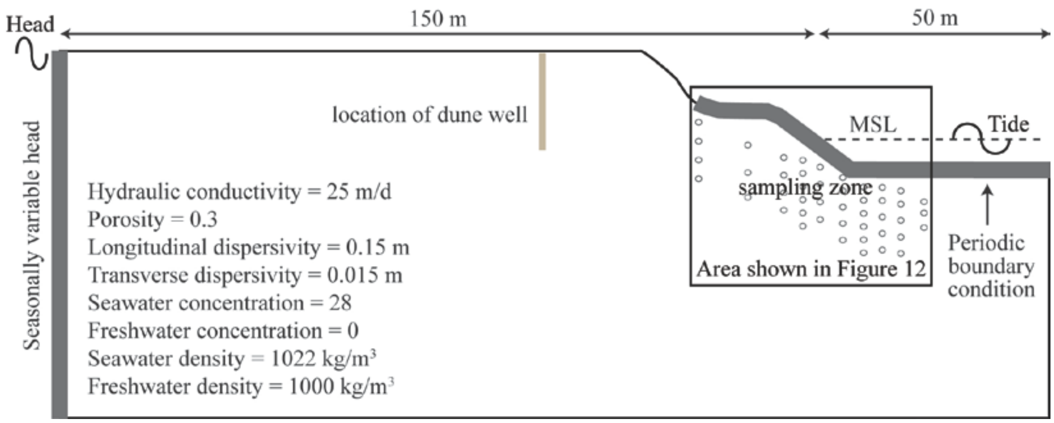

Figure 2.4. Model domain, boundary conditions, aquifer parameters, and sampling zone. Thin gray lines are no-flow boundaries.

2.2.3.2 Model Calibration

Model calibration was performed by manually adjusting aquifer parameters, including hydraulic conductivity, porosity, and longitudinal and transverse dispersivity until simulated hydraulic heads and concentrations during the one-year simulation period and flow velocities during the tracer test matched the field measurements well. The aquifer parameters used in the model are shown in Figure 2.4. The calibrated hydraulic conductivity of 25 m/d is close to the range of measured hydraulic conductivity (27.6 - 30.2 m/d).

2.3 Results and Discussion

2.3.1 Field Observations

2.3.1.1 Dune Water Table

Hydraulic head at the dune responded to changes in tidal stage, tidal amplitude, precipitation events, and seasonal variability in recharge (Figure 2.5a and b). Over a tidal cycle, the dune water table typically fluctuated between 5 and 10 cm depending on the amplitude of the tide. The water table fluctuated 10-25 cm over monthly spring-neap cycles and up to 100 cm in response to precipitation events. On the seasonal time scale, the water table oscillated by about 30 cm.

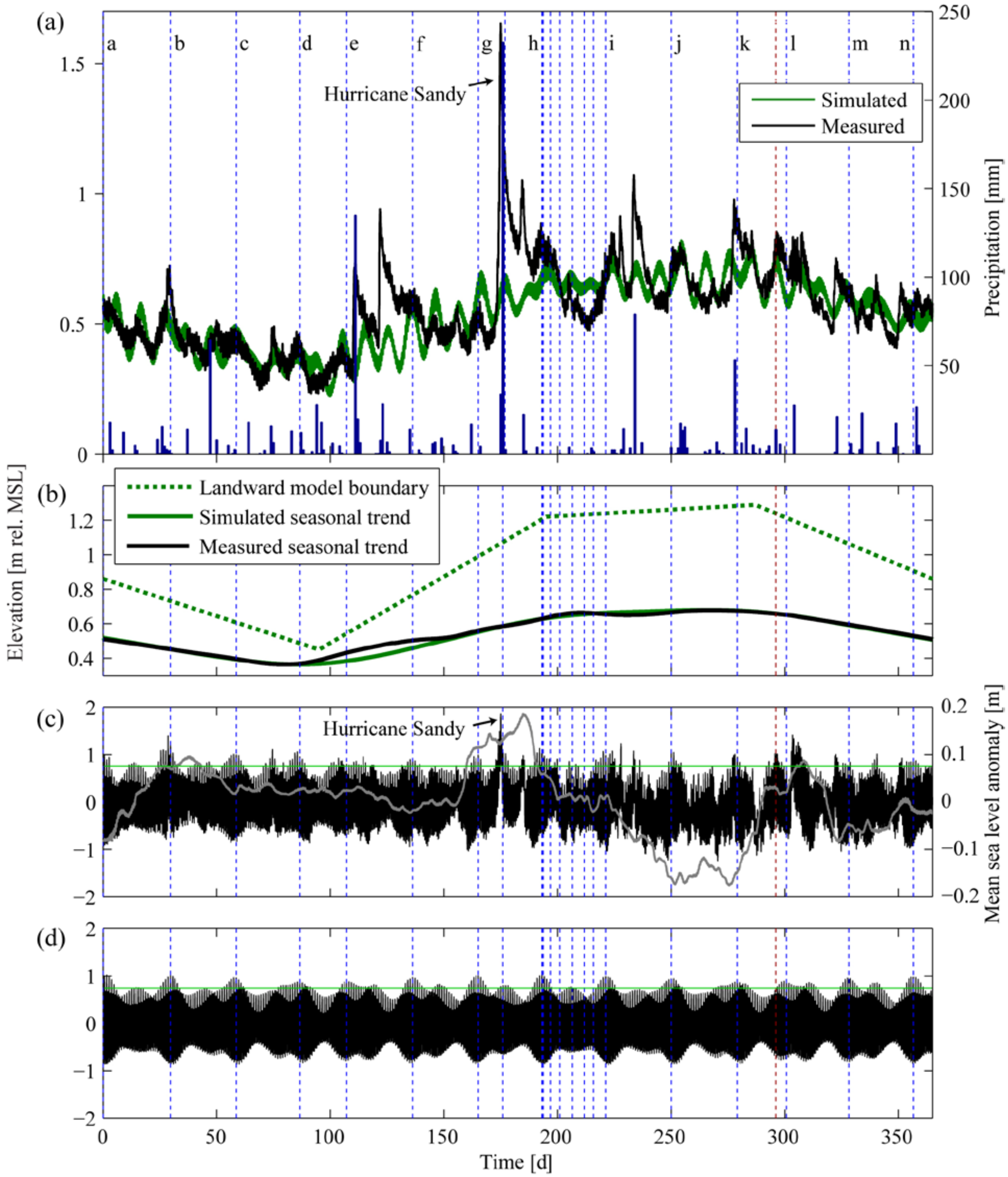

(a)
a
b
c
d
e
f
g
h
i
j
k
l
m
n
Hurricane Sandy
Simulated
Measured
Precipitation [mm]
(b)
Landward model boundary
Simulated seasonal trend
Measured seasonal trend
Elevation [m rel. MSL]
(c)
Hurricane Sandy
Mean sea level anomaly [m]
(d)
Time [d]

Figure 2.5. a) Daily precipitation and measured and simulated hydraulic heads at the dune well; HS = Hurricane Sandy sampling event; b) smoothed measured and simulated heads at dune well with the landward model head boundary; c) measured tide (black) and seasonal mean sea level anomaly (gray); d) tidal signal used in the model. Vertical blue lines denote sampling events. Vertical red line indicates timing of the tracer test. The horizontal green line on the tidal plots indicate the berm elevation. Time is days since 7 May 2012.

2.3.1.2 Tracer Experiment

The residence time and velocity of circulating saltwater were calculated by tracking the movement of the center of the tracer plume along its flowpath with time. The center of the plume and discharge location were interpreted from the bromide concentration contours mapped over the sampling ports. The maximum error in the position of the center of the plume is the distance between sampling ports: up to 80 cm vertically and 4 m horizontally, though the actual error is likely less. The results (Appendix I Figure 2.1) showed that seawater that entered the beach aquifer at the high tide mark flowed predominantly seaward before discharging across the lower beachface. The average velocity of the plume was 1.6 m/d, and the center of the plume began to exit the aquifer 7 days after injection. This velocity is close to the 1 m/d flow rate measured in a sandy beach by Michael et al. [2005] and less than the 10 m/d velocity measured by Boufadel and Bobo [2011]. The residence time is within the range of residence times (3 – 14 days) observed in other intertidal field settings [e.g. Michael et al., 2005; Abarca et al., 2013], but slightly shorter than a 9 day residence time simulated by Robinson et al. [2007b], and significantly shorter than the 66 day residence time simulated by Lenkopane et al. [2009].

2.3.1.3 Spatial and Temporal Variation of Measured Salinity

The salinity measurements revealed a cell of brackish to saline pore water overlying fresh groundwater beneath the beach surface at all sampling periods. The cell extended from the high tide mark to the lower end of the beach with salinity decreasing with depth. High salinity (>25 ppt) was found to depths of up to 3 meters beneath the mid-intertidal zone. A fresh groundwater discharge zone separated the circulation cell from the lower interface located at the base of the beach.

Over a semidiurnal tidal cycle, the salinity distribution remained nearly constant (left panels; Figure 2.6). The circulation cell remained centered beneath the mid-intertidal zone extending to a maximum depth of 2.5 m. This is consistent with results of numerical modeling studies [e.g. Ataie-Ashtiani et al., 1999; Mao et al., 2006; Robinson et al., 2007a; 2007b; 2007c].

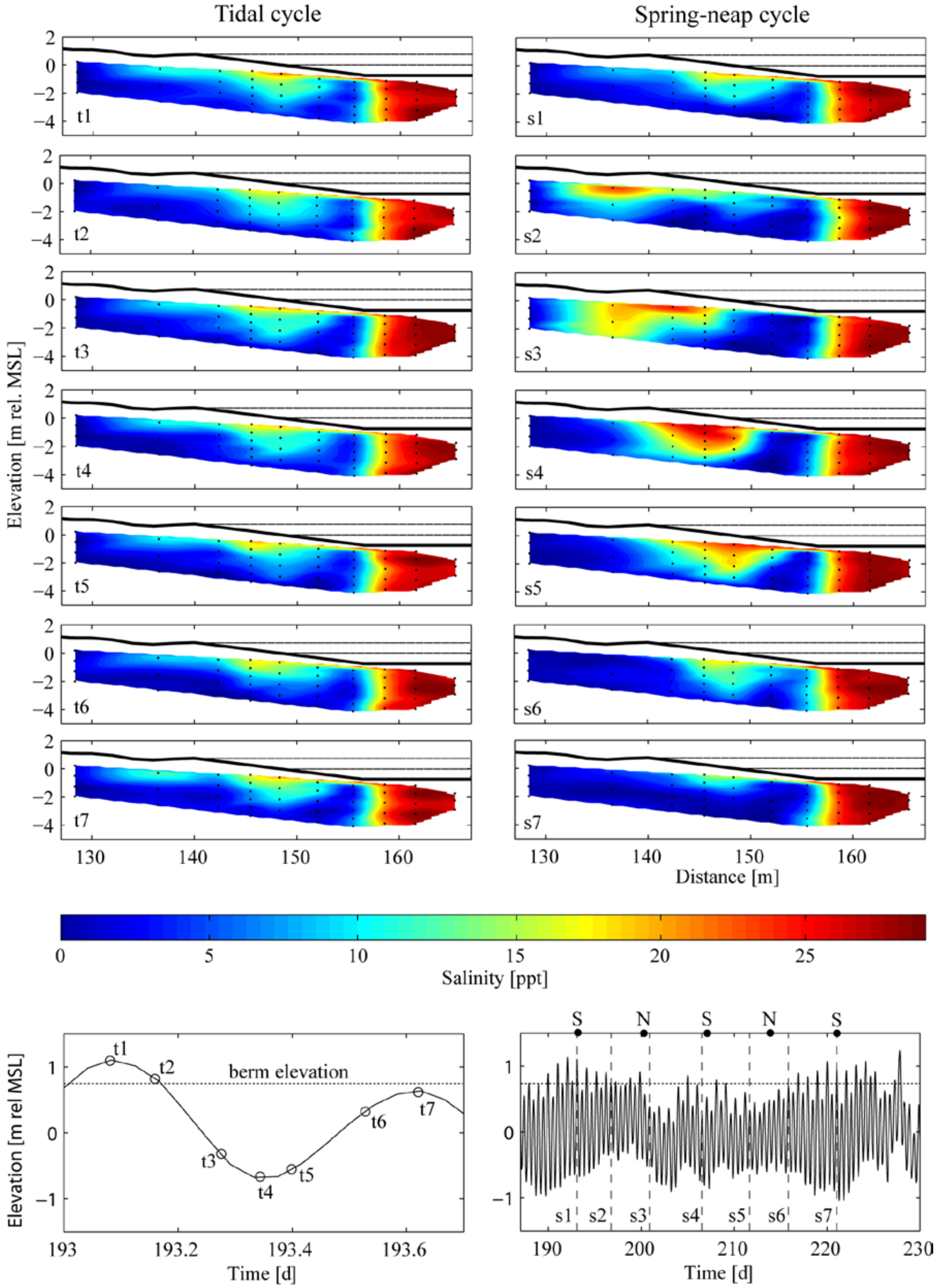
Tidal cycle
Spring-neap cycle
Elevation [m rel. MSL]
t1
t2
t3
t4
t5
t6
t7
s1
s2
s3
s4
s5
s6
s7
Distance [m]
Salinity [ppt]
berm elevation
Elevation [m rel MSL]
Time [d]
S
N
S
N
S

Figure 2.6. Measured pore water salinity over a tidal and spring-neap cycle. The horizontal line that intersects the beachface near the berm in each cross-section is MHHW and the horizontal line that intersects the mid-beachface is MSL. X-axis is distance relative to landward model boundary. Labels on salinity profiles correspond to sample times in the bottom two panels. The horizontal line on the tidal plots indicate the elevation of the sand surface at the berm. “S” and “N” on the spring-neap tidal plot denote spring and neap tide, respectively.

Over the monthly spring-neap cycle, the location of the circulation cell shifted and its size changed somewhat in response to changes in tidal amplitude (right panels; Figure 2.6). The cell moved downward from the backshore depression 4 days after the first spring tide, and then seaward before migrating upward near the beachface-MSL intersection following the second spring tide (206 d). Salinity below the backshore and upper beachface was elevated from days 193-200 (Figure 2.6 s2-s3), corresponding to the period when high tide exceeded the elevation of the berm. This led to infiltration across the backshore and a landward shift in the location of the circulation cell. Over this time interval, shallow salinity beneath the depression decreased while deeper (>1.5 m) salinity increased. As neap tide approached and the high tide elevation declined below the berm crest, fresh groundwater flowed laterally into the upper beach and salinity beneath the depression declined rapidly from 20 to 5 ppt (Figure 2.6 s3-s4). This freshening continued through the remaining spring-neap cycle (Figure 2.6 s5-s7). Beneath the mid to lower end of the beach, salinity increased as the cell shifted seaward during the period of lower tidal amplitude (Figure 2.6 s3-s5). The similarity of the salt distribution during the larger monthly spring tide measurement times (panels s1 and s7 in Figure 2.6) indicates that the observed oscillating pattern repeats over monthly spring-neap cycles. The observed shift in the position of the circulation cell was different from observations at other sites where the center of the cell remained stationary below the middle of the intertidal zone over a spring-neap cycle [e.g. Robinson et al., 2007a; Abarca et al., 2013].

Over the seasonal cycle, the circulation cell remained in approximately the same place, but its size changed significantly in response to the inland hydraulic gradient driving fresh groundwater flow (Figure 2.7). Since monthly sampling took place during spring tide, the high tide level at the times shown in Figure 2.7 exceeded the berm elevation. The salinity distributions in each panel thus indicate a response to berm overtopping. During a decline in the dune water table from 0 d – 80 d, intertidal salinities increased (Figure 2.5b and Figure 2.7a-e). Once the water table reached its lowest elevation (80 d; Figure 2.5b), the circulation cell occupied nearly the entire sampling zone (Figure 2.7d-e). As the dune water table started to rise, salinity in all parts of the aquifer below the beachface decreased until the water table reached its highest yearly elevation (268 d; Figure 2.5b). At this point the beach groundwater was mostly fresh (Figure 2.7i-j). Salinity again increased when the dune water table declined for the second time (268 – 365 d; Figure 2.5b and Figure 2.7k-n). Essentially, the effectiveness of tidal forcing increased as freshwater forcing decreased. Similar results have been demonstrated in numerical modeling studies [e.g. Robinson et al. 2007b; Kuan et al., 2012]. Here, we extend the findings of these previous studies to include the dynamic behavior of the cell under a non-steady landward head boundary.

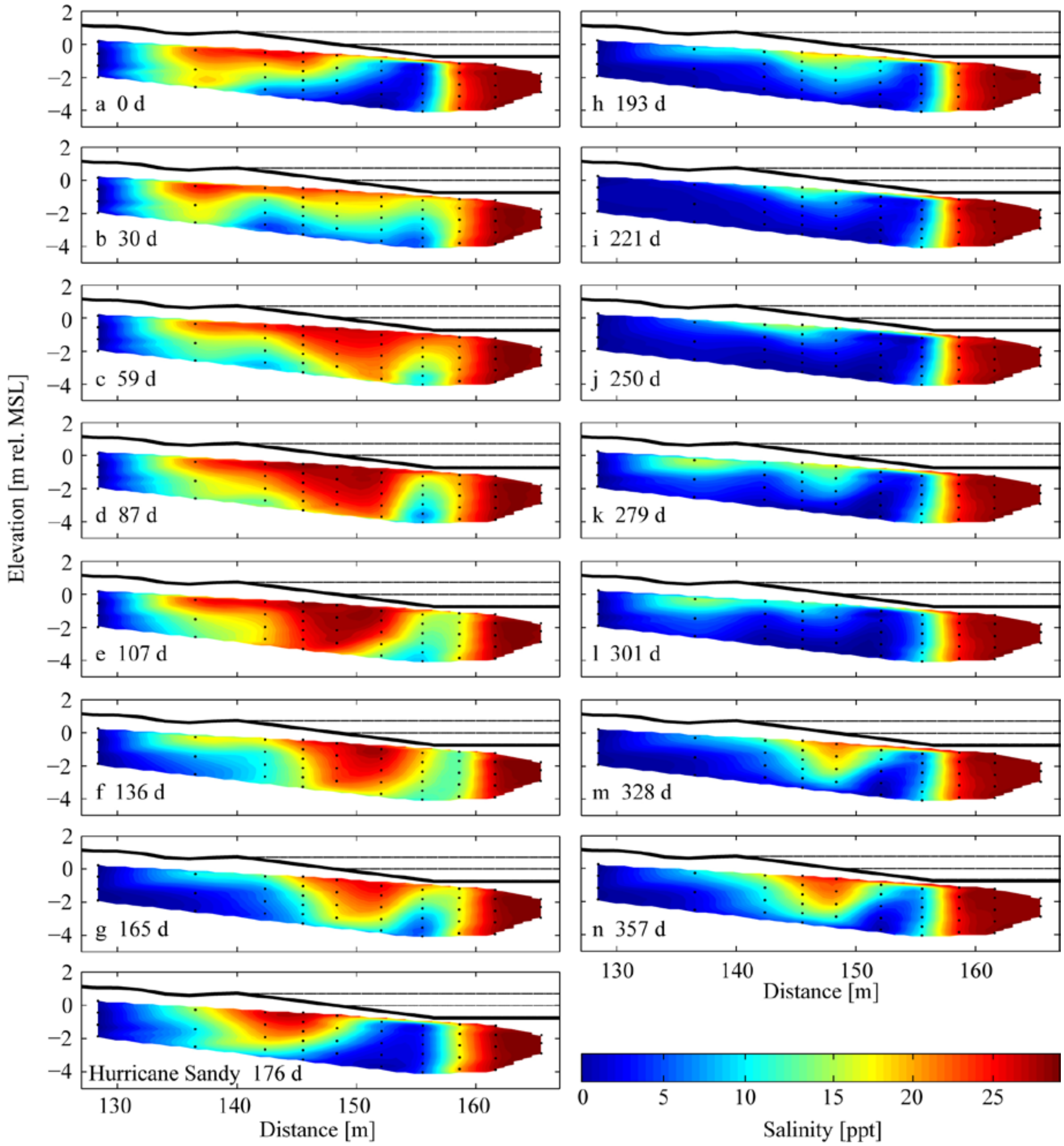

Figure 2.7. Measured monthly pore water salinity over a one-year sample period. The horizontal line that intersects the beachface near the berm in each cross-section is MHHW and the horizontal line that intersects the mid-beachface is MSL. X-axis is distance relative to landward model boundary. Labels on cross sections correspond to sample times in Figure 5a. The location of the sampling zone is shown in Figure 4.

Seasonal cycling of mean sea level can be an important mechanism controlling coastal aquifer salinization [e.g. Vera et al., 2012; Gonneea et al., 2013; Wood and Harrington, 2014]. These field studies showed that seasonally elevated mean sea levels can enhance seawater intrusion. At our site, however, seasonal variation of mean sea level did not appear to have a major influence on intertidal salinity. An approximately 15 cm positive sea level anomaly occurred between 155 and 200 days, prior to and during Hurricane Sandy (Figure 2.5c). During the sampling at 165 days (Figure 2.7g), mean sea level was elevated and the head at the dune had not yet risen due to heavy rains. However, the salinity distribution was freshened relative to the sampling at 136 days (Figure 2.7f), likely a response to the longer-term increase in mean head at the dune (Figure 2.5b). The negative mean sea level anomaly from ~225-285 days corresponded to the time of highest average dune water table. The effect was an increase in the hydraulic gradient driving fresh discharge, which may have contributed to more freshening than would have occurred without the sea level anomaly. However, the simulated and measured salinities matched well (see Section 4.2.1), despite the neglect of sea level anomalies in the model.

Episodic variations in rainfall, sea level, and wave action may also significantly affect the salinity distribution within the beach [e.g. Li et al., 2009; Gonneea et al., 2013; Robinson et al., 2014]. However, our salinity measurements after Hurricane Sandy indicate that the effects of the storm were short-lived and did not substantially impact the seasonal salinity pattern (Figure 2.7g). The storm made landfall 85 km northeast of Cape Henlopen as a post-tropical cyclone and generated a 1.23 m storm surge at the Lewes, DE tide gauge. Just prior to the sampling at 176 days, the dune head rose more than 1 m due to heavy rains (Figure 2.5a), creating a strong hydraulic gradient driving fresh discharge despite the anomalous rise in mean sea level. This resulted in freshening, a landward shift in the intertidal circulation cell, and a larger zone of fresh discharge (Figure 2.7). However, by the next sampling event at 193 days, salinities were much lower and in line with the overall seasonal trend of decreasing salinity during that part of the year. This suggests that the beach aquifer adjusts quickly after events such as moderate storm surges and enhanced fresh groundwater inflow as a result of elevated inland hydraulic heads from rainfall.

2.3.2 Model Simulations

Groundwater flow and salt transport in the coastal aquifer were simulated numerically to support interpretation of field results and to further analyze dynamics in response to simultaneous forcing on multiple timescales.

2.3.2.1 Comparison to Field Measurements

Simulated heads, salt concentrations, and groundwater velocities and residence times are first compared to the field results to ensure consistency. The seasonal trend in simulated head at the location of the dune well matched reasonably well to measurements (Figure 2.5b). On an hourly timescale, deviations of up to 1.08 m occurred between measured and simulated heads (Figure 2.5a). This was due, at least in part, to the limitations of the numerical model, which did not account for waves, storms, or precipitation events that have been shown to affect hydraulic heads and salinity distributions in other coastal aquifers [Anderson, 2002; Smith et al., 2008; Xin et al., 2010; Wilson et al., 2011; Robinson et al., 2014]. Despite this, measured and simulated salinities at the time of the Hurricane Sandy sampling event agreed well (Figure 2.8). The head deviations may also have been the result of the difference between the measured tidal fluctuations (Figure 2.5c) and the simulated periodic boundary condition (Figure 2.5d). However, the measured and simulated amplitude of the head oscillations at the dune well in response to tidal forcing and spring neap variability in tidal amplitude compared favorably. The simulated head at the dune fluctuated over the same 5-10 cm range that was measured in the field. Spring-neap fluctuations were also within the 10-25 cm range of those measured at the dune. The reasonable match despite short timescale deviations indicates that the system responds to hydrologic fluctuations over longer timescales.

The model also reproduced field measurements of salinity over the spring-neap and seasonal time periods (Figure 2.8). Salinity variations over the semidiurnal tidal cycle also agreed favorably but are not shown in Figure 2.8, as there were no significant changes. In addition to matching well the salinity in the circulation cell, the model replicated variations in the positions of the fresh discharge zone and lower interface. The change in the location of the lower interface over the spring-neap cycle is evidenced by the changes in measured and simulated salinity at the shallowest port at well 8 (Figure 2.8). Over the seasonal time period, measured and simulated salinity at the bottom port at well 6 declined abruptly at 150 days, indicating a shift of the fresh discharge zone landward (Figure 2.8).

The simulated bromide tracer plume closely matched the overall migration of the experimental tracer through the subsurface (Appendix Figure 2.1). The simulated plume traveled predominantly seaward at an average rate of 1.4 m/d before discharging across the lower beachface 8 days after injection.

Given that the simulated heads, groundwater velocities, and salinities were satisfactorily matched to the field data, the model was used to examine: 1) the horizontal surface extent of the circulation cell; 2) the cross-sectional area of the intertidal mixing zone; and 3) fresh and total SGD across the aquifer-ocean interface over each of the three time periods

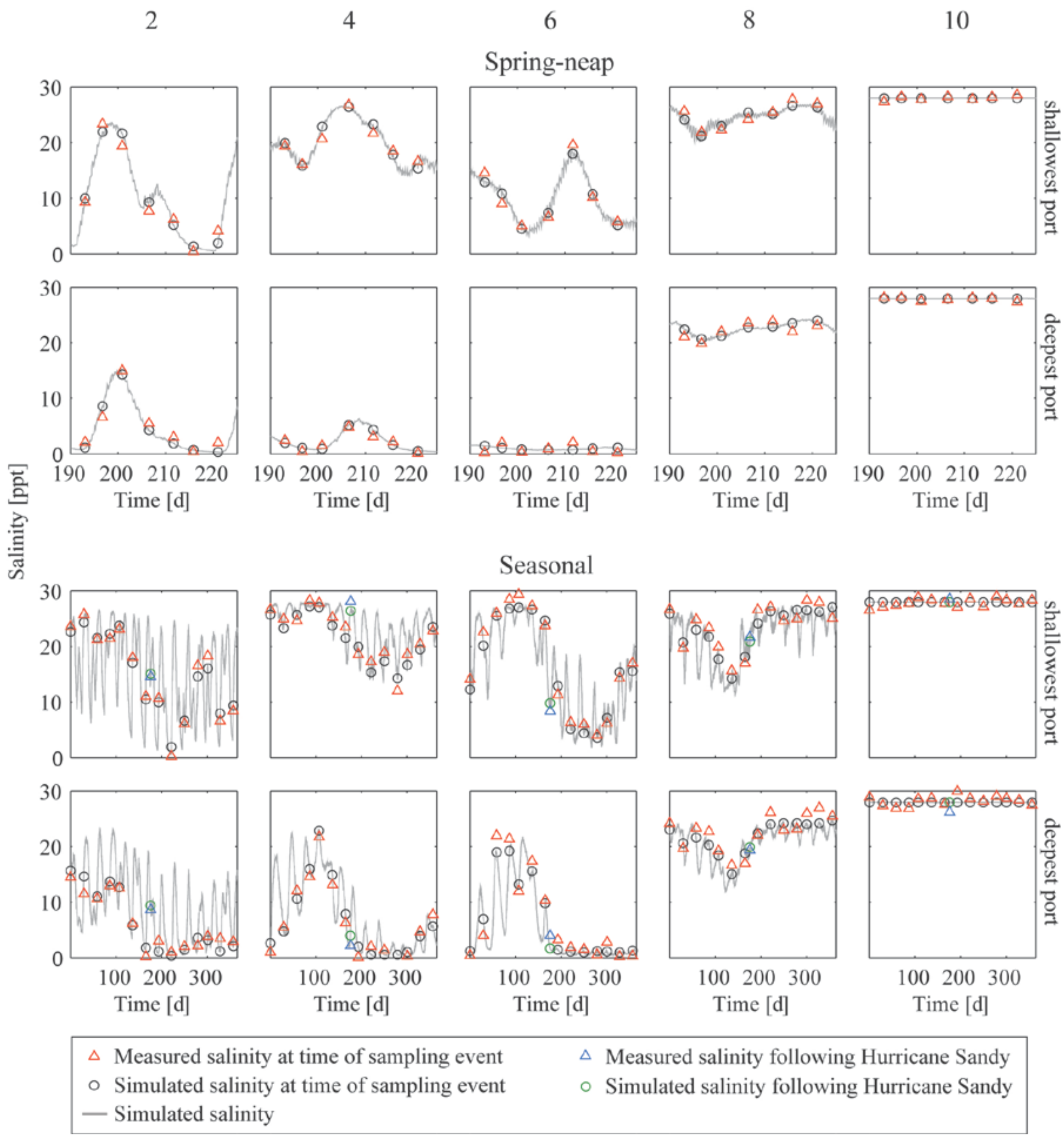

Figure 2.8. Observed and simulated pore water salinity for the shallowest and deepest ports for selected multilevel samplers (numbered at top) over a spring-neap and seasonal time period.

2.3.2.2 Tidal, Spring-Neap, and Seasonal Cycling of Shallow Salinity

Figure 2.9 shows salinity across the top layer of model domain over time. These near-surface salinity dynamics provide insight into the importance of each of the three time scales in controlling the horizontal surface extent of the circulation cell, fresh discharge zone, and top of the lower freshwater-saltwater interface.

The horizontal extent of the circulation cell remained largely unchanged through the semidiurnal tidal period (Figure 2.9a). The tidal cycle and salinity response shown Figure 2.9a correspond to the same tidal cycle that was investigated in the field. Salinity across the sand surface was highest near the mid-section of the intertidal zone, consistent with previous numerical modeling studies that indicate high infiltration rates from the mid tide mark to the upper beach [e.g. Abarca et al., 2013]. A region of low salinity at the berm (x = 140 m) separated the high salinity between the high and low water marks from a smaller region of high salinity in the backshore (x = 134-138 m) (Figure 2.9a). The two sets of saltwater plumes, one beneath the beachface and a second below the backshore, was both simulated and observed (see panels a and g in Figure 2.6). This highlights the influence of beach morphology on the structure of the circulation cell and is consistent with findings in other modeling studies [i.e. Robinson et al., 2006; Abarca et al., 2013]. Salinities over other tidal cycles also were also unaffected by tidal stage.

Salinity across the top of the model and the horizontal extent of the circulation cell varied over monthly and biweekly spring-neap cycles. Figure 2.9b shows simulated concentrations over the same spring-neap cycle examined at Cape Shores. Salinity was generally highest across the upper beachface 4-5 days following the monthly spring tide. The salinity distribution reversed as the tidal amplitude declined; salinity beneath the upper beachface and backshore decreased while it increased across the mid-intertidal zone. The high salinity in the backshore was brought about by an increase in the landward extent of the shoreline at high tide during spring tide. This resulted in overtopping of the berm with seawater, which infiltrated in the backshore and circulated seaward to the base of the beach over the remainder of the spring-neap cycle. The circulation of seawater from the upper to lower beach indicated a seaward shift in the location of the circulation cell. In response to the shift, the fresh discharge zone contracted by approximately 4 m (201 – 212 d) and the lower interface oscillated 1-2 meters. Similar salinity patterns occurred over biweekly spring-neap cycles (Figure 2.9b). The salinity pattern and oscillation of the lower interface are consistent with field measurements (right panels; Figure 2.6), supporting the assertion that variations were due to spring-neap cycling combined with berm overtopping rather than shorter timescale events such as storms. Previous studies have also shown that the lower interface can oscillate in response to forcing by a sinusoidal tide [e.g. Robinson et al. 2007b; Xin et al., 2010] and over spring-neap cycles [e.g. Abarca et al., 2013]. Our results indicate that these oscillations are consistent throughout the year, despite changes in the inland hydraulic gradient.

The elevation of the inland water table affected the width of the circulation cell and the location and width of the freshwater discharge zone. The width of the cell was narrowest when the water table was high, ranging from 10 m to 23 m over spring neap cycles (180 – 300 d; Figure 2.9c). The cell was wider during times when the water table was low, ranging from 14 m – 26 m over spring-neap cycles (50 – 140 d; Figure 2.9c). The cell expanded primarily seaward, which displaced the freshwater discharge zone and lower interface seaward. As the inland water table rose and flushing of infiltrated saltwater intensified, the horizontal extent of the cell decreased, allowing the discharge zone and lower interface to encroach landward. The inland water table had an opposite effect on the width of the discharge zone. In this case the width of the discharge zone expanded by approximately 3 m and became fresher from 120 to 270 days as the inland water table increased. The decrease in salinity in the discharge zone can be explained by dilution from greater freshwater discharge as well as a decrease in intertidal circulation rates, which reduces dispersion along the lower interface and the amount of salt entrained in discharging groundwater [e.g., Robinson et al., 2007c]. Thus, seasonal inland water table oscillations had a greater effect on the location of the freshwater discharge zone than on its width in the presence of tidal oscillations. In contrast, spring-neap cycling of tidal amplitude primarily influenced the width of the discharge zone.

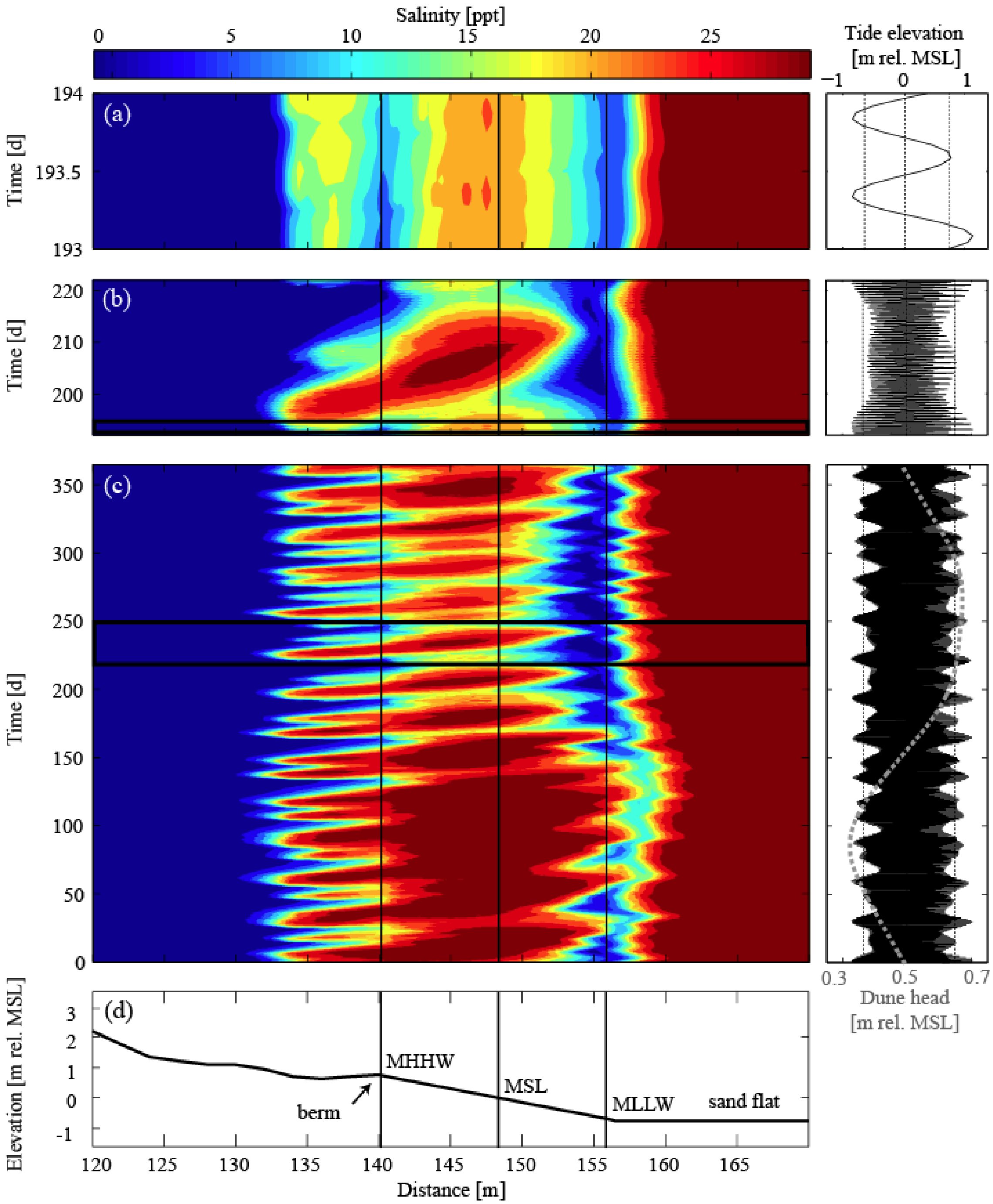

Salinity [ppt]
0
5
10
15
20
25
Tide elevation
[m rel. MSL]
−1
0
1
194
193.5
193
Time [d]
(a)
220
210
200
Time [d]
(b)
350
300
250
200
150
100
50
0
Time [d]
(c)
0.3
0.5
0.7
Dune head
[m rel. MSL]
(d)
3
2
1
0
-1
Elevation [m rel. MSL]
MHHW
MSL
MLLW
sand flat
berm
120
125
130
135
140
145
150
155
160
165
Distance [m]

Figure 2.9. Simulated salinity across the top of the model domain. Salinity is shown over a) a tidal cycle; b) a spring-neap cycle; and c) a seasonal cycle. d) Beach profile. The three black vertical lines in panels a-d correspond to the location of the intersection between beachface and MHHW, MSL, and MLLW. The horizontal black rectangle in panel (c) corresponds to the time period shown in panel (b). The horizontal black rectangle in panel in panel (b) corresponds to the time period shown in panel (a). The location of the berm coincides with the beachface-MHHW intersection. The dashed lines on the tide plots are MHHW, MSL, and MLLW. X-axis is distance relative to landward model boundary. Time is days since 7 May 2012.

2.3.2.3 Size of the Mixing Zone

Hydrodynamic dispersion and the transient response to forcing in the intertidal zone resulted in mixing of fresh and saline water along the perimeter of the intertidal circulation cell. This mixing zone is often biogeochemically active, so we considered its response to hydrologic fluctuations. For this purpose, we defined the size of the mixing zone as the cross-sectional area beneath the intertidal zone that fell within a range of salinity contours. Five ranges were considered; 5 – 95%, 10 -90%, 20 – 80%, and 30 – 70% saltwater.

The mixing area varied up to 3 m2 per tidal cycle (Figure 2.10a). The mixing area generally began to increase at high tide and reached a tidal cycle maximum 3-4 hours later near low tide. Semidiurnal differences in tidal amplitude did not appreciably influence the size of the mixing zone.

Mixing area varied more with tidal amplitude over lunar cycles than over semidiurnal tidal cycles, as indicated by the 10 m2 fluctuation in area that occurred over about 14 days. This is illustrated from day 193 to 207, the same time period that was investigated in the field (Figure 2.10b). The mixing area reached a lunar cycle maximum on day 197, 4 days after spring tide, and shrank to its smallest area on day

203.5, 5.5 days after neap tide. The 4-5.5 day time lag is likely due to infiltration across the backshore, which continued to salinize the aquifer and increase the size of the mixing zone while the high tide elevation was above the berm crest. A similar time lag time (3 days) in intertidal salinity was measured and simulated over a two-week spring cycle by Robinson et al., 2007a. The time lag and response of the mixing zone was consistent across the other spring-neap cycles.

The greatest change in the area of the mixing zone was in response to the seasonal inland water table oscillations, varying up to 115 m3 for the 5 – 95% seawater contours (Figure 2.10). Yearly cycling in the size of the mixing zone was also greatest for the other three salinity ranges. The largest mixing zone (119 d) formed when the inland water table was near its lowest elevation (86 d). This was due to a reduction in freshwater forcing as the water table dropped, allowing the tidal circulation to strengthen and the area of the mixing zone along the boundaries of the circulation cell to increase. The opposite was the case for the smallest area, which occurred 45 days preceding the highest water table. The greater landward hydraulic gradient pushed the circulation cell up toward the surface and maintained a smaller mixing area (Figure 2.11). The temporal offsets between the maximum and minimum areas and the highest and lowest inland water table elevations were caused by the effects and spring and neap tides, which were large enough to impact the timing of the largest and smallest mixing zone areas over the one-year timeframe.

The simulation results demonstrate the importance of seasonality on mixing zone dynamics and show that shorter-term tidal and spring-neap oscillations in the size of the mixing zone are superimposed on the longer-term and more dominant seasonal cycle. These findings were qualitatively supported by the field observations, but have not been quantified prior to this work. The time lag and behavior of the mixing zone in response to the various forcing conditions was similar to that of the full circulation cell; the mixing zone expanded and contracted in-phase with the cell.

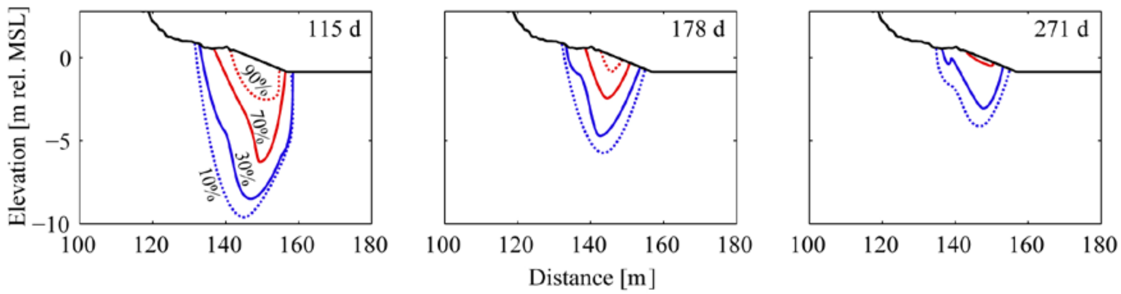

Figure 2.10. Simulated mixing zone area at selected times for 10 – 90% saltwater (between the two dotted isohalines) and 30 – 70% saltwater (between the two solid isohalines).

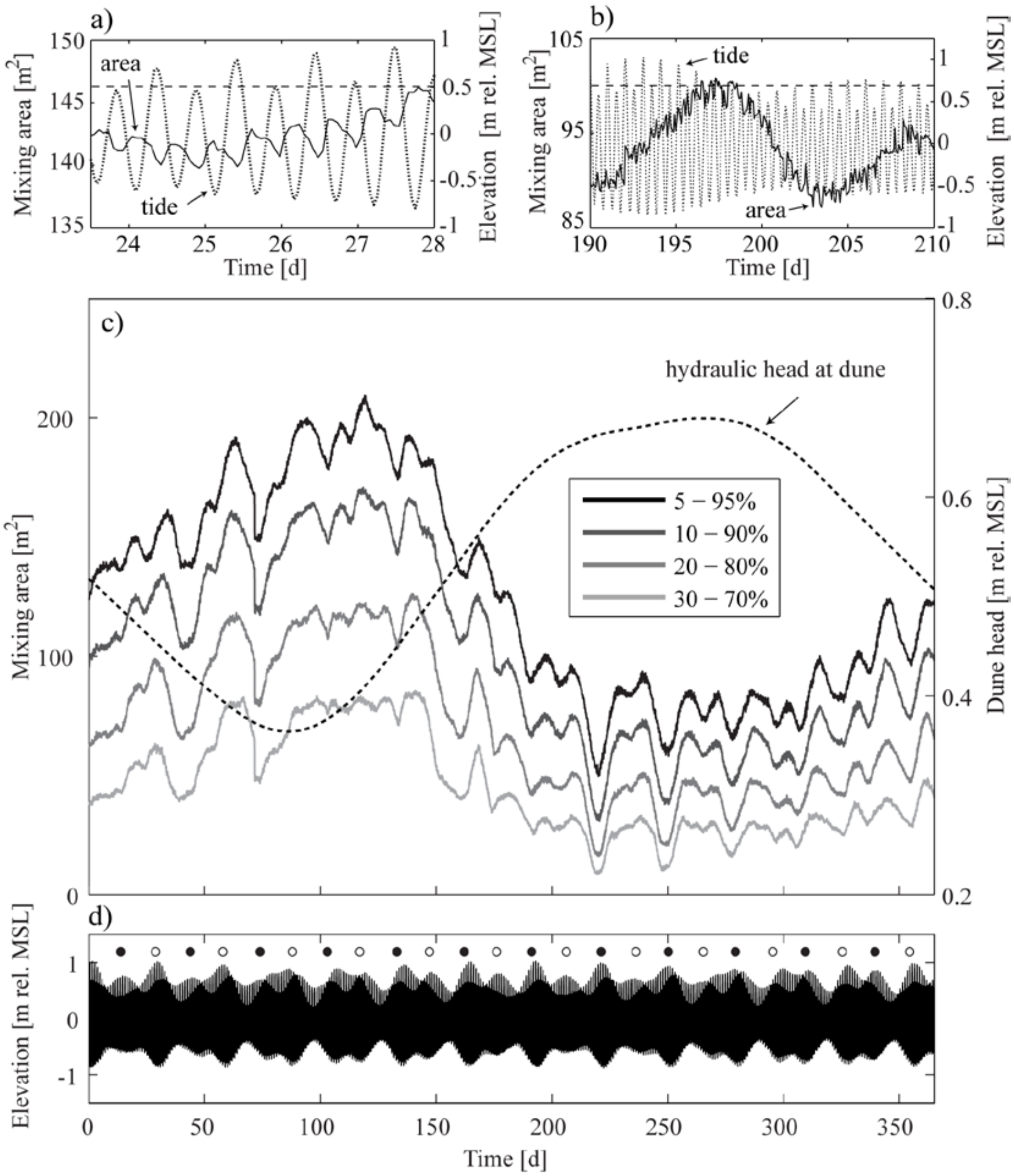

a)
b)
c)
d)
Mixing area [m^2]
Elevation [m rel. MSL]
Time [d]
area
tide
hydraulic head at dune
5 − 95%
10 − 90%
20 − 80%
30 − 70%
Dune head [m rel. MSL]

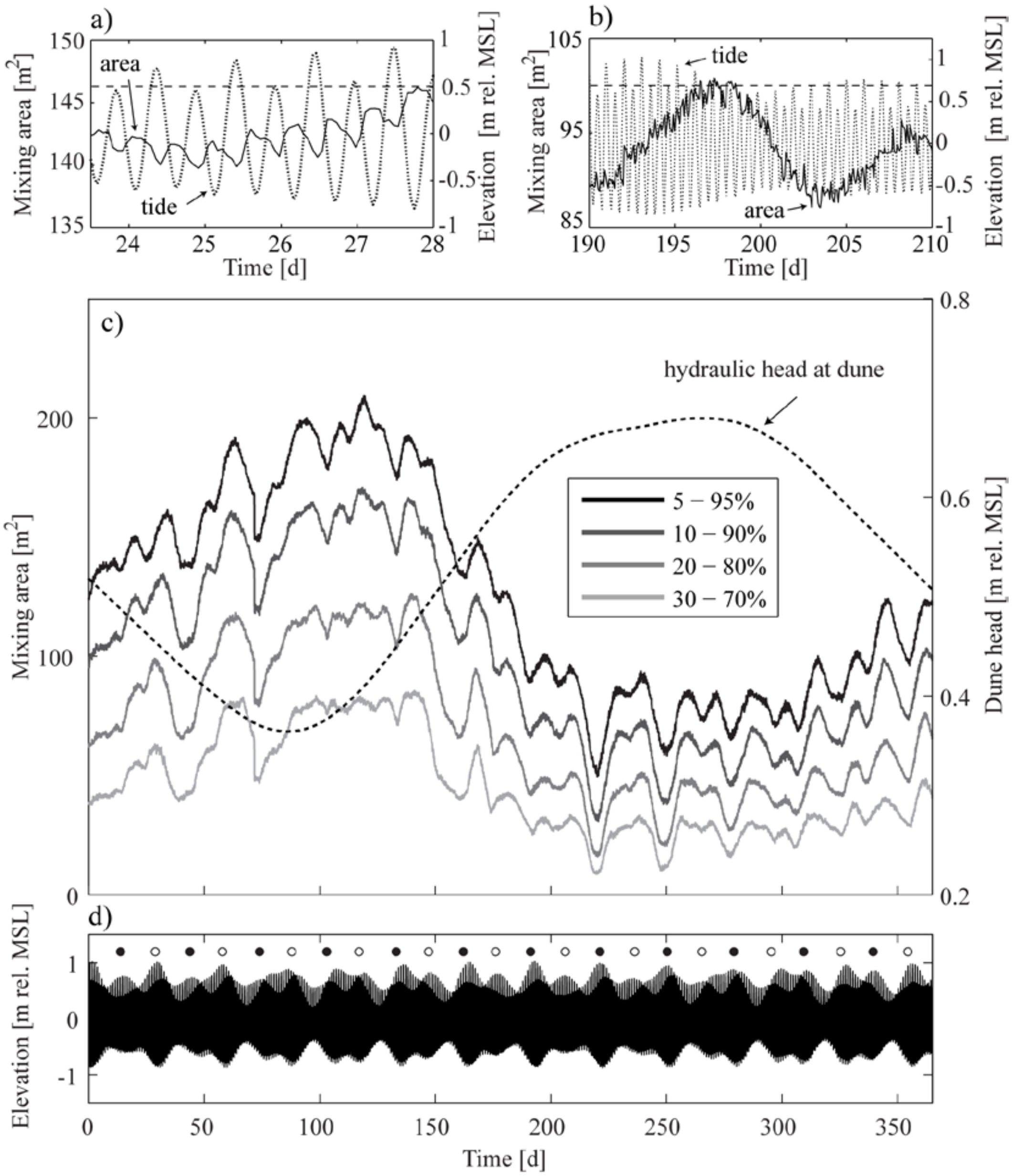

Figure 2.11. Simulated mixing zone area over a) individual tidal cycles and (b) over a spring-neap cycle using the 5 - 95% seawater salinity contours. c) Area of the mixing zone for different salinity ranges (as percentage of the maximum simulated salinity) over the one-year simulation period. d) Predicted tide used in the simulation. Symbols at the top of panel (d) denote full (white) and new (black) moons. The horizontal dotted lines on (a) and (b) indicate the elevation of the sand surface at the backshore depression.

2.3.2.4 Significance of Berm Overtopping

The measured and simulated results suggest that berm overtopping and infiltration across the backshore is an important factor that regulates the formation and dynamics of the circulation cell. The observations of higher salt concentrations beneath the depression in panel s3 in Figure 2.6 and Figure 2.9a suggest that overtopping substantially alters the spatial extent of the circulation cell. To demonstrate this importance, a simulation without a berm or backshore depression was performed with the same flow and transport boundary conditions. The slope of the beachface boundary was uniform and equal to the measured slope (1:9). In effect, the beachface was extended landward to the dune.

The beach profile affected the horizontal and vertical extent of the circulation cell considerably. Figure 2.12 shows the salinity distributions for simulations with and without the berm at selected times for each of the three timeframes. The results show that in the absence of berm overtopping, a secondary region of higher salt concentration beneath the upper beachface landward of 140 m (panels t1 and k; Figure 2.12) did not develop. The lack of infiltration across the upper beach profile resulted in a circulation cell that was smaller by up to 6 m horizontally and 3 m vertically compared to the simulation with the berm (Figure 2.12).

While the structure and extent of the circulation cell was modified by the beach profile, the general dynamics of the cell over the three timescales were preserved. In particular, phase-averaged velocity vectors over a tidal cycle indicate that the single cell of circulating seawater in the non-berm scenario was maintained when the berm was removed (Figure 2.12). The vectors also show that under some conditions (rows d and k; Figure 2.12), the backshore and intertidal salinity zones in the berm scenario connect, while under other conditions (row t1; Figure 2.12) these salinity zones are separate and the backshore saltwater flows downward and mixes with underlying fresh water. Salinity remained largely unchanged over tidal cycles while the circulation cell expanded and contracted over monthly spring-neap cycles (rows s3-s5; Figure 2.12) and seasonally (rows d and k; Figure 2.12). Thus, similar transient behavior of the circulation cell may be expected in beaches with differing morphologies, while its structure may vary widely.

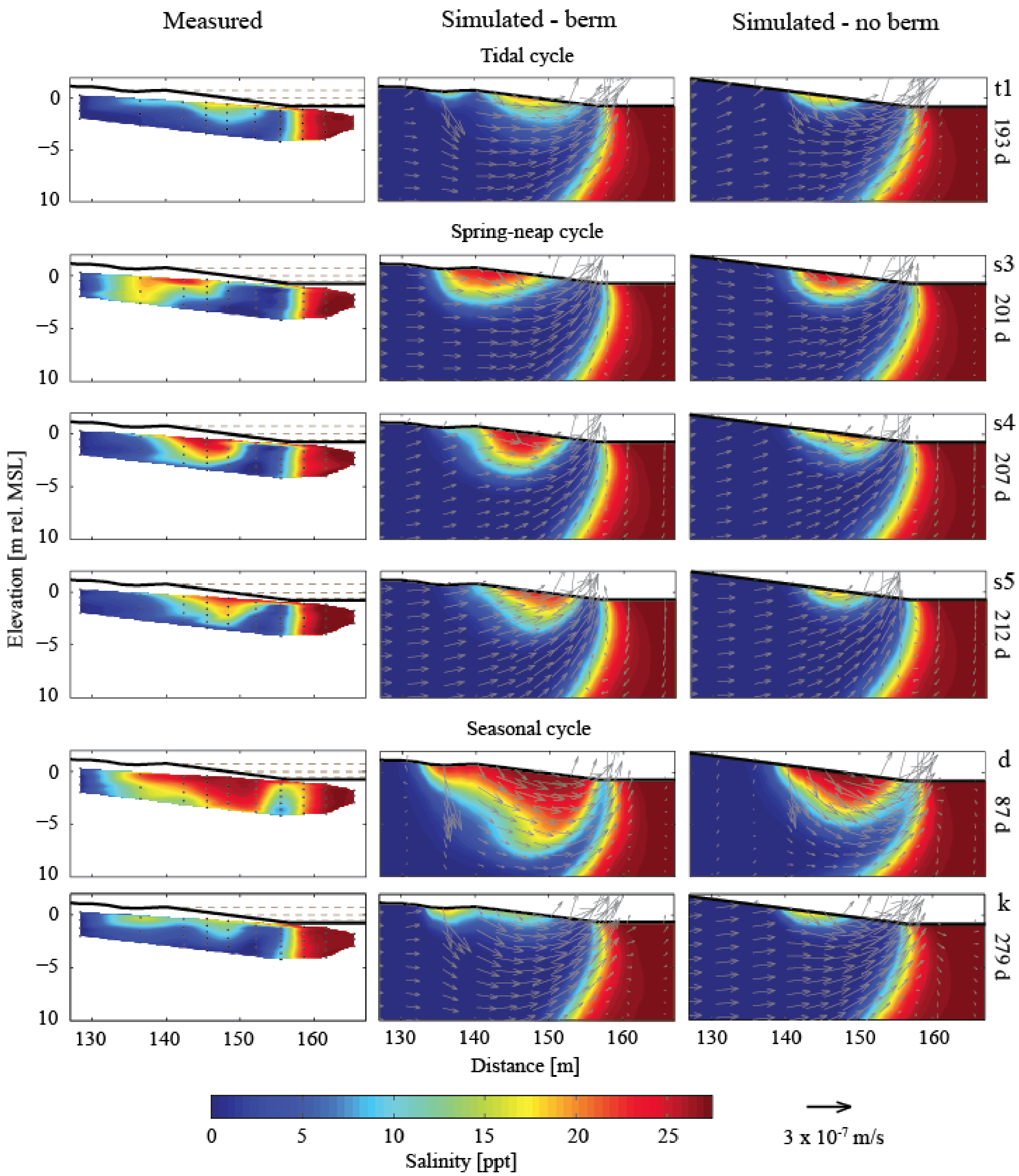

Figure 2.12. Measured and simulated salinity with and without a beach berm. The row labels for the tidal (t1) and spring-neap (s3-s5) cross-sections correspond to those in Figure 6. The seasonal (d and k) cross-sections correspond to those in Figure 5. The top, middle, and bottom horizontal dashed lines intersecting the beachface are MHHW, MSL, and MLLW, respectively. The location of the sampling zone in column 1 and location of the cross-sectional areas in columns 2 and 3 are shown in Figure 4.

2.3.2.5 Fresh and Saline SGD

Both fresh and saline SGD responded to tidal stage. The top and bottom of each of the two shaded regions on a particular day in Figure 2.13 (top panel) indicate the maximum and minimum value of saline or fresh SGD that occurred over the tidal cycle on that day, respectively. For example, for the tidal cycle that occurred on day 250, fresh SGD reached a maximum of 3.0 x 10-5 m3/s per meter length of shoreline and a minimum of nearly zero. This large range is expected as the lower freshwater hydraulic gradient during high tide significantly reduced fresh SGD, while beach drainage and a stronger gradient during low tide promoted fresh SGD. Similarly, saline SGD decreased during high tide as the hydraulic gradient driving upward flow in the saltwater circulation cell was reduced.

Changes in tidal amplitude also impacted fresh and saline SGD (Figure 2.13). The ~14 and 30 day fluctuations in fresh and saline SGD correspond to spring-neap cycles. Previous field [e.g. Robinson et al., 2007a] and numerical modeling [e.g. Abarca et al., 2013] studies have identified similar SGD behavior.

Seasonal fluctuations affected both the average magnitude and the daily fluctuations of fresh and saline SGD. Fresh SGD varied with inland hydraulic head while saline SGD varied inversely. The percentage of total SGD that was fresh therefore varied significantly, ranging from 48% to 85% over the one-year simulation period (bottom panel; Figure 2.13). Fresh SGD increased with the inland head due to the increased freshwater hydraulic gradient. The greater inflow of fresh groundwater reduced the size of the saline circulation cell, thus reducing saline circulation and discharge, consistent with simulations [e.g. Robinson et al. 2007c]. The lowest percent fresh SGD (126 d) lagged 35 days behind the lowest inland water table level. This offset was caused by the spring-neap cycling in tidal amplitude, which had a similar impact on the timing of the lowest percent of fresh SGD as it did on the timing of the minimum mixing zone area discussed in Section 4.2.4. Simulated saline SGD included the tidally driven intertidal processes investigated here, as well as offshore exchange induced by tidal pumping [e.g. Riedl et al., 1972; Shum and Sundby, 1996] and density gradients [Cooper, 1969]. However, it did not include exchange driven by processes such as waves [Precht and Huettel, 2003; King et al., 2009], currents [Huettel et al., 1996], and bioirrigation [Cable et al., 2006], which can induce significant seawater exchange [e.g. Santos et al., 2012; Sawyer et al., 2013]. Aquifer heterogeneity may also impact spatial and temporal SGD patterns [e.g. Michael et al., 2003; Russoniello et al., 2013; Sawyer et al., 2014]. Because tidal pumping is generally small relative to intertidal circulation [Li et al., 1999] and density-driven convection is relatively constant where the lower interface exists [Abarca et al., 2007], the simulated variability was likely primarily due to changes in intertidal circulation.

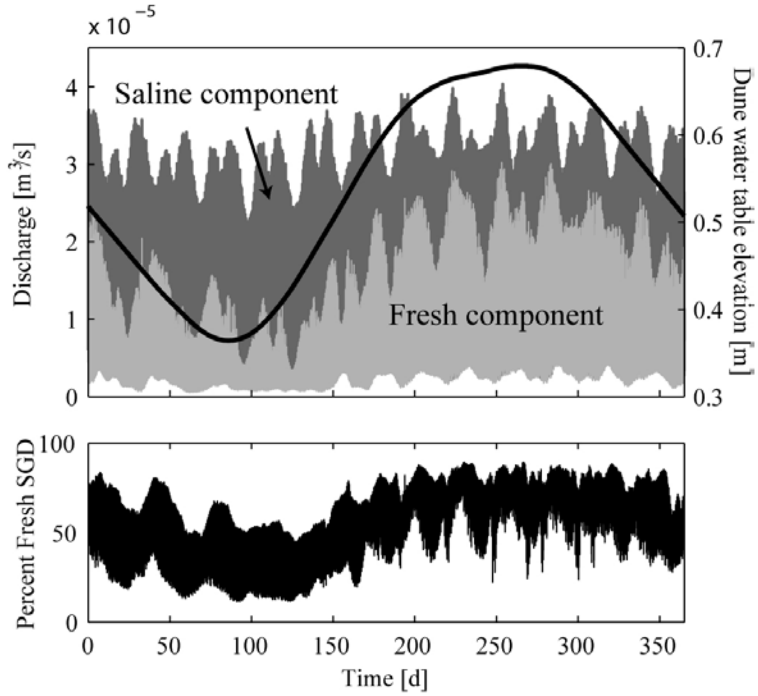

Figure 2.13. Stacked plot of the simulated fresh and saline components of SGD with dune head (top panel) and percent of SGD that is freshwater (bottom panel). Discharge is per m length of shoreline.

2.4 Implications for Reactivity and Chemical Fluxes

Biogeochemical reactions that occur in beach aquifers can alter fluxes of nutrients, heavy metals, and other reactive contaminants to the coastal zone [Moore, 1999; Charette and Sholkovitz, 2002; Santos et al., 2008; Spiteri et al., 2008; Santoro et al., 2010]. The biogeochemical reactivity of these systems is ultimately linked to the physical processes of groundwater flow, mixing, and solute transport that form redox and salinity gradients and a biogeochemically active environment. The highly transient nature of these physical processes over the three time scales identified in this study is likely to impact the fate and distribution of reactive chemicals in the nearshore aquifer. For example, abiotic and biologically mediated chemical transformations occurring within the beach saltwater-freshwater mixing zone [e.g. Charette et al,. 2005; Beck et al., 2007; Roy et al., 2013] may become enhanced as the mixing zone expands during extended periods of reduced recharge and a low inland water table. In addition, variability in the biogeochemical environment may provide, within the beach aquifer, the conditions for multiple pathways of contaminant degradation, immobilization, or release. Moreover, the rate of movement of the zone of interrmediate salinities along the lower saltwate-freshwater interface in response to the various forcing mechansims may also affect the types of microbial communities in the beach aquifer. Thus, accurate predictions of the types and rates of subsurface chemical transformations and of chemical fluxes related to SGD requires a comprehensive understanding of the hydrodynamics of the beach-aquifer system over a range of time scales. The results of this work may provide insight into the processes that affect biogeochemically reactive zones in beach aquifers and the timescales over which they may change.

Groundwater flow and transport processes in beach aquifers differ significantly from those occurring offshore. Residence times and flowpaths tend to be shorter [e.g. Michael et al., 2005; Robinson et al., 2007a; Michael et al., 2011; Abarca et al., 2013] and oxygen levels higher [Kroeger and Charette, 2008; Charbonnier, et al., 2013] in the circulating seawater in the beach relative to those in circulating seawater offshore [Kroeger and Charette, 2008; Abarca et al., 2013]. Because the hydrodynamics, residence times, and chemical composition of water sources differ, the mixing zone in beach aquifers is likely to exhibit different geochemical and microbial zonations than those along the lower interface and offshore. These contrasting flow and transport regimes may have important implications for the types and rates of chemical transformations that contaminants may undergo prior to discharging to nearshore marine ecosystems.

2.5 Conclusions

Measurements of intertidal pore water salinity collected over three timescales were combined with a variable-density numerical model to explore the importance of tidal stage, tidal amplitude, and seasonal inland water table fluctuations on the hydrodynamics and salinity distribution in a sandy beach aquifer. Measured and simulated salinities in the beach aquifer revealed an upper brackish to saline circulation cell and mixing zone with a structure, cross-sectional area, and horizontal and vertical extent that varied over tidal, spring-neap and seasonal timescales. Simulated SGD also responded to these hydrologic fluctuations.

The three timescales of forcing had different effects on the intertidal circulation cell. Observations and simulations showed that the horizontal and vertical extent of the cell was primarily controlled by seasonal changes in the inland water table, and by extension the freshwater flux. Although the circulation cell remained in approximately the same place during spring tide over a seasonal cycle, its size changed significantly. Both the circulation cell and the size of the mixing zone along its perimeter were largest during periods of low inland water table and smallest when the water table was highest. As the water table decreased, the fresh discharge zone and lower interface moved seaward due to a widening of the circulation cell that displaced the discharge zone. A high inland water table also resulted in slightly greater total SGD and a significantly higher percent of fresh SGD due to the stronger inland gradient driving fresh groundwater flow.

Changes in tidal amplitude over spring-neap cycles also influenced the intertidal dynamics, but to a lesser degree than seasonal water table fluctuations. Salinity beneath the backshore increased near spring tide as the backshore depression became inundated due to larger tidal amplitudes. The center of the circulation cell shifted seaward over the spring-neap cycle from beneath the backshore depression to the mid-section of the intertidal zone. In response to this shift, the fresh discharge zone contracted and the lower interface oscillated over the fortnightly and monthly spring-neap cycles. The size of the mixing zone varied over spring-neap and tidal cycles, though to a lesser degree than over the one-year timeframe. Tidal cycle fluctuations in sea level had the smallest effect on the salinity distribution and mixing zone. However, both tidal elevation and tidal amplitude significantly affected both the amount of fresh and saline SGD and their ratio.

Comparison between simulations with and without a berm and backshore depression demonstrated that berm overtopping modified the structure of the landward portion of the circulation cell. Nevertheless, the dynamic behavior of the circulation cell, fresh discharge zone, and lower interface was largely preserved over the three time scales for both the berm and non-berm scenarios.

The results provide insight into the time scales and physical forcing mechanisms that are important to the nature of the intertidal saltwater circulation cell, the locations of fresh and saline groundwater discharge, and the position of the nearshore portion of the lower saltwater-freshwater interface. The field measurements and model results demonstrate the highly transient nature of beach groundwater, emphasize the need to consider dynamic behavior in studies of intertidal flow, transport, and chemical reactivity, and indicate that measurements taken at a single point in time should be cautiously extrapolated.

REFERENCES

Abarca, E., J. Carrera, X. Sánchez-Vila, and M. Dentz (2007), Anisotropic dispersive Henry problem, *Adv. Water Resour.*, *30*(4), 913–926, doi:10.1016/j.advwatres.2006.08.005.

Abarca, E., H. Karam, H. F. Hemond, and C. F. Harvey (2013), Transient groundwater dynamics in a coastal aquifer: The effects of tides, the lunar cycle, and the beach profile, *Water Resour. Res.*, *49*, 1–16, doi:10.1002/wrcr.20075.

Anderson., W.P. Jr. (2002), Aquifer Salinization from Storm Overwash, *J. Coast. Res.*, *18*(3), 413–420.

Ataie-Ashtiani, B., R. E. Volker, and D. A. Lockington (1999), Tidal effects on sea water intrusion in unconfined aquifers, *J. Hydrol*., 216, 17–31

Bakhtyar, R., D. A. Barry, and A. Brovelli (2012), Numerical experiments on interactions between wave motion and variable-density coastal aquifers, *Coast. Eng.*, *60*, 95–108, doi:10.1016/j.coastaleng.2011.09.001.

Beck, A. J., Y. Tsukamoto, A. Tovar-Sanchez, M. Huerta-Diaz, H. J. Bokuniewicz, and S. A. Sañudo-Wilhelmy (2007), Importance of geochemical transformations in determining submarine groundwater discharge-derived trace metal and nutrient fluxes, *Applied Geochemistry*, 22(2), 477-490.

Befus, K. M., M. B. Cardenas, D. V. Erler, I. R. Santos, and B. D. Eyre (2013), Heat transport dynamics at a sandy intertidal zone, *Water Resources Research*, *49*(6), 3770–3786. doi:10.1002/wrcr.20325.

Bokuniewicz, H., M. Pollock, J. Blum, and R. Wilson (2004), Submarine ground water discharge and salt penetration across the sea floor, *Ground Water*, *42*(7), 983–989, doi:10.1111/j.1745-6584.2004.tb02637.x.

Boufadel, M. C. (2000), A mechanistic study of nonlinear solute transport in a groundwater – surface water system under steady state and transient hydraulic conditions, *Water Resour.*, *36*(9), 2549–2565.

Boufadel, M. C., and A. M. Bobo (2011), Feasibility of High Pressure Injection of Chemicals into the Subsurface for the Bioremediation of the Exxon Valdez Oil, *Ground Water Monit. Remediat.*, *31*(1), 59–67, doi:10.1111/j1745.

Boufadel, M. C., Y. Xia, and H. Li (2011), Modeling solute transport and transient seepage in a laboratory beach under tidal influence, *Environmental Modelling & Software*, *26*(7), 899–912, doi:10.1016/j.envsoft.2011.02.005.

Bratton, J. F., J. K. Bohlke, F. T. Manheim, and D. E. Krantz (2004), Ground Water Beneath Coastal Bays of the Delmarva Peninsula: Ages and Nutrients, *Ground Water*, *42*(7), 1021–1034, doi:10.1111/j.1745-6584.2004.tb02641.x.

Cable, J. E., J. B. Martin, and J. Jaeger (2006), Exonerating Bernoulli? On evaluating the physical and biological processes affecting marine seepage meter measurements, *Limnol. Oceanogr. Methods*, *4*, 172–183.

Charbonnier, C., P. Anschutz, D. Poirier, S. Bujan, and P. Lecroart (2013), Aerobic respiration in a high-energy sandy beach, *Marine Chemistry*, *155*, 10–21, doi:10.1016/j.

Charette, M. A., and E. R. Sholkovitz (2006), Trace element cycling in a subterranean estuary: Part 2. Geochemistry of the pore water, *Geochim. Cosmochim. Acta*, *70*(4), 811–826, doi:10.1016/j.gca.2005.10.019.

Charette, M. A., and E. R. Sholkovitz (2002), Oxidative precipitation of groundwater-derived ferrous iron in the subterranean estuary of a coastal bay, Geophys. Res. Lett., 29(10), 1444, doi:10.1029/2001GL014512.

Charette, M. A., E. R. Sholkovitz, and C. M. Hansel (2005), Trace element cycling in a subterranean estuary: Part 1. Geochemistry of the permeable sediments, *Geochim. Cosmochim. Acta*, *69*(8), 2095–2109, doi:10.1016/j.gca.2004.10.024.

Cooper, H. H. (1959), A hypothesis concerning the dynamic balance of fresh water and salt Water in a coastal aquifer, *J. Geophys. Res.*, *64*(4), 461–467, doi:10.1029/JZ064i004p00461.

Gibbes, B., C. Robinson, L. Li, and D. Lockington (2007), Measurement of hydrodynamics and pore water chemistry in intertidal groundwater systems, *J. Coast. Res.*, *2007*(50).

Glover, R. E. (1959), The Pattern of Fresh-Water Flow in a Coastal Aquifer, *J. Geophys. Res.*, *64*(2), 457–459.

Gonneea, M. E., A. E. Mulligan, and M. A. Charette (2013), Climate-driven sea level anomalies modulate coastal groundwater dynamics and discharge, *Geophys. Res. Lett.*, *40*(11), 2701–2706, doi:10.1002/grl.50192.

Hays, R. L., and W. J. Ullman (2007), Direct determination of total and fresh groundwater discharge and nutrient loads from a sandy beachface at low tide (Cape Henlopen , Delaware), *Limnol. Oceanogr.*, *52*(1), 240–247.

Heiss, J. W., W. J. Ullman, and H. A. Michael (2014), Swash zone moisture dynamics and unsaturated infiltration in two sandy beach aquifers, *Estuar. Coast. Shelf Sci.*, *143*, 20–31, doi:10.1016/j.ecss.2014.03.015.

Henderson, R. D., F. D. Day-Lewis, E. Abarca, C. F. Harvey, H. N. Karam, L. Liu, and J. W. Lane (2009), Marine electrical resistivity imaging of submarine groundwater discharge: sensitivity analysis and application in Waquoit Bay, Massachusetts, USA, *Hydrogeol. J.*, *18*(1), 173–185, doi:10.1007/s10040-009-0498-z.

Huettel, M., W. Ziebis, S. Forster (1996), Flow-induced uptake of particulate matter in permeable sediments, *Limnology and Oceanography*, 41, 309–322.

Johannes, R. E. (1980), The ecological significance of the submarine discharge of groundwater, *Mar. Ecol. Prog. Ser.*, *3*, 365–373.

Jun, S. -C., G. -O. Bae, and K. -K. Lee (2013), Factors causing dynamic variations in the saltwater–freshwater transition zone in a beach aquifer, Mangsang, South Korea, *Hydrogeol. J.*, 21(6), 1355–1371, doi:10.1007/s10040-013-0995-y.

King, J. N., A. J. Mehta, and R. G. Dean (2009), Generalized analytical model for benthic water flux forced by surface gravity waves, J. Geophys. Res., 114(C04004), doi:10.1029/2008jc005116.

Kohout, F. A. (1960), Cyclic flow of salt water in the Biscayne aquifer of southeastern Florida, *J. Geophys. Res.*, *65*(7), 2133–2141, doi:10.1029/JZ065i007p02133.

Kraft, J. C. (1971), The migration of Holocene sedimentary environments in coastal Delaware, *North American Contenental Shelf: Quaternaria*, 14, 23-38.

Kroeger, K. D., and M. A. Charette (2008), Nitrogen biogeochemistry of submarine groundwater discharge, *Limnol. Oceanogr.*, *53*(3), 1025–1039, doi:10.4319/lo.2008.53.3.1025.

Kuan, W. K., G. Jin, P. Xin, C. Robinson, B. Gibbes, and L. Li (2012), Tidal influence on seawater intrusion in unconfined coastal aquifers, *Water Resour. Res.*, *48*(2), 1–11, doi:10.1029/2011WR010678.

Langevin, C. D., D. T. Thorne Jr, A. M. Dausman, M. C. Sukop, and W. Guo (2008), SEAWAT version 4: A computer program for simulation of multi-species solute and heat transport, Technical Report, in U.S. Geological Survey Techniques and Methods Book 6, Chapter A22, 39 pp.

Lebbe, L. (1999), Parameter identification in fresh-saltwater flow based on borehole resistivities and freshwater head data, *Adv. Water Resour.*, *22*(8), 791–806.

Lenkopane, M., A. D. Werner, D. A. Lockington, and L. Li (2009), Influence of variable salinity conditions in a tidal creek on riparian groundwater flow and salinity dynamics, *J. Hydrol.*, *375*(3-4), 536–545, doi:10.1016/j.jhydrol.2009.07.004.

Li, L., D. A. Barry, F. Stagnitti, and J. Y. Parlange (1999), Submarine groundwater discharge and associated chemical input to the coastal sea, *Water Resources Research*, (35)11, 3253-3259.

Li, H., M. C. Boufadel, and J. Weaver (2008), Tide-induced seawater–groundwater circulation in shallow beach aquifers, *J. Hydrol.*, *352*(1-2), 211–224, doi:10.1016/j.jhydrol.2008.01.013.

Li, X., B. X. Hu, W. C. Burnett, I. R. Santos, and J. P. Chanton (2009), Submarine ground water discharge driven by tidal pumping in a heterogeneous aquifer., *Ground Water*, *47*(4), 558–68, doi:10.1111/j.1745-6584.2009.00563.x.

Mao, X., P. Enot, D. A. Barry, L. Li, A. Binley, and D. –S. Jeng (2006), Tidal influence on behaviour of a coastal aquifer adjacent to a low-relief estuary, *Journal of Hydrology*, *327*(1-2), 110–127. doi:10.1016/j.jhydrol.2005.11.030.

Michael, H. A., J. S. Lubetsky, C. F. Harvey (2003), Characterizing submarine groundwater discharge: a seepage meter study in Waquoit Bay, Massachusetts, *Geophys. Res. Lett*., 30(6), 1297, doi.org/10.1029/2002GL016000.

Michael, H. A., Mulligan, A. E., and Harvey, C. F. (2005), Seasonal oscillations in water exchange between aquifers and the coastal ocean, *Nature*, 436, 1145–1148.

Michael, H. A., M. A. Charette, and C. F. Harvey (2011), Patterns and variability of groundwater flow and radium activity at the coast: A case study from Waquoit Bay, Massachusetts, *Mar. Chem.*, *127*(1-4), 100–114, doi:10.1016/j.marchem.2011.08.001.

Miller, D., and W. J. Ullman (2004), Ecological consequences of ground water discharge to Delaware Bay, United States, *Ground Water*, *42*(7), 959–970, doi:10.1111/j.1745-6584.2004.tb02635.x.

Moore, W. S. (1996), Large groundwater inputs to coastal waters revealed by 226Ra enrichments, *Nature*, *380*, 1996.

Moore, W. S. (1999), The subterranean estuary: A reaction zone of ground water and sea water, *Mar. Chem.*, 65, 111–125.

Moore, W. S., J. L. Sarmiento, and R. M. Key (2008), Submarine groundwater discharge revealed by 228Ra distribution in the upper Atlantic Ocean. *Nat. Geosci*. 1, 309– 311.

Post, V. E. (2011), A new package for simulating periodic boundary conditions in MODFLOW and SEAWAT, *Computers and Geosciences*, *37*(11), 1843–1849. doi:10.1016/j.cageo.2011.01.012.

Precht, E., and M. Huettel (2003), Advective pore-water exchange driven by surface gravity waves and its ecological implications, *Limnol. Oceanogr*., 48(4), 1674–1684, doi:10.4319/lo.2003.48.4.1674.

Riedl, R. J., N. Huang, and R. Machan (1972), The subtidal pump: a mechanism of interstitial water exchange by wave action, *Marine Biology*, 13, 210–21

Robinson, M., D. Gallagher, and W. Reay (1998), Field observations of tidal and seasonal variations in groundwater discharge to tidal estuarine surface water, *Groundwater Monit. Rem.*, *18(1)*, 83–92.

Robinson, C., B. Gibbes, and L. Li (2006), Driving mechanisms for groundwater flow and salt transport in a subterranean estuary, *Geophys. Res. Lett*., 33, L03402, doi:10.1029/2005GL025247.

Robinson, C., B. Gibbes, H. Carey, and L. Li (2007a), Salt-freshwater dynamics in a subterranean estuary over a spring-neap tidal cycle, *J. Geophys. Res.*, *112*(C9), 1–15, doi:10.1029/2006JC003888.

Robinson, C., L. Li, and D. A. Barry (2007b), Effect of tidal forcing on a subterranean estuary, *Adv. Water Resour.*, *30*(4), 851–865, doi:10.1016/j.advwatres.2006.07.006.

Robinson, C., L. Li, and H. Prommer (2007c), Tide-induced recirculation across the aquifer-ocean interface, *Water Resour. Res*., 43(7), 1–14, doi:10.1029/2006WR005679.

Robinson, C., A. Brovelli, D. A. Barry, and L. Li (2009), Tidal influence on BTEX biodegradation in sandy coastal aquifers, *Adv. Water Resour.*, *32*(1), 16–28, doi:10.1016/j.advwatres.2008.09.008.

Robinson, C., P. Xin, L. Li, and D. A. Barry (2014), Groundwater flow and salt transport in a subterranean estuary driven by intensified wave conditions, *Water Resour. Res.*, *50*, 165 – 181, doi:10.1002/2013WR013813.

Roy, M., J. B. Martin, J. E. Cable, and C. G. Smith (2013), Variations of iron flux and organic carbon remineralization in a subterranean estuary caused by inter-annual variations in recharge, *Geochim. Cosmochim. Acta*, *103,* 301–315, doi:10.1016/j.gca.2012.10.055.

Russoniello, C. J., C. Fernandez, J. F. Bratton, J. F. Banaszak, D. E. Krantz, A. S. Andres, L. F. Konikow, H. A. Michael (2013), Geologic effects on groundwater salinity and discharge into an estuary, *Journal of Hydrology*, *498*, 1–12, doi:10.1016/j.jhydrol.2013.05.049.

Santoro, A. E. (2010), Microbial nitrogen cycling at the saltwater–freshwater interface, *Hydrogeol. J.*, *18*(1), 187–202, doi:10.1007/s10040-009-0526-z.

Santos, I. R., W. C. Burnett, J. Chanton, B. Mwashote, I G. N. A. Suryaputra, and T. Dittmar, (2008), Nutrient biogeochemistry in a Gulf of Mexico subterranean estuary and groundwater-derived fluxes to the coastal ocean, *Limnology and Oceanography*, 53, 705-718, doi:10.4319/lo.2008.53.2.0705.

Santos, I. R., B. D. Eyre, and M. Huettel (2012), The driving forces of porewater and groundwater flow in permeable coastal sediments: A review, Estuarine Coastal Shelf Sci., 98,1–15, doi:10.1016/j.ecss.2011.10.024

Sawyer, A. H., O. Lazareva, K. D. Kroeger, K. Crespo, C. S. Chan, T. Stieglitz, and H. A. Michael (2014), Stratigraphic controls on fluid and solute fluxes across the sediment-water interface of an estuary, *Limnol. Oceanogr.*, *59*(3), 997–1010, doi:10.4319/lo.2014.59.3.0997.

Sawyer, A. H., F. Shi, J. T. Kirby, and H. A. Michael (2013), Dynamic response of surface water-groundwater exchange to currents, tides, and waves in a shallow estuary, *J. Geophys. Res. Ocean.*, *118*(4), 1749–1758, doi:10.1002/jgrc.20154.

Shum, K. T., and B. Sundby (1996), Organic matter processing in continental shelf sediments – the subtidal pump revisited, *Marine Chemistry*, 53, 81–87.

Simmons, G. M. (1992), Importance of submarine groundwater discharge (SGWD) and seawater cycling to material flux across the sediment/water interfaces in marine environments, *Mar. Ecol. Prog. Ser*., 84, 173–184.

Slomp, C. P., and P. Van Cappellen (2004), Nutrient inputs to the coastal ocean through submarine groundwater discharge: controls and potential impact, *J. Hydrol.*, *295*, 64–86, doi:10.1016/j.jhydrol.2004.02.018.

Smith, C. G., J. E. Cable, and J. B. Martin (2008), Episodic high intensity mixing events in a subterranean estuary: Effects of tropical cyclones, *Limnol. Oceanogr.*, *53*(2), 666–674.

Spiteri, C., C. P. Slomp, M. A. Charette, K. Tuncay, and C. Meile (2008), Flow and nutrient dynamics in a subterranean estuary (Waquoit Bay, MA, USA): field data and reactive transport modeling, *Geochim. Cosmochim. Acta*, 72, 3398–3412.

Taniguchi, M., W. C. Burnett, J. E. Cable, and J. V. Turner (2002), Investigation of submarine groundwater discharge, *Hydrol. Process*, 16, 2115–2129.

Turner, I. L., and R. I. Acworth (2004), Field measurements of beachface salinity structure using cross-borehole resistivity imaging, *J. Coastal Res*., 20(3), 753–760.

Ullman, W. J., B. Chang, D. C. Miller, and J. A. Madsen (2003), Groundwater mixing, nutrient diagenesis, and discharges across a sandy beachface, Cape Henlopen, Delaware (USA), *Estuarine, Coastal Shelf Sci*., 57, 539-52.

Vandenbohede, A., and L. Lebbe (2005), Occurrence of salt water above fresh water in dynamic equilibrium in a coastal groundwater flow system near De Panne, Belgium, *Hydrogeol. J.*, *14*(4), 462–472, doi:10.1007/s10040-005-0446-5.

Vera, I., I. Marino-Tapia, and C. Enriquez (2012), Effects of drought and subtidal sea-level variability on salt intrusion in a coastal karst aquifer, *Mar. Freshw. Res.*, *63*, 485–493.

Vukovic, M., Soro, A., 1992. Determination of Hydraulic Conductivity of Porous Media from Grain-Size Composition. Water Resources Publications, Littleton, CO,

Werner, A. D., and D. A. Lockington (2006), Tidal impacts on riparian salinities near estuaries, *J. Hydrol.*, *328*(3-4), 511–522, doi:10.1016/j.jhydrol.2005.12.011.

Wilson, A. M., W. S. Moore, S. B. Joye, J. L. Anderson, and C. A. Schutte (2011), Storm-driven groundwater flow in a salt marsh, *Water Resour. Res.*, *47*(2), 1–11, doi:10.1029/2010WR009496.

Wood, C., and G. A. Harrington (2014), Influence of seasonal variations in sea level on the salinity regime of a coastal groundwater-fed wetland, *Groundwater*, doi:10.1111/gwat.12168.

Xin, P., C. Robinson, L. Li, D. A. Barry, and R. Bakhtyar (2010), Effects of wave forcing on a subterranean estuary, *Water Resour. Res*., 46, W12505, doi:10.1029/2010WR009632.

Chapter 3

COUPLED SURFACE-SUBSURFACE HYDROLOGIC MEASUREMENTS REVEAL INFILTRATION, RECHARGE, AND DISCHARGE DYNAMICS ACROSS THE SWASH ZONE OF A SANDY BEACH

This work has been published as Heiss, J. W., J. A. Puleo, W. J. Ullman, and H. A. Michael (2015), Coupled surface-subsurface hydrologic measurements reveal infiltration, recharge, and discharge dynamics across the swash zone of a sandy beach, *Water Resour. Res.*, 51, 8834–8853, doi:10.1002/2015WR017395.

ABSTRACT

Swash-groundwater interactions affect the biogeochemistry of beach aquifers and the transport of solutes and sediment across the beachface. Improved understanding of the complex, coupled dynamics of surface and subsurface flow processes in the swash zone is required to better estimate chemical fluxes to the sea and predict the morphological evolution of beaches. Simultaneous high-frequency measurements of saturation, water table elevation, and the cross-shore locations of runup and the boundary between the saturated and unsaturated beachface (surface saturation boundary) were collected on a sandy beach to link groundwater flow dynamics with swash zone forcing. Saturation and lysimeter measurements showed the dynamic response of subsurface saturation to swash events and permitted estimation of infiltration rates. Surface and subsurface observations revealed a decoupling of the surface saturation boundary and the intersection between the water table and the beachface. Surface measurements alone were insufficient to delineate the infiltration and discharge zones, which moved independently of the surface saturation

boundary. Results show for the first time the motion and areal extent of infiltration and recharge zones, and constrain the maximum size of the subaerial discharge zone over swash and tidal time scales. The width of the infiltration zone was controlled by swash processes and subaerial discharge was controlled primarily by tidal processes. These dynamics reveal the tightly coupled nature of surface and subsurface processes over multiple timescales, with implications for sediment transport and fluid and solute fluxes through the hydrologically and biogeochemically active intertidal zone of sandy beaches.

3.1 Introduction

Groundwater-surface water interactions in the intertidal zone are recognized as an important factor in beach biogeochemistry and morphology. Fluid exchange across the aquifer-ocean interface can lead to mixing between seawater and discharging fresh groundwater in coastal aquifers. Mixing can alter the biogeochemistry of sandy beach aquifers [e.g., Charette and Sholkovitz, 2002; Kroeger and Charette, 2008; Spiteri et al., 2008; Santoro, 2010; Anwar et al., 2014; McAllister et al., 2015] and influence solute concentrations in groundwater prior to discharge [Santos et al., 2008; Roy et al., 2010; Sawyer et al., 2014]. Seawater can also introduce organic matter and dissolved oxygen to shallow beach sediments, driving aerobic and anaerobic respiration [McLachlan et al., 1985; Ullman et al., 2003; Orr et al., 2005; Charbonnier et al., 2013].

Groundwater-surface water exchange also affects sediment transport processes by altering the thickness of the boundary layer and the effective weight of the sediment [Nielsen, 1992]. Infiltration during runup increases bed shear stress due to a thinning of the boundary layer which promotes onshore sediment transport while simultaneously increasing the effective weight of immersed sediment, which decreases the potential for onshore sediment transport. The opposite occurs during rundown when discharge thickens the boundary layer and reduces shear stress. This decreases the potential for offshore transport, but effective sediment weight is simultaneously reduced due to discharge, promoting offshore sediment transport. The effects of infiltration and discharge on the relative importance of effective sediment weight versus boundary layer effects have been numerically [e.g. Masselink and Li, 2001; Karambas 2003; Hoque and Asano, 2007; Bakhtyar et al. 2011] and experimentally [Turner and Masselink, 1998; Butt et al. 2001] investigated. Effective sediment weight dominates and offshore transport is promoted for grain sizes below 0.4 mm to 0.6 mm. For larger grain sizes, the effects of a modified boundary layer dominate and net transport is onshore [Karambas, 2003; Butt et al., 2001].

The swash zone, the area between wave rundown and the location of maximum wave runup, is a dynamic area of groundwater-surface water exchange and is thus important to the biological, biogeochemical, and morphological evolution of beaches. Within the swash zone, the location of the intersection of the water table and beach surface has been termed the exit point (Turner, 1993) because it can mark a divide between zones of infiltration and discharge (Figure 3.1). Where that is the case, vertical infiltration occurs landward of the exit point across an intermittently saturated beachface, while subaerial groundwater discharge occurs seaward of the exit point across the permanently saturated lower beachface (Figure 3.1). Farther seaward, submarine groundwater discharge occurs below the tide level (Figure 3.1). Pore pressure response to swash motion below the infiltration and discharge zones has been investigated in a number of field and modeling studies [e.g. Waddell, 1976; Packwood and Peregrine, 1980; Hegge and Masselink, 1991; Turner and Nielsen, 1997; Horn et al., 1998; Turner and Masselink, 1998; Baldock et al., 2001; Butt et al., 2001]. These studies demonstrated that pore pressure response generally decreases with distance landward and depth below the sand surface. The resulting hydraulic gradients drive vertical flow across the beachface. Field, laboratory, and numerical modeling investigations have shown that vertical flow landward of the exit point within the swash zoneis spatially and temporally variable [McLachlan et al., 1985; Kang et al., 1994; Steenhauer et al., 201l, 2012; Masselink and Turner, 2012; Heiss et al., 2014; Geng and Boufadel, 2015]. Infiltration within this zone affects saturation in the unsaturated zone as water flows downward to the water table [Steenhauer et al., 201l, 2012; Geng and Boufadel, 2015] and may contribute significantly to total flow through the beach aquifer [McLachlan et al., 1985; Heiss et al., 2014]. Groundwater discharge in the intertidal zone seaward of the exit point also varies over time and space [Turner and Masselink, 1998; Li et al., 1999; Butt et al., 2001; Hays and Ullman, 2007; Michael et al., 2011; Rosenberry et al., 2013]. The location of the exit point has been identified as the interface between the unsaturated and saturated beachface (hereafter referred to as the surface saturation boundary), the area seaward of which appears as a shiny and glassy surface [Aagaard and Holm, 1989; Holman et al., 1993; Cartwright et al., 2006; Puleo, 2009; Huisman et al., 2011; Vousdoukas, 2014].

The dynamics of the surface saturation boundary has been the focus of previous field studies investigating groundwater-surface water interactions in the swash zone. Red-green-blue (RGB) imaging systems have been used to identify and track the surface saturation boundary as a proxy for subaerial discharge at the time scale of individual swash events, as this technique provides continuous data collection at high spatial and temporal resolution [Aagaard and Holm, 1989; Holman et al., 1993; Puleo, 2009; Huisman et al., 2011; Vousdoukas, 2014]. The surface saturation boundary can also be tracked manually by visual inspection of the beachface [Cartwright et al., 2006]. The subaerial discharge zone can be monitored directly from water table measurements using a cross-shore transect of monitoring wells [Turner, 1993; Turner and Masselink, 1998; Huisman et al. 2011]. Huisman et al. [2011] combined observations of the surface saturation boundary with water table measurements and demonstrated that the surface saturation boundary corresponded to the location on the beachface where the water table was within 2 cm of the surface. In that study the surface saturation boundary was coincident with the exit point, was landward of the swash zone, and displayed low-frequency motion related to tidal phase. Others have shown that the surface saturation boundary moves across the beach in response to individual swash events [e.g. Cartwright et al., 2006; Puleo, 2009; Vousdoukas, 2014]. However, the extent to which the location and motion of the surface saturation boundary at the swash time scale is representative of the location and dynamics of the water table-beachface intersection remains unclear. Combined surface and subsurface observations at high temporal and spatial resolution are needed to investigate the extent of this coupling and to identify and the boundary between zones of groundwater-surface water exchange

In addition to the need to better link surface conditions to infiltration and discharge zones, there is a need to connect surface conditions to flow in the unsaturated zone. Coupling between swash and groundwater flow in the saturated zone has been investigated extensively. Pore pressure fluctuations in the saturated beach in response to runup have been tied to surface dynamics such as the location of the leading edge of the swash lens (hereafter referred to as the swash edge) [Hegge and Masselink, 1991], swash velocity [Butt et al., 2001] and depth [Turner and Masselink, 1998], the location across the swash zone [Austin and Masselink, 2001], surf zone conditions [Sous et al., 2013], and proximity to the surface saturation boundary [Cartwright et al., 2006]. However, fewer field studies have instrumented the unsaturated zone to monitor unsaturated groundwater flow in response to swash processes [e.g. Horn et al., 1998; Baldock et al., 2001; Heiss et al., 2014]. Although these three field studies offer valuable insight into unsaturated flow processes, the measurements were limited to the subsurface. Pore pressure [e.g. Horn et al., 1998] and subsurface water content [e.g. Heiss et al., 2014] measurements collected within the unsaturated zone have revealed a region of nearly saturated sediment immediately below the sand surface that forms as a result of swash inundation and infiltration across the unsaturated beachface. A zone of unsaturated sediment divides the recharge lens from the water table at depth [Figure 3.1; Horn et al., 1998; Heiss et al, 2014] until saturation occurs due to a combination of the downward movement of the recharge lens and a rising water table and capillary fringe from below [Heiss et al., 2014]. Steenhauer et al. [2011] conducted laboratory experiments to couple the swash edge location with unsaturated flow. They used digital imaging techniques and pore pressure measurements in a series of carefully controlled tests in cemented and immobile sediment to demonstrate important linkages between the location of the swash edge and the dynamics of the recharge lens including its shape, horizontal and vertical extent, volume, and downward velocity following a dam break-driven swash event. The results revealed decoupling between swash and unsaturated flow where the recharge lens continued to move downward through unsaturated sediment to the water table following rundown. Most infiltrating water in the laboratory beach with 1.5 mm diameter sediment remained in the shallow unsaturated zone and moved downward slowly. In sediment of 8.5 mm diameter the recharge lens was thicker and moved downward more rapidly. The water table-beachface intersection was also decoupled from the swash edge in both beaches. The findings demonstrate that infiltration into and flow though the unsaturated zone should be considered when evaluating subsurface flow behavior. Austin and Masselink [2006] used pore pressure measurements below the water table in the swash zone and observed similar decoupling behavior in a steep gravel beach. The saturated pore pressure measurements were used to infer a downward motion of the recharge lens to the water table. However the structure and dynamics of the recharge lens and flow through the unsaturated zone were not directly examined. As a result, it remains unclear how the swash edge, surface saturation boundary, and exit point are coupled to pore water flow through the unsaturated zone over multiple swash events and over a tidal cycle in a natural beach setting.

We expand on previous studies by simultaneously measuring surface and subsurface processes to investigate the coupling between the swash edge and surface saturation boundary, and the groundwater dynamics in the saturated and unsaturated zones of a sandy beach aquifer. The objectives of this work are to 1) investigate the dynamics of infiltration and discharge zones as they relate to the location of the swash edge, surface saturation boundary, and tide level, 2) link saturated and unsaturated flow processes with swash and tidal forcing, and 3) provide new insight into groundwater-surface water interactions within the swash zone.

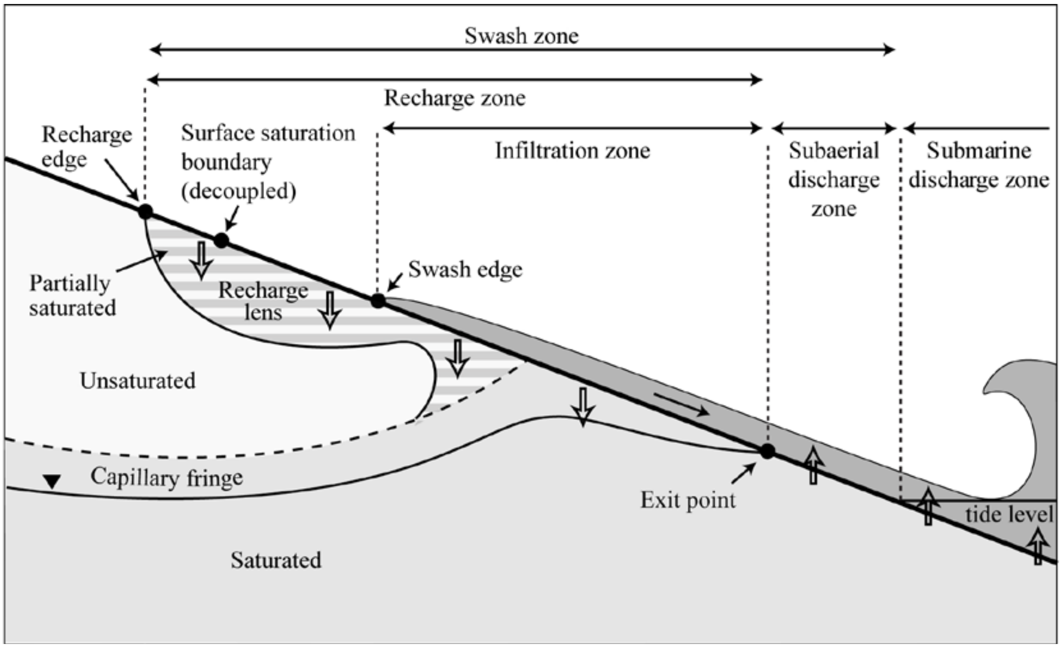

Figure 3.1. Schematic of surface water and groundwater levels in the swash zone. The locations of the infiltration, recharge, and discharge zones move

3.2 Field Experiment

3.2.1 Study Site

A field experiment was conducted on 27 June 2013 at Herring Point, Cape Henlopen, Delaware (38°45'51.8"N, 75°04'54.0"W) on the U.S. mid-Atlantic seaboard. Cape Henlopen is a sandy spit where longshore currents transport sediment northward along its Atlantic boundary. The morphology of the beach consists of a dune, a flat backshore, and a 30 m wide beachface with a 1:6 slope. Grain size analysis of sediment collected from the site indicate that the intertidal zone is comprised of medium sand with a median grain size of 0.39 mm. Constant head permeameter tests yielded a hydraulic conductivity of 21 m d^{-1}. Offshore significant wave height and period recorded 47 km to the southeast by the National Data Buoy Center Station

44009 during the experiment were 0.89 m and 8.7 s, respectively. Tides are semidiurnal with a range of 1.4 m between mean higher high water and mean lower low water (NOAA tidal station 8557830, Lewes, Delaware).

3.2.2 Instrumentation

Volumetric water content and water table elevation were monitored using a cross-shore transect of moisture sensors and pressure transducers (Figure 3.2). The transect was deployed in the section of the beach that extended from 3.5 m to 6.0 m landward of the high tide mark and included six instrument arrays separated horizontally by approximately 0.5 m. Each array, labeled Sites A through F in Figure 3.2, was outfitted with 5-6 moisture sensors (Decagon Devices EC-5) to measure volumetric water content at various depths in the unsaturated zone. Moisture sensors were pushed horizontally into the undisturbed sediment along the wall of an augured hole in an effort to measure water content at the natural bulk density of the beach. Volumetric water content was converted to local saturation at all moisture sensor locations using the porosity measured by each sensor. The sensors were installed in vertical arrays at depths of 2, 6, 10, 14, and 18 cm below the beach surface. An additional moisture sensor was installed at a depth of 24 cm at Site F. All arrays were equipped with a pressure transducer (Druck PTX 1835 or Druck PTX 1830) placed in the saturated zone to measure the water table, and four arrays had a second pressure transducer positioned at the sand surface to measure swash depth. A manometer with two 1 cm screens separated vertically by 40 cm was used to observe vertical head differences in the saturated beach below the swash zone in order to ensure that vertical flow was negligible and that pore pressure measurements could be used to estimate the water table height. The head difference was consistently $\leq$ 1.5 mm, which is within the measurement error of the pressure transducers and 3% of head fluctuations which were typically 5 cm. A pressure transducer was positioned in the inner surf zone to measure local incoming wave height and period. Cables were routed away from the transect and buried in a trench leading up the beach. Water content and pressure were recorded at 5 and 16 Hz, respectively.

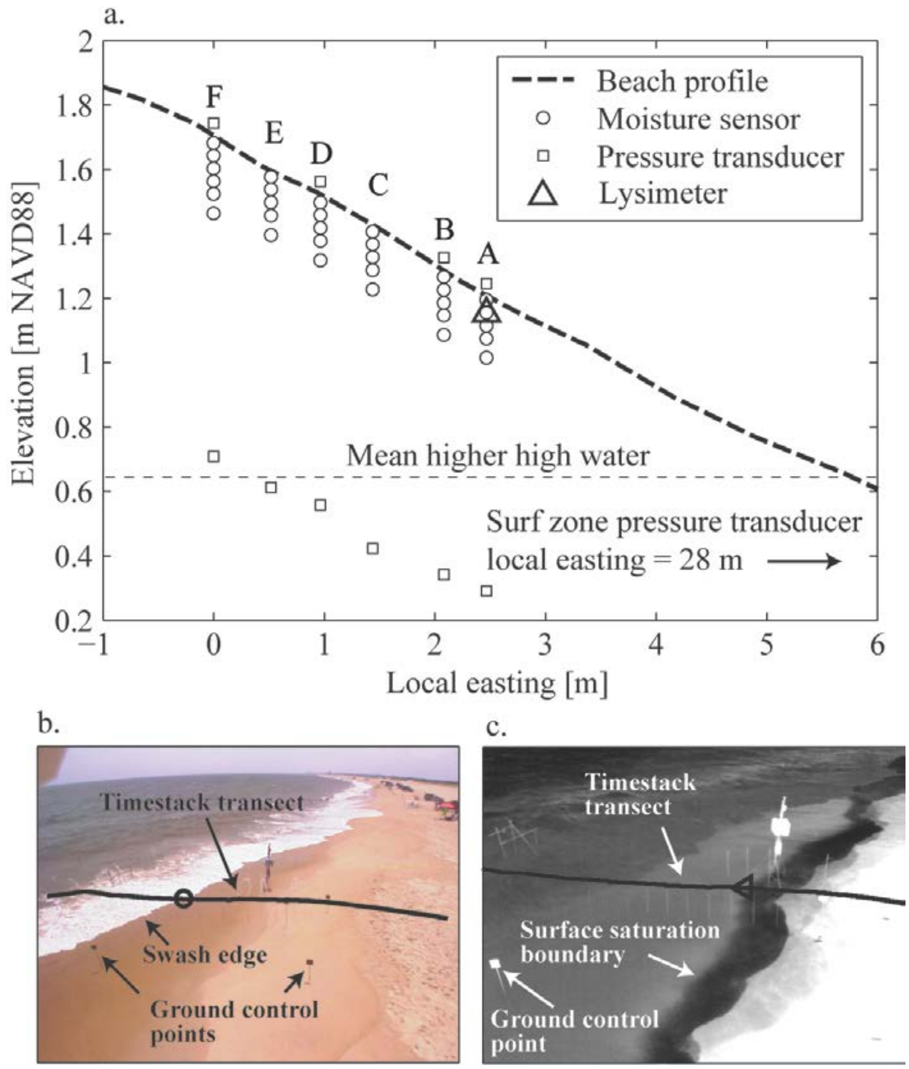

Figure 3.2. Instrument deployment for the field study. a) Sensor transect and beach profile. Labels A-F indicate vertical array site location. The triangle is the position of the lysimeter separated 0.5 m in the alongshore direction from the main cross-shore instrument transect. b) View from RGB imager showing swash edge (circle). c) View from thermal imager showing surface saturation boundary (triangle). The black curves in (b) and (c) are the pixel coordinates of the timestack transect.

The slope of the measured water table between the two most seaward pressure transducers was linearly extrapolated to the sand surface [e.g. Turner, 1993; Turner and Masselink, 1998; Huisman et al. 2011].The point of contact between the extrapolated water table and beachface is referred to as the extrapolated water table-beachface intersection. The distinction between the extrapolated water table-beachface intersection and the exit point is discussed in section 3.1.1.

The motion of the swash edge and surface saturation boundary were tracked using two different imagers. A Sony DFW-X710 RGB imager (1024 x 768 pixels) recorded visible-band imagery at 4 Hz to identify the swash edge. The image sequence was recorded as individual time-stamped frames as joint picture experiment group (jpeg) images. Thermal infrared imagery was captured using a FLIR systems SC645 imager (640 x 480 pixels) recording at 3.125 Hz to identify the surface saturation boundary. Thermal imagery was recorded using FLIR software in their proprietary format and later converted to a windows media file (.wmv) for analysis. The main focus for thermal imagery was the contrast between the saturated and unsaturated beachface. Therefore the actual kinetic temperature was not calculated. Parameters such as emissivity in the internal conversion from radiance to temperature were chosen based on water (0.98) and local conditions. Contrast was enhanced by altering the temperature scale versus image intensity within the image sequence prior to file conversion. The uncertainty in the location of the surface saturation boundary is estimated to be +/- 12 cm. This was calculated based on the slope of the beach (1:6) and the depth of the shallowest moisture sensors (2 cm), above which saturation could not be directly measured to confirm the imagery. This uncertainty is ~1% of the width of the swash zone during the experiment. Images were recorded in Coordinated

Universal Time (UTC) and converted to local time where the beginning of the run is relative to 13:33:00 UTC.

The imagers were mounted on top of a 6 m aluminum tower in the back beach 20 m orthogonal (in the alongshore) to the transect such that the field of view was oblique relative to the study area (Figure 3.2b-c). The location of the swash edge and surface saturation boundary were extracted from time stack images collected near the instrument transect. A time stack is a cross-shore transect of pixel intensity from each sequential frame in the image sequence [Aagaard and Holm, 1989; Holman et al., 1993; Holland and Holman, 1993]. The pixel coordinates of the cross-shore transect (Figure 3.2b-c; black curves) were identified in the image using a geometrical model (including lens distortion) based on the camera position and surveyed ground control points (rectangular targets in Figure 3.2b-c) within the image [Holland et al., 1997]. The model allows for conversion from real-world to pixel coordinates using the measured beach profile. The swash edge is clearly identifiable in the visible band [Aagaard and Holm, 1989; Holman et al., 1993; Puleo, 2009] while the surface saturation boundary is most pronounced in thermal images as a result of the temperature contrast between the dry and wet beach surface. An edge-detection algorithm based on pixel intensity differences was used to automatically detect the location of the two boundaries and hence the time history of the saturation and swash edge location. The algorithm is imperfect and requires manual correction where it clearly does not track the feature of interest. The amount of manual correction was estimated as 10% of the time series. A real time kinematic global position system (RTK-GPS) survey was performed on the day of the experiment quantifying the sensor positions, the local beach topography and the ground control points needed for geometrical transformation of images. Positions were collected in Universal Transverse Mercator (UTM) using North American Datum (NAD83) in the horizontal and North American Vertical Datum (NAVD88) in the vertical. Mean sea level in the area is roughly -0.1 m NAVD88. UTM coordinates were converted to a local northing-easting coordinate system with the origin at Site F to simplify understanding of distances on presented Figures.

The experiment began mid-way through rising tide, continued into high tide, and concluded mid-way into the following ebb tide for a total of 8.5 hours of data collection. Local significant wave height (0.57 m) was estimated as 4 times the standard deviation of the free surface elevation time series from the inner surf-zone pressure transducer after removing the tidal signal. The local mean period (5.2 s) was determined using the zero up-crossing method on the free-surface time series. Saturation and pressure were recorded to three data loggers (National Instruments and Campbell Scientific) and imagery was recorded to two laptop computers. All devices were time synchronized using a Garmin GPS antenna, and Tac32 and Dimension4 software.

Swash infiltration across the saturated beach landward of the extrapolated water table-beachface intersection was measured using a pan lysimeter [Jordan, 1968]. The lysimeter consisted of a cylinder constructed from 10 cm ID polyvinyl chloride (PVC) pipe with a length of 20 cm (see Thompson and Scharf, 1994). The bottom of the cylinder was sealed and the top was outfitted with a porous plate and mesh. A stand-alone pressure sensor placed in the lysimeter measured water depth at 2 Hz. Atmospheric pressure was maintained inside the device by venting the buried container to the sand surface with polyethylene tubing, providing an outlet for air as water flowed into the lysimeter. A perched water table must form along the top of the device in order for water to infiltrate [Jemison and Fox, 1992; Zhu et al., 2002]. Conventionally, pan lysimeters are buried in the unsaturated zone in agricultural and forested settings where pressure head is negative relative to the atmospheric pressure in the container. Consequently, soil suction can cause a considerable portion of flow to diverge around lysimeters yielding collection efficiencies that typically range between 10 and 60% of the total percolate [Russell and Ewel, 1985; Jemison and Fox, 1992; Zhu et al., 2002], with higher collection efficiencies under wet conditions and large vertical flow rates [Peters and Durner, 2009]. Initial laboratory and field tests at the study site indicated that the lysimeter collected infiltrating water across the lower saturated swash zone when the capillary fringe was at the sand surface, resulting in apparent collection efficiencies greater than 350%. A 2.5 cm divergence control tube [e.g. Bews et al., 1997] was added to the top of the lysimeter to calibrate the device to a collection efficiency near 100%. The control tube was filled with sand finer than the ambient sediment to impede flow into the device and to promote formation of a perched water table. A benchtop test was performed for the lysimeter in a chamber filled with sediment from the study site. Water was added to the sand surface at various periods (5 s -100 s) and to a range of depths (1 cm - 35 cm) to simulate swash inundation. Collection efficiencies ranged from 95-116%. Efficiencies greater than 100% were found when the period between inundation events was 5 s - 25 s and inundation depths were 10 cm - 35 cm. Efficiencies from 95-100% occurred for inundation events with longer periods (25 s - 100 s) and shallower depths (1 cm - 7 cm), the typical range for swash during the experiment. The pan lysimeter was installed 6 cm below the sand surface at Site A to test its utility for measuring saturated swash infiltration across the seaward swash zone and to compare saturated infiltration rates to unsaturated infiltration rates farther landward.

Swash-driven infiltration across the unsaturated beachface was calculated using saturation profiles from the vertical arrays of moisture sensors (see Heiss et al. [2014] for a more detailed description of the methodology). The technique is similar to the numerical scheme developed by Talbot and Ogden [2008] where infiltration is estimated as the difference between subsurface saturation before and after an infiltration event. Saturation at the shallowest sensor was the first to increase following swash inundation of the beachface at each site. It was assumed that once saturation at the shallowest sensor peaked, the volume of infiltrating water was enclosed within the region extending from the sand surface to 10 cm. This was based on the observation that saturation at the shallowest sensor began to decline before rising at the third deepest sensor at 10 cm depth (saturation at sensors below this depth remained constant for the swash events considered). The volume of water that infiltrated the beach due to individual swash events at each site is calculated as the difference in the saturation, accounting for porosity, along the vertical profile immediately prior to swash inundation (T1) and at the time that the shallowest sensor signal peaked (T2). By fitting a line to the vertical profile at time T1 and an exponential function at time T2, unsaturated swash infiltration per swash event D_{su} is:

$$D_{su} = \int_{-z_{MS3}}^{0} S_{T2}(z)dz - \int_{-z_{MS3}}^{0} S_{T1}(z)dz \tag{1}$$

where $S_{T2}(z)$ is the saturation S as a function of depth z at $T2$, $S_{T1}(z)$ is the saturation as a function of depth at $T1$, and Z_{MS3} is the depth of the third moisture sensor from the surface.

Infiltration for 6 closely spaced swash events was calculated using equation (1) and the results were paired with the lysimeter values for the same set of swash events to develop an infiltration profile from the seaward saturated swash zone to the landward unsaturated swash zone.

3.3 Results

The imagers captured the location of the swash edge and surface saturation boundary. The swash edge is identifiable in the visible-band time stack by the bright rapidly moving feature across the beachface (Figure 3.3a). The surface saturation boundary is shown in the thermal imagery as the bright, more slowly seaward moving feature (Figure 3.3b). The effect of the tide on the location of the swash edge and surface saturation boundary is evident from the curvature of the time series over the duration of the experiment (Figure 3.3c-d). The transect was landward of the runup limit from the start of the experiment to 5000 s and was periodically inundated by swash events from 5000 s to 22500 s (Figure 3.3c). The surface saturation boundary also passed over the transect from 5000 s to 22500 s, indicating that the instruments were located in the landward portion of the swash zone (Figure 3.3d).

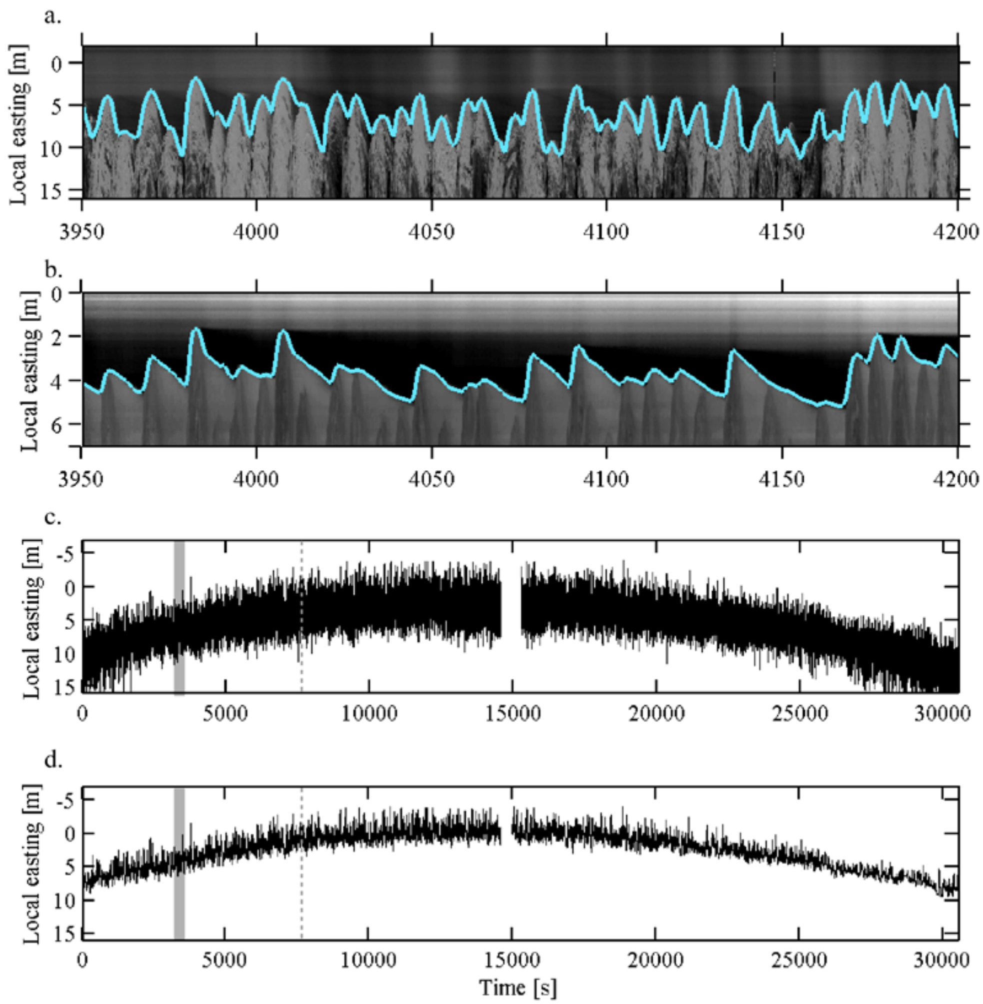

Figure 3.3. Swash zone runup and surface saturation boundaries. a) Example visible-band RGB time stack imagery for a period of 250 s, showing detected swash edge in blue. The grayscale is pixel intensity; b) example thermal time stack imagery showing surface saturation boundary in blue for the same period as (a). The grayscale is temperature mapped to pixel intensity; entire c) runup and d) surface saturation boundary time series extracted from the timestacks. The gray shading in (c) and (d) shows the time range presented in (a) and (b). The dotted vertical gray line in (c) and (d) shows the time presented in Figure 4. Local easting is meters relative to the farthest landward site (Site F). Negative easting is landward and positive easting is seaward.

3.3.1 Saturation beneath the Swash Zone

3.3.1.1 Identification of Surface and Subsurface Features

The surface and subsurface features shown in Figure 3.1 were identified from the field measurements. The instantaneous data from 7650 s (Figure 3.4) is used to illustrate these features. Swash infiltration occurred across the sand surface in the *infiltration zone*, defined as the area between the extrapolated water table-beachface intersection and the instantaneous location of the overriding swash edge (Figure 3.4). In effect, the infiltration zone was located landward of the extrapolated water table-beachface intersection where the beachface was currently inundated by swash. Saturation increased and then decreased in the unsaturated zone after the swash edge receded, hence there was downward vertical flow during times when the swash edge was seaward of the transect. This indicates that recharge was occurring where instantaneous infiltration was not. The region of vertical unsaturated flow is the *recharge lens* (see black contour in Figure 3.4), defined as the aquifer region where saturation was changing beneath the swash zone. The area of the beachface directly above the recharge lens and including the infiltration zone is the *recharge zone*. The *recharge edge* marks the landward extent of the recharge zone on the beachface.

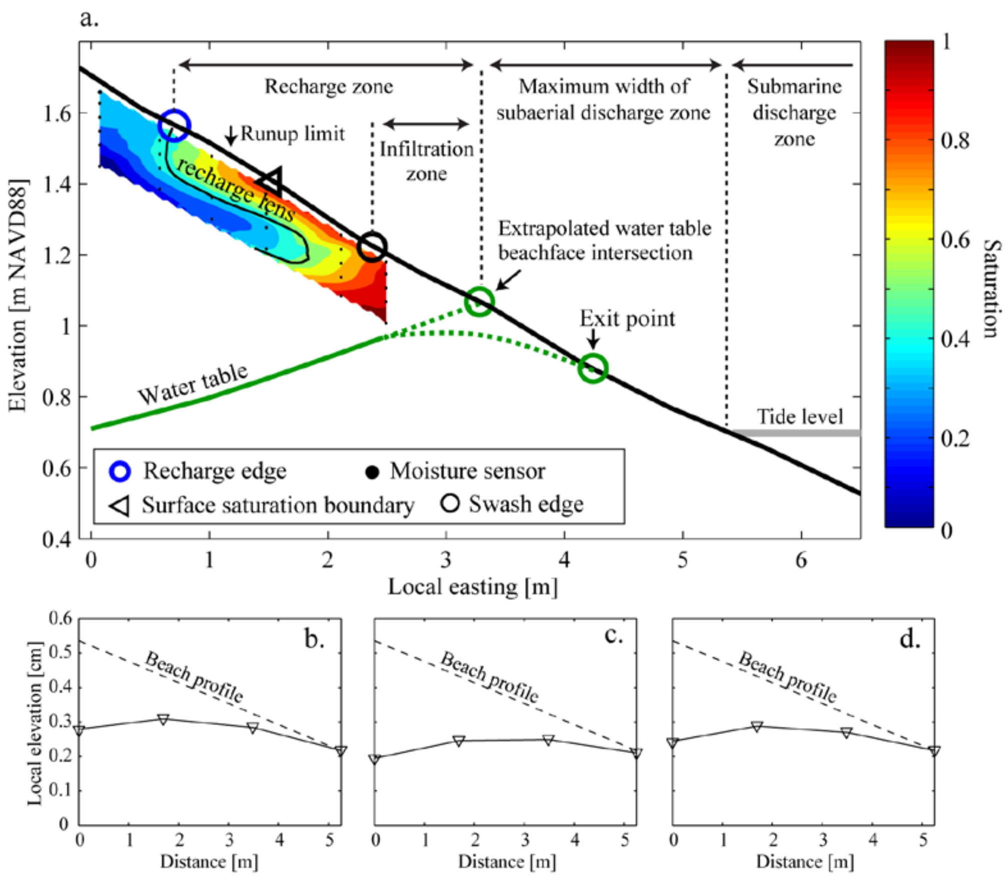

Figure 3.4. Instantaneous surface and subsurface conditions during rising tide at 7640 s (see Figure 3c and 3d. a) Subsurface saturation, water table, surface features and surface zonation. 0 indicates fully unsaturated conditions and 1 indicates fully saturated conditions. The black contour is the boundary of the recharge lens. Dashed green lines indicate potential water table configurations seaward of measurements. Measured water table mound at b) low, c) mid, and d) high tide marks from *Heiss et al.*, [2014].

The vertical flow direction across the sand surface seaward of the extrapolated water table-beachface intersection is unclear due a lack of measurements in that zone and the resulting uncertainty in the slope of the water table in that section of the beach. When a water table mound exists due to swash infiltration, the seaward swash zone is characterized by a subaerial discharge zone with an exit point seaward of the extrapolated water table and extending to the cross-shore location of the tide level (Figure 3.4a). Conversely, the same region of the beachface can be characterized as a zone of subaerial recharge if the water table slopes landward. In this work it is assumed that a water table mound and exit point were present seaward of the transect based on previously reported observations from a variety of natural and laboratory beaches [e.g. Keng et al., 1994, Boufadel et al., 2007, Steenhauer et al., 2011; Masselink and Turner, 2012; Turner and Masselink, 2012] and at this field site [Heiss et al., 2014]. Heiss et al. [2014] monitored the water table elevation farther seaward in the swash zone and observed mounding near the low, mid, and high tide marks (Figure 3.4b-d). Thus, the prior data support the existence of a water table mound and exit point on the rising tide, and because it is more likely that a mound exists on a falling tide, it is assumed that they exist throughout the tidal cycle at this site. A *subaerial discharge zone* exists between the exit point and the tide level (Figure 3.1). The location of the exit point could only be quantified near high tide because the exit point was located seaward of the measurement transect for the rest of the monitoring period. The extrapolated water table-beachface intersection is used to constrain the location of the exit point when the exit point is seaward of the transect. It is tracked as the farthest possible landward location of the exit point and constrains the maximum width of the subaerial discharge zone (Figure 3.4a). Additional discharge seaward of the tide level likely occurs in the *submarine discharge zone*.

The recharge lens and its origin due to infiltration was previously discussed in Heiss et al. [2014]. In the next three sections those findings are extended by describing the structure of the recharge lens and saturation dynamics as they relate to the swash edge, the surface saturation boundary, and the tide levels over swash event and tidal time scales. The dynamics of the infiltration, recharge, and discharge zones are discussed in Section 3.3.

3.3.1.2 Saturation Dynamics at the Swash Time Scale

Subsurface saturation was less dynamic than the swash edge. Figure 3.5a illustrates the conditions immediately prior to a swash event that inundated the sand surface within the full transect. Swash inundation that occurred prior to the time in Figure 3.5a produced a recharge lens in the upper 10 cm of sediment that extended landward to x = 1.1 m. The recharge edge moved landward roughly 0.5 m as the swash edge overrode Site F at 25 s (Figure 3.5b and h). Approximately 3 s later the recharge edge shifted beyond the landward limit of the transect (Figure 3.5c and h), and therefore could not be mapped in Figure 3.5h. Saturation increased marginally from 2-6 cm depth between Sites D and F in the time period between the initial subsurface conditions and the arrival of the second large swash event at 45 s (Figure 3.5c-d). It was not until after this second swash event at 45 s (Figure 3.5e) that saturation in the landward half of the unsaturated zone increased substantially due to infiltration (Figure 3.5d-e). Saturation in the shallow sediment at Site F then decreased and the recharge edge moved seaward back within the transect (Figure 3.5f). The dampened movement of the recharge edge compared to the swash edge indicates that downward flow in the unsaturated zone and recharge to the aquifer continues after the swash recedes.

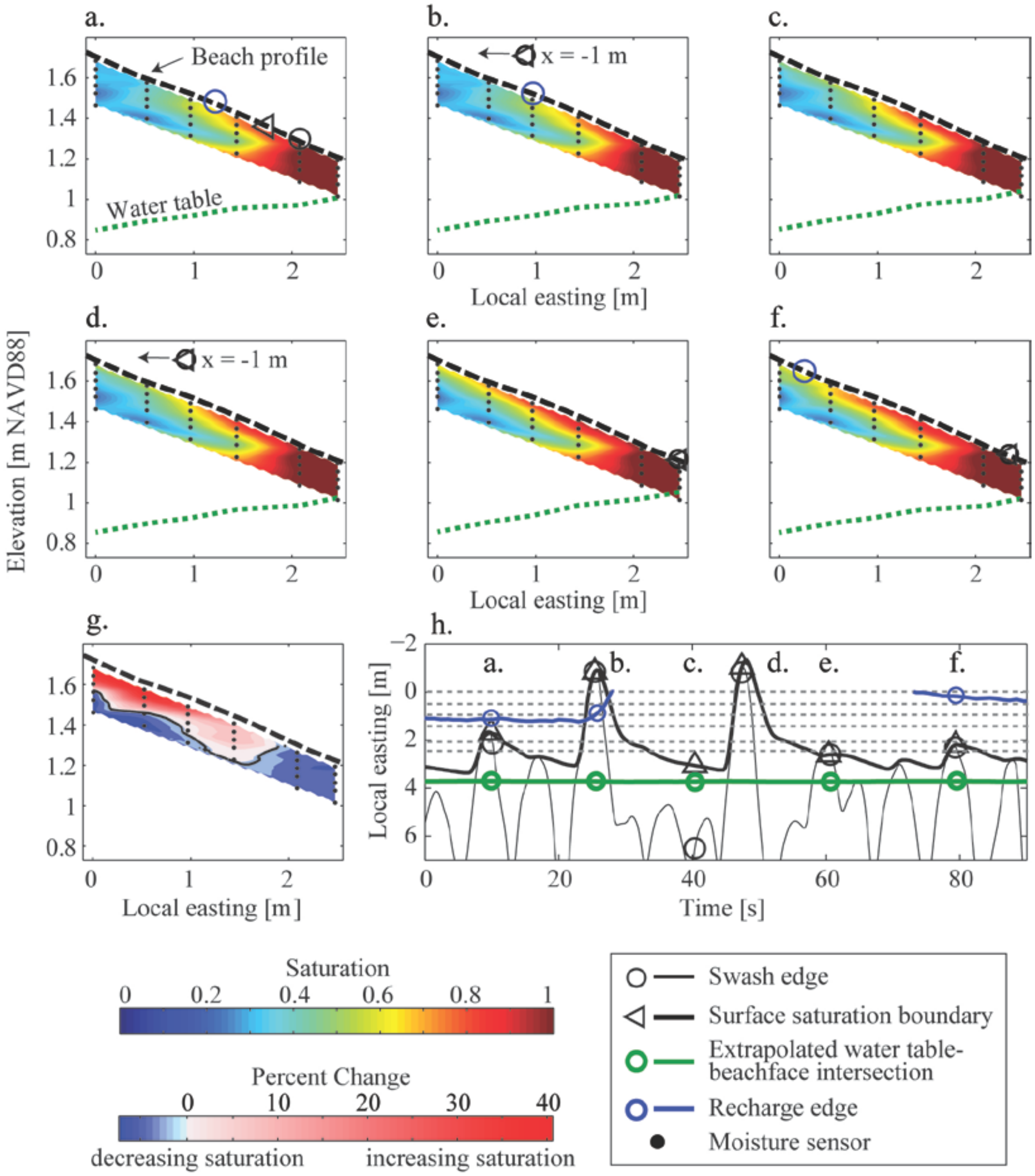

Figure 3.5. Subsurface saturation and surface features through two swash events that inundated the instrument transects between 8970 s and 9039 s a-f) Subsurface saturation and water table before, during, and immediately following two swash events that inundated the full extent of the instrument transect. g) Percent change in saturation between panels (a) and (f). Dashed horizontal lines in (h) are the cross-shore positions of the instrument sites. The positions of the swash edge, surface saturation boundary, and recharge edge at the times shown in the cross-sections are indicated in panel (h).

The movement of the lateral boundary between saturated and unsaturated sediments in the subsurface over swash events was muted compared to that at the surface (Figure 3.6). The subsurface saturation boundaries were defined by moisture measurements greater than 95% of saturation at that location, due to uncertainty in porosity and precision of the measurements. The surface saturation boundary moved up the beach 3.3 m in response to the swash event at 18 s while the subsurface saturation boundary at 2 cm depth moved 0.51 m. The dampening effect was more pronounced deeper in the unsaturated zone where the subsurface saturation boundary moved 0.38 m at 6 cm depth and 0.07 m at 10 cm depth (Figure 3.6). Analysis of the movement of the subsurface saturation boundary relative to that of the surface saturation boundary for 5 swash events indicates an exponential decay in the magnitude of fluctuation with depth (Figure 3.7a). The symbols in Figure 3.7 represent the 5 swash events that prompted a movement of the subsurface saturation boundary at all depths. The difference in the magnitude of the fluctuations demonstrates that infiltrating water entered the shallow unsaturated zone rapidly before draining more slowly downward at depth. The rapid and pulsed vertical infiltration resulted in large fluctuations in downward flow near the surface while more steady downward flow deeper in the unsaturated zone resulted in smaller changes in subsurface saturation.

In addition to dampening, there was a time lag between the movement of the surface saturation boundary and the subsurface saturation response over individual swashes. The time lag was calculated as the elapsed time between the arrival of the landward limit of the surface saturation boundary and the landward limit of the subsurface saturation boundary at a particular depth. The time lag between the surface and subsurface saturation boundary increased linearly by 1.7 s cm-1 into the subsurface (Figure 3.7b). This time lag is a result of downward flow of water infiltrated during each swash event.

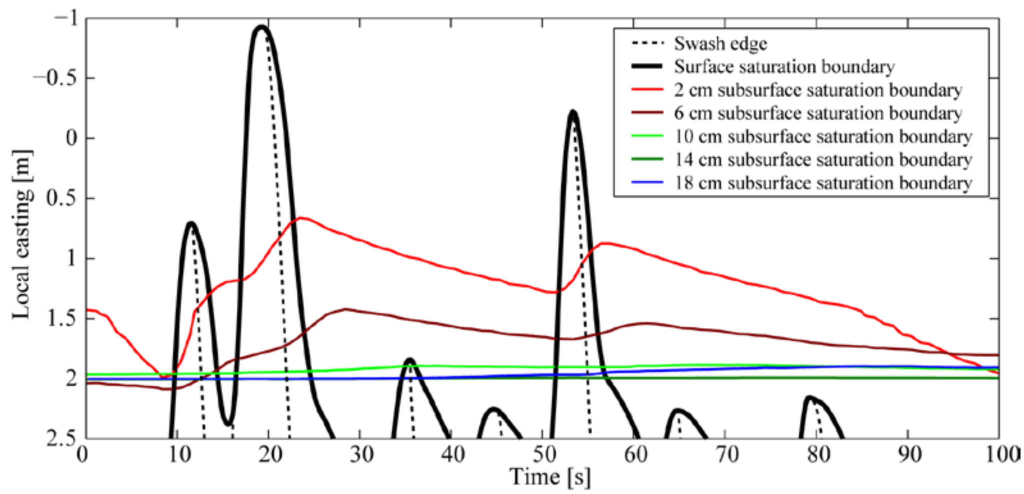

Figure 3.6. Cross-shore position of the swash edge, surface saturation boundary, and subsurface saturation boundaries at selected depths in the swash zone. Seaward is to the bottom of the Figure. Time is relative to 8200.

Subsurface saturation in the landward reaches of the swash zone experienced the largest fluctuations in response to swash inundation due to the lower frequency of swash events reaching this section of the beach and lower overall levels of saturation near the beach surface (Figure 3.8). Only the largest swash events were able to reach this region of the swash zone, allowing for greater infiltration into dryer and well-drained sediments compared to farther seaward. The findings are consistent with the pattern of increasing infiltration rates landward in the swash zone observed by Heiss et al. [2014].

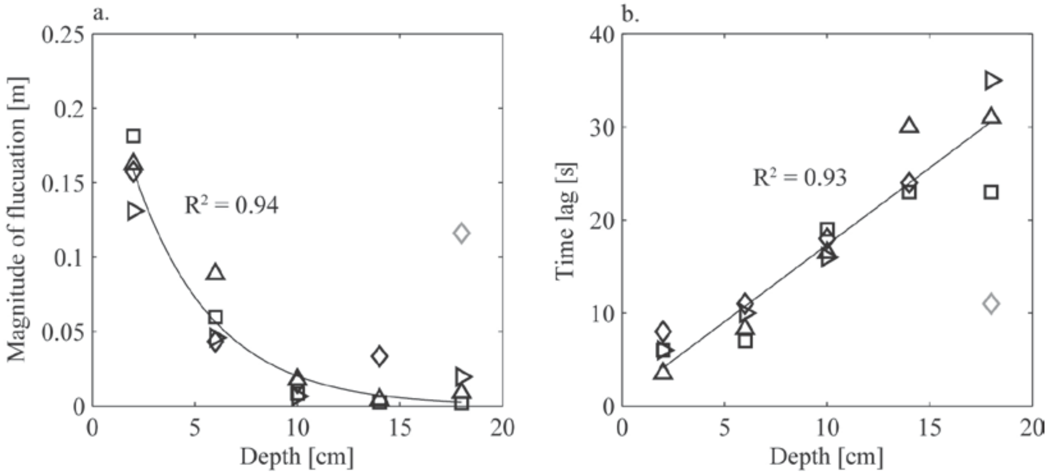

Figure 3.7. Surface and subsurface saturation boundary response. a) Magnitude of the fluctuation of the subsurface saturation boundary at various depths normalized to the movement of the surface saturation boundary for each swash event; b) time lag between the instance of the most landward extent of the subsurface saturation boundary relative to that of the surface saturation boundary as a function of depth. The gray symbols represent fluctuations and time lags caused by underlying water table oscillations and were therefore not included in the curve fitting procedure. R^2 is the coefficient of determination of the fitted curves.

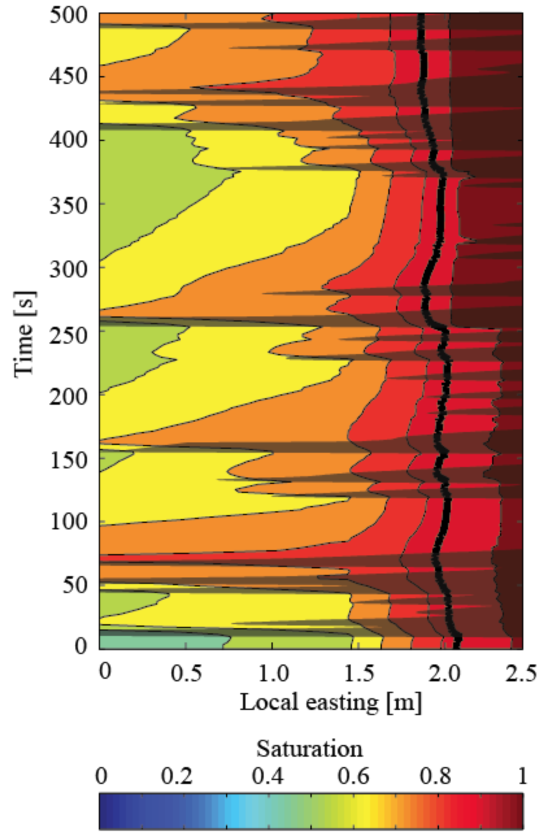

Figure 3.8. Subsurface saturation across the instrument transect at 2 cm depth. The subsurface saturation boundary (defined as 95% saturation) is shown by the thick black line. The position of the surface saturation boundary is shown by the area shaded black. Seaward is to the right. Time is relative to 8200 s.

3.3.1.3 Saturation Dynamics over a Tidal Cycle

On a tidal timescale, the aquifer sediments near the high tide mark varied from almost fully saturated to unsaturated. The recharge lens appeared immediately following the first swash event that inundated the transect and became more well-defined as the swash zone moved landward due to the rising tide (Figure 3.9a-c). Swash infiltration and a rising water table eventually saturated the shallow and deeper regions of the initially unsaturated zone, respectively (Figure 3.9d-e). Subsurface saturation reached a maximum 60 minutes before high tide (Figure 3.9f) and began to decline between x = 0 and 1 m 50 minutes after high tide (Figure 3.9g). The offset was caused by swash infiltration, which maintained saturated conditions up to 4 m landward of the tide level. Enough pore water was able to drain from the beach to result in lower subsurface saturation only when the swash zone moved seaward of each measurement location. Subsurface saturation in the landward portion of the swash zone decreased further as the water table and tide level fell (Figure 3.9h). Once the upper limit of the swash zone was seaward of the transect, the water table fell 0.17 m (Figure 3.9h-i). The seaward movement of the swash zone coincided with a further reduction in subsurface saturation throughout the measurement area (Figure 3.9i). These results demonstrate that the recharge lens was present during flood tide only. The absence of the recharge lens 2 hours following high tide was the result of the close proximity of water table and capillary fringe to the sand surface. The water table and capillary fringe maintained saturated conditions below the part of the beach that was periodically inundated and prevented the formation of a recharge lens. As a result, the unsaturated portion of the beachface was located farther landward in the swash zone compared to rising tide. Swash infiltration was limited to a few swash events large enough to extend over the wide saturated beachface and onto the unsaturated beachface.

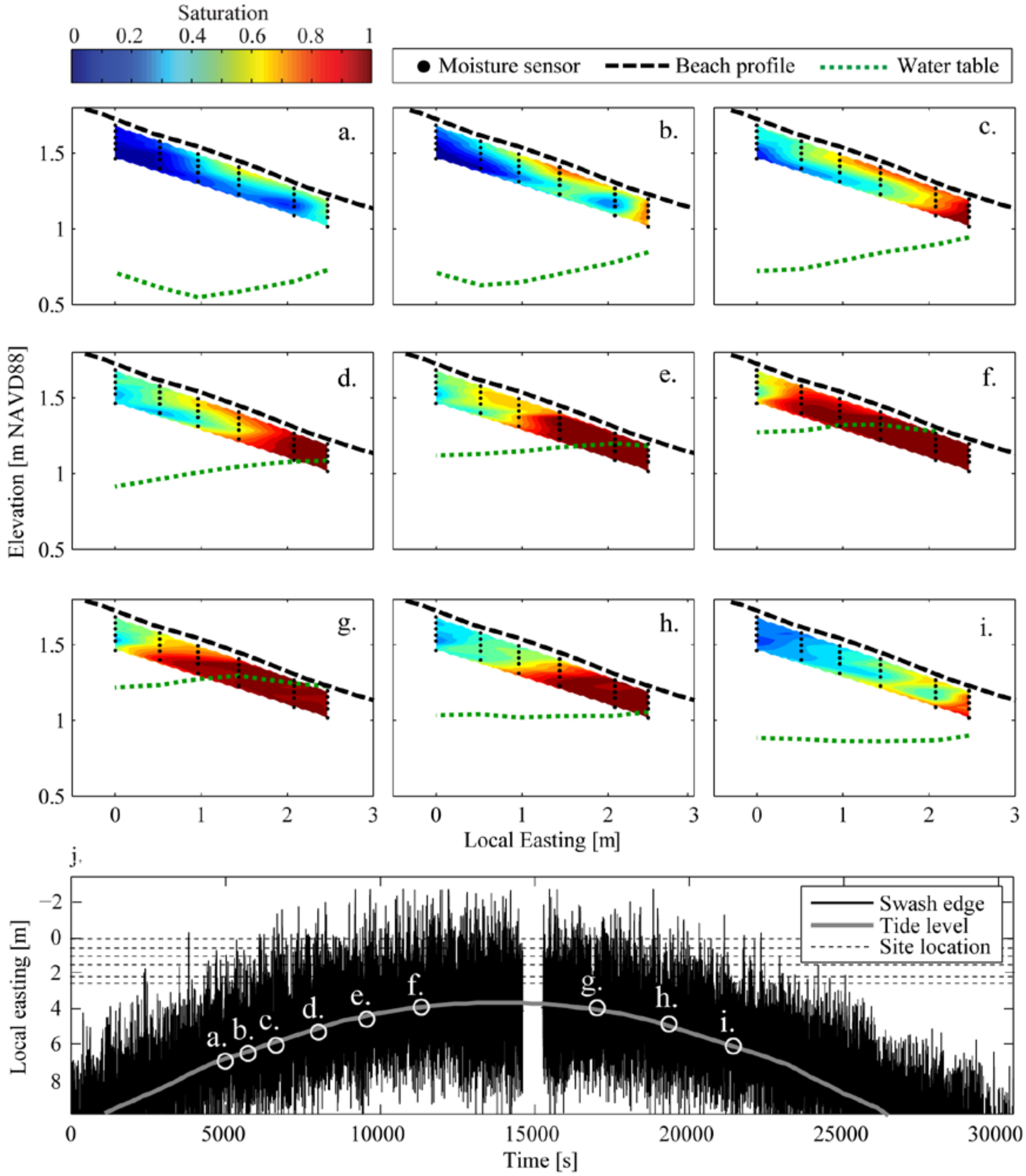

Figure 3.9. Subsurface saturation and water table elevation averaged over 15-minute intervals over the tidal cycle. The position of the tide level on the beachface at the times represented in the cross-sections is indicated by the labels in (j).

3.3.2 Mechanisms of Subsurface Saturation

Subsurface saturation occurred due to a combination of swash infiltration and a rising water table and capillary fringe, with the relative importance of each process depending on the position in the swash zone. At the seaward end of the transect at Site B, the initially unsaturated zone became saturated both from the sand surface downward and from the base of the unsaturated zone upward (Figure 3.10d-f). Downward saturation was due to swash infiltration whereas upward saturation was the result of a rising capillary fringe (since the water table was observed to be below the deepest moisture sensor). The rise of the capillary fringe coincided with a water table that rose due to swash-derived unsaturated flow from above in addition to lateral tidal inputs. The top of the capillary fringe is visible from 700 – 1600 s in Figure 3.10e and its thickness (20 cm) was taken as the distance between the water table and the 95% saturation contour directly above. The predicted thickness of 18 cm based on an empirical approximation [Turner and Nielsen, 1997] and the field site grain size (0.39 mm) agrees well with the observed thickness. The unsaturated zone decreased in thickness until infiltrating water merged with the capillary fringe at 1750 s. Infiltration farther landward at Site C led to higher saturation in the shallow unsaturated zone in comparison to Site B. For instance saturation greater than 50% at Site C extended to twice the depth of that at Site B (14 cm vs. 6 cm; Figure 3.10). Thus, pore space in the shallow unsaturated zone toward the seaward end of the swash zone filled with water due to swash infiltration, while the deeper portion succumbed to a capillary fringe rising together with the water table.

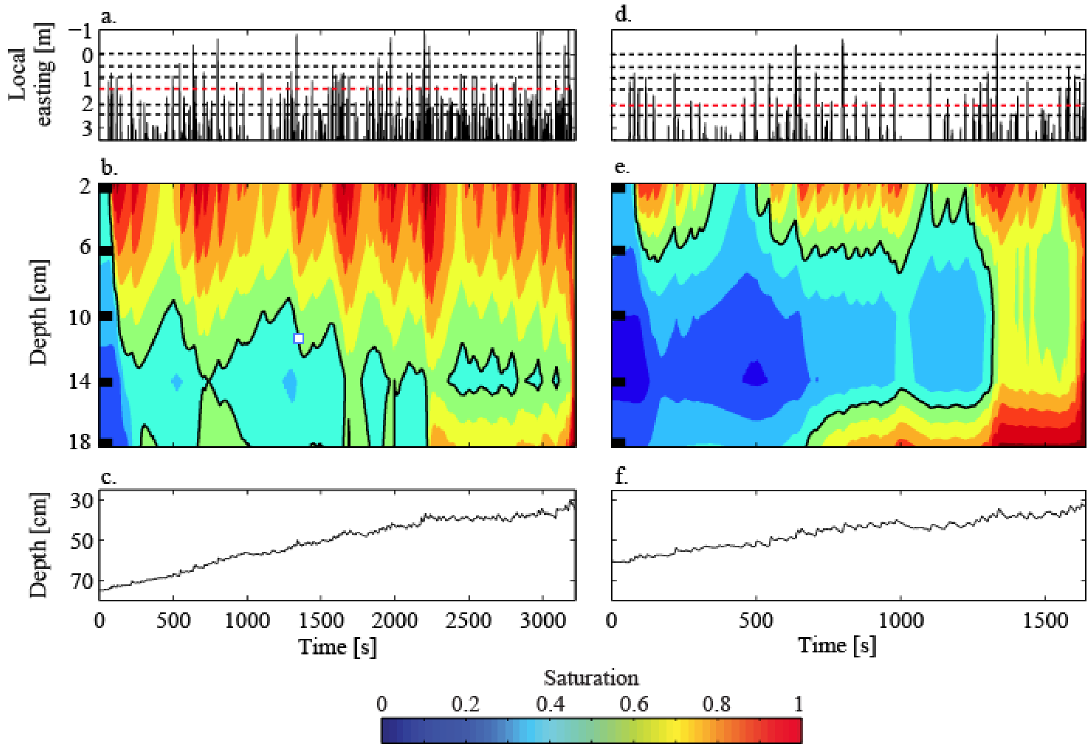

Figure 3.10. Vertical 1-D subsurface saturation profiles as a function of time at Site C (left panels) and Site B (right panels). a) Swash edge position; b) subsurface saturation, and c) water table depth at Site C. d) Swash edge position; e) subsurface saturation, and f) water table depth at Site B. The dashed horizontal lines are the cross-shore positions of the instrument sites. The red dashed horizontal line is the position of Site C (left) and Site B (right). The time frame in the right panels is of the first 1500 s of the time shown in the left panels because the array at Site B becomes fully saturated at 1800 s. The black filled rectangles on the y-axis show the depth of the moisture sensors. The black contours in b) and e) are 50% saturation. Time is relative to 6020 s.

3.3.3 Infiltration, Recharge, and Discharge Zone Dynamics

The surface saturation boundary and swash edge were coincident during runup and then diverged during rundown as the seaward movement of the surface saturation boundary lagged behind the more rapidly moving swash edge (Figure 3.11b). This finding is in agreement with previous field studies [e.g. Aagaard and Holm, 1989; Holman et al., 1993; Puleo, 2009; Huisman et al., 2011; Vousdoukas, 2014]. The surface saturation boundary was also consistently decoupled from the extrapolated water table-beachface intersection, which was located farther seaward and generally was the seaward limit of the surface saturation boundary (Figure 3.11b), which means that it was also decoupled from the exit point, confirming other studies demonstrating surface-subsurface flow decoupling [e.g. Austin and Masselink, 2006; Steenahuer et al., 2011]. The exit point was located within the permanently saturated beachface seaward of the surface saturation boundary and was undetectable from the surface. The dynamics of the extrapolated water table-beachface intersection, subsurface saturation, swash location, exit point, and tide level provide insight into the transient nature of the infiltration, recharge, and discharge zones across the beachface at the tidal and swash event time scale.

The zone of infiltration into the unsaturated zone was more extensive on rising tide than on falling tide, whereas the zone of subaerial discharge was larger on falling tide compared to rising tide. The extrapolated water table-beachface intersection and location of the tide on the beachface moved landward at similar rates from 0 to 5000 s and the distance between them, an indication of the maximum width of the subaerial discharge zone, remained roughly constant at 0.5 m (Figure 3.11a). The maximum width of the subaerial discharge zone increased to 1.5 m near high tide at 5000 s when the rate of rising tide began to slow and then doubled to 3 m during ebb tide as the rate of tidal fall outpaced the seaward movement of the extrapolated water table-beachface intersection (Figure 3.11a). Consequently the infiltration zone was narrower during ebb tide - the maximum extent of the subaerial discharge zone occupied a larger portion of the swash zone. The opposite occurred during rising tide where the maximum extent of the subaerial discharge zone was narrow and hence infiltration was more widespread.

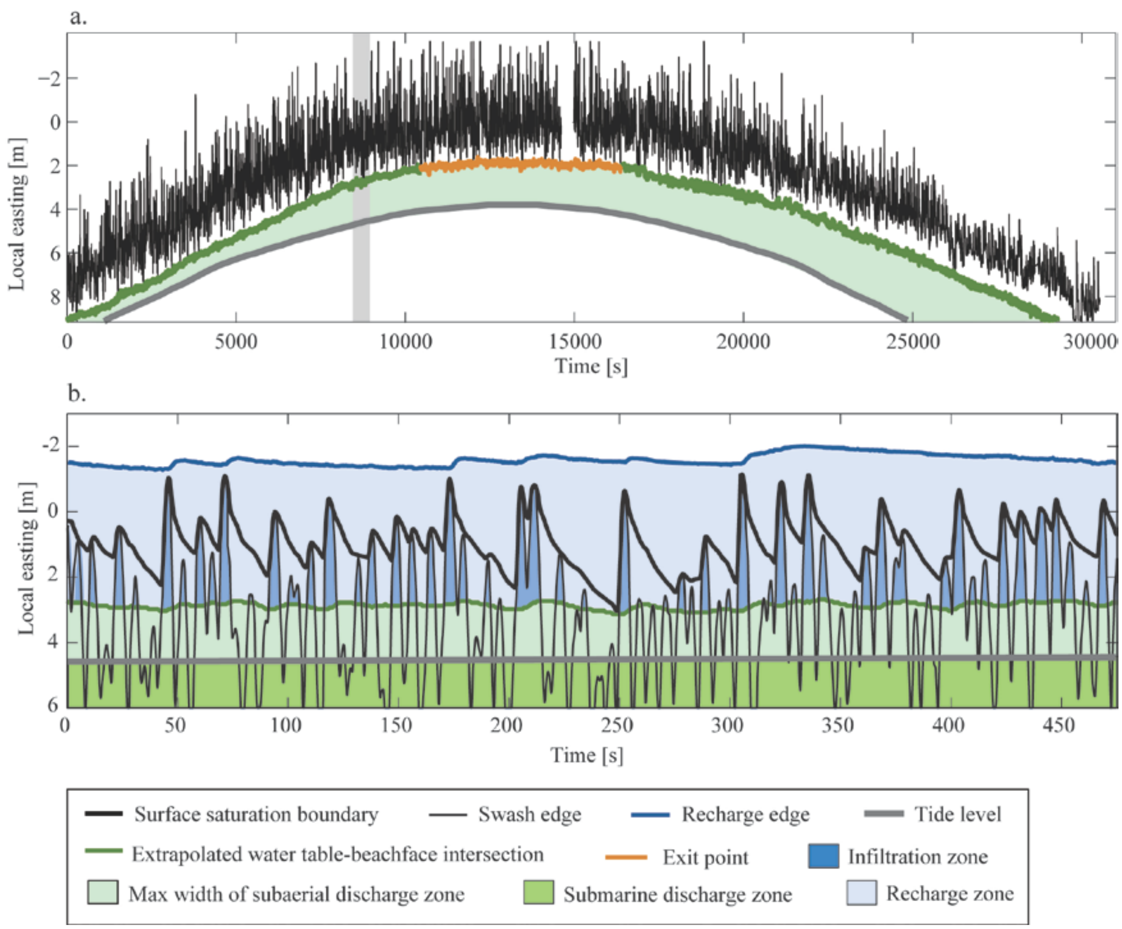

Figure 3.11. Infiltration, recharge, and discharge zones at the tidal and swash time scale. a) Surface saturation boundary, exit point, extrapolated water table-beachface intersection, tide level, and maximum width of the subaerial discharge zone on the beachface over the 8.5 hour data collection period; b) inset of shaded gray region in top panel over an 8 minute time interval with infiltration, recharge, subaerial discharge, and submarine discharge zones indicated. Seaward is to the bottom in both panels.

The width of the infiltration zone at the swash time scale was most variable, followed by the recharge zone, the subaerial discharge zone, and the submarine discharge zone. The width of the infiltration zone varied up to 7 m between swashes as it transited the intermittently saturated beachface with the swash edge. In contrast, the width of the recharge zone was less variable and shifted on the order of 0.5-1.0 m when the swash edge came to within a meter of the recharge edge (Figure 3.11b). The recharge edge was located in the farthest landward section of the swash zone, typically 0.5-1.5 m landward of the runup limit of the largest swash events (Figure 3.11b). The spatial offset between the recharge edge and the nearby runup limits suggests that landward flow occurs in the unsaturated zone in response to swash, consistent with the landward transport of microspheres in swash zone sediments observed by Gast et al., 2015. The extrapolated water table-beachface intersection, marking the maximum landward extent of the subaerial discharge zone, moved on the order of several centimeters between individual swash events (Figure 3.11b). The exit point was within the transect for approximately 1.3 hours near high tide and also moved on the order of several centimeters between swashes during that period (Figure 3.11a). Farther seaward, the landward extent of the submarine discharge zone was unchanged as shown by the tide level over the 475 s time period (Figure 3.11b). The results demonstrate that the width and location of the subaerial discharge zone were controlled primarily by the tide, and the width of the infiltration zone was controlled primarily by swash, while its location varied in response to both swash and the tide.

3.3.4 Cross-Shore Saturated and Unsaturated Infiltration Rates

The lysimeter collected infiltrating water driven by swash into the saturated portion of the beach within the capillary fringe. The moisture sensors confirmed that flow into the lysimeter did not occur until sediment surrounding the lysimeter was nearly or fully saturated. The time when the perched water table formed and collection began is shown in the beginning of the time series in Figure 3.12. Water depth inside the lysimeter increased with each swash event that inundated Site A (Figure 3.12b) and remained steady between events, forming the staircase pattern in Figure 3.12a. Infiltration ranged from 2 mm - 14 mm per swash event with greater infiltration generally occurring under longer duration swash events. The 2 mm - 14 mm infiltration range translates to a water table fluctuation of 7 mm - 47 mm assuming a porosity of 0.3 [e.g. Heiss et al., 2014] and agrees well with the observed 10 mm - 50 mm water table fluctuations over this time period, supporting the utility of lysimeters for measuring infiltration in the swash zone.

The lysimeter measurements of infiltration across the saturated beach and calculated infiltration based on saturation across the landward unsaturated beach provide an infiltration profile across the full swash zone. Infiltration per swash event increased in the landward direction from the saturated to unsaturated swash zone. Six swash events extended up to or beyond Site C between 200 s and 400 s (Figure 3.12a-b) and unsaturated infiltration was calculated for each event using equation (1). Unsaturated infiltration at Sites A and B could not be determined because the capillary fringe was in contact with the beach surface and hence there was no change in saturation. Estimated infiltration across the unsaturated beachface was lowest at Site C and increased to Site F (Table 1). Comparison between infiltration rates based on the lysimeter and saturation show that flow across the saturated portion of the swash zone was less than that across the unsaturated beachface. Average infiltration per swash was 8.1 mm across the saturated beach at Site A and 10.9 mm across the unsaturated beachface between Sites C and F. Infiltration was less across the saturated beach, likely due to the presence of the capillary fringe at the sand surface at the location of the lysimeter, which limited infiltration relative to the unsaturated swash zone. Although average infiltration per swash event increased landward from the saturated to unsaturated beachface, total infiltration over the 200 second time span did not increase monotonically landward because all six swash events did not reach the most landward sites. Thus, total inflow increased from Sites A to D before decreasing from Sites D to F.

Table 3.1. Calculated infiltration [mm] per swash event from lysimeter (Site A) and saturation (D_{su}, Sites C-F) measurements. Swash # corresponds to the labels in Figure 3.12a.

	Swash 1	Swash 2	Swash 3	Swash 4	Swash 5	Swash 6	Total	Average
Site A	7.6	4.6	12.7	4.8	11.5	7.4	48.6	8.1
Site C	8.5	5.1	13.6	5.3	12.5	7.8	52.8	8.8
Site D	9.1	5.5	14.9	5.8	13.5	8.4	57.2	9.5
Site E	-	-	16.1	6.0	14.2	9.0	45.3	11.3
Site F	-	-	16.9	-	15.2	9.9	42.0	14.0

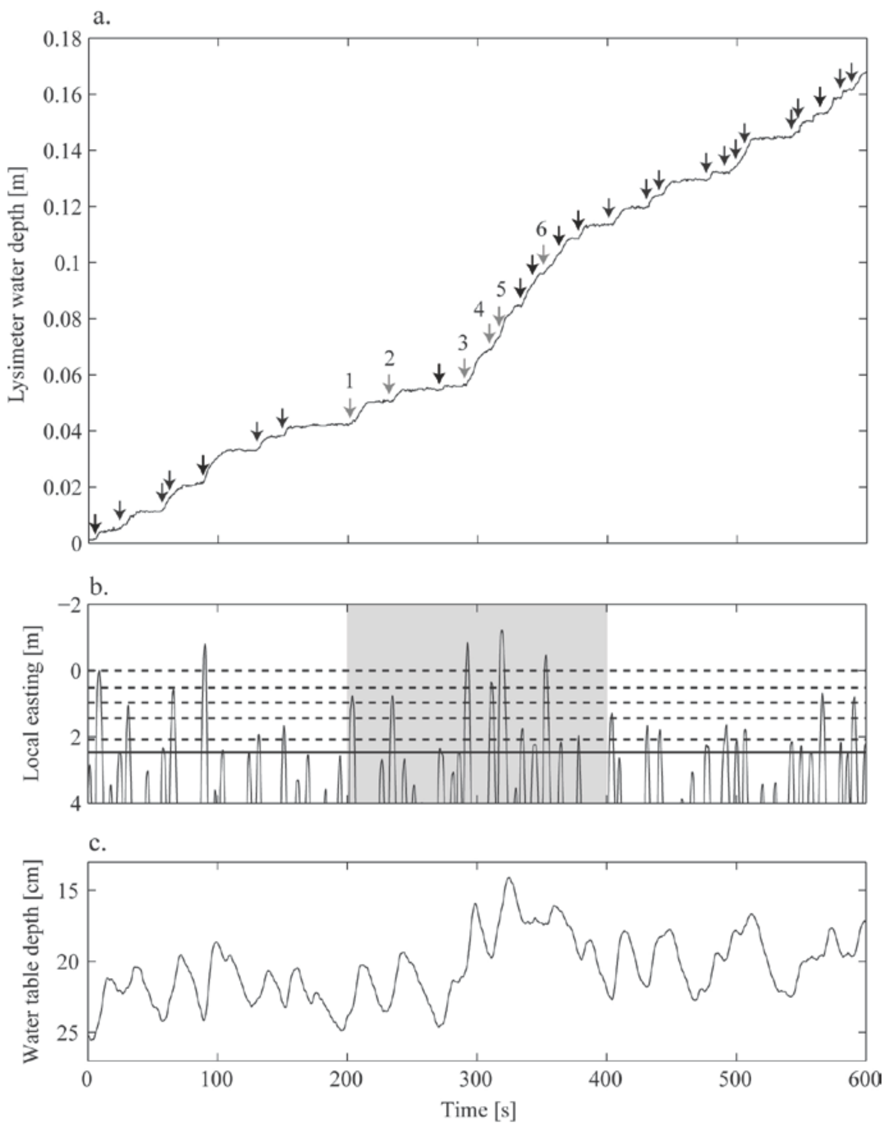

Figure 3.12. Lysimeter measurements and surrounding conditions. a) Water depth in the lysimeter at Site A. Black arrows indicate when Site A was inundated by swash. The gray arrows indicate the swash events where infiltration was calculated from moisture response, only events that inundated the beachface landward of Site A were used; b) cross-shore position of the swash edge. The gray shading is the time interval where infiltration was calculated using equation (1). The dashed horizontal lines are the cross-shore positions of the instrument sites. The solid horizontal line is the position of Site A; c) water table relative to the sand surface. Time is relative to 7900 s.

3.4 Discussion

3.4.1 Subsurface Observations Reveal Infiltration and Discharge Zones

The combined surface and subsurface measurements reveal previously unobserved groundwater-surface water interactions in the swash zone. Previous studies have used the surface saturation boundary as a proxy for the exit point on fine to very coarse grained beaches [e.g. Aagaard and Holm, 1989; Holman et al., 1993; Cartwright et al., 2006; Puleo, 2009; Huisman et al., 2011; Vousdoukas, 2014]. The results of this study suggest that the surface saturation boundary and exit point are distinct features on the beach that are consistently decoupled at swash and tidal time scales.

Subsurface saturation in the swash zone is affected by both infiltration and discharge processes. Infiltration occurs on the landward region of the beach beneath the part of the swash that overrides the exit point. The presence of a zone of infiltration across a portion of the saturated beachface contradicts the notion that the entirety of the saturated beachface seaward of the surface saturation boundary is a zone of groundwater discharge and verifies the laboratory findings of Steenhauer et al., [2011]. Thus, use of the surface saturation boundary to identify the location of the subaerial discharge zone may lead to an incorrect and large offset relative to its true location. The occurrence and magnitude of the offset will vary with beach slope, hydraulic conductivity, wave conditions, and width of the intertidal zone. The present results demonstrate that identifying the infiltration and subaerial discharge zones can be achieved only through coupled surface and subsurface measurements.

The decoupling between the surface saturation boundary and exit point has important implications for the dynamics of the infiltration, recharge, and discharge zones. Previous studies have used water table measurements to demonstrate that the exit point closely tracks tide level during rising tide, but becomes decoupled during ebb tide [e.g. Turner, 1993; Turner and Masselink, 1998]. Our results confirm these measurements and further show that the location and maximum width of the subaerial discharge zone is controlled primarily by the tide rather than individual swash events, even in the moderate wave-energy environment at Herring Point. The swash edge moved across a larger portion of the beachface compared to the extrapolated water table-beachface intersection, suggesting that the infiltration zone is more dynamic than the subaerial discharge zone. However, the recharge zone occupied an area that was more consistent in size than the dynamic infiltration zone. Observations on both rising and falling tides further indicate an asymmetry in infiltration and discharge. On rising tide, the size of the zone of infiltration is large relative to the maximum width of the subaerial discharge zone, whereas on falling tide the infiltration zone is smaller.

3.4.2 Implications for Biogeochemistry and Sediment Transport

Beach aquifers host a range of biogeochemical processes that affect the fluxes of dissolved materials from the coast to the ocean through SGD [Moore, 1999; Charette and Sholkovitz, 2006; Hays and Ullman, 2007; Santos et al., 2008; Santoro, 2010]. The maintenance of biogeochemical reactivity within the aquifer is in part dependent on the supply of labile organic carbon and oxygen that enters the beach through wave, tidal, and swash-driven processes. The location and nature of the addition of these seawater-derived constituents into the beach aquifer will affect their transport, degradation, and mixing with through-flowing freshened groundwater. This study demonstrates that infiltration occurs under both saturated and unsaturated conditions in the beachface, but is dynamic in both space and time. Much of the infiltration of water and associated solutes and particles occurs in the intermittently saturated zone in the upper part of the swash zone. However, the transport of reactive solutes and particles from their entry point in the infiltration zone to zones of reactivity in the subsurface ultimately relies on the dynamics of the groundwater flow system which can change over swash [e.g. Turner and Masselink, 1998; Sous et al., 2013; Heiss et al., 2014] and tidal cycles [e.g. Riedel et al., 2010; Befus et al., 2013; Heiss and Michael, 2014]. Because flow within the beach depends on hydraulic gradients and moisture conditions and thus on the location of the infiltration zone, which varies though the tidal cycle, the fate of reactive constituents will likely also differ with their entry point as the swash and infiltration zones move with the tide.

The relative size and location of the infiltration and discharge zones may also influence the stability of the beach. The present results show that a region of the saturated beachface is an area of infiltration implying a smaller subaerial discharge zone relative to what would be expected based on the full width of the saturated beachface. Infiltration and discharge play important roles in controlling the thickness of the boundary layer and bed shear stress, as well as impacting the effective weight of the sediment [Nielsen, 1992; Turner and Masselink, 1998; Masselink and Li, 2001; Bakhtyar et al. 2011], with the relative importance of boundary layer effects and effective sediment weight dependent on a critical grain size [e.g. Butt et al. 2001; Karambas 2003]. Thus, the modified size of infiltration and discharge zones relative to previous conceptual understanding that is based on beachface saturation is likely to be important for cross-shore sediment transport as boundary layer effects and the influence of effective sediment weight are adjusted accordingly. Moreover, additional loss of water from the swash lens to the subsurface during runup in comparison to that which would occur over a discharge zone could enhance differences in velocity and flow duration between runup and rundown potentially altering cross-shore sediment transport.

3.5 Conclusions

High-frequency surface and subsurface measurements in the swash zone together with simultaneous measurements of saturation and water table elevation within the beach and the position of the swash edge and surface saturation boundary on the beachface provide new insights into the coupled behavior of swash processes, tides, infiltration, and aquifer recharge and discharge in the intertidal zone.

A region of elevated saturation is formed in the shallow unsaturated zone due to swash infiltration across the unsaturated beachface. This recharge lens indicates vertical unsaturated flow to the water table. The landward extent of the lens responds to swash, but its motion is muted relative to the rapidly moving swash edge, indicating that downward flow in the unsaturated zone and recharge to the aquifer continues after runup. The recharge lens is present only during flood tide because few swash events are capable of overriding a widening subaerial discharge zone during ebb tide.

The initially unsaturated zone becomes saturated due to a combination of vertical infiltration from above and a rising water table and capillary fringe from below, with the relative importance varying with location on the beach. Vertical infiltration is the dominant subsurface saturation mechanism in the landward swash zone, while a rising water table and capillary fringe is more significant farther seaward.

The results of this study show that the location of the surface saturation boundary does not necessarily correspond to the location of the exit point. At Herring

Point, the exit point is located farther seaward than the surface saturation boundary. Infiltration occurs landward of the exit point beneath the swash edge, and groundwater discharge occurs seaward of the exit point to the tide level. These results further indicate that surface observations alone cannot be used to identify the location of the intersection of the water table with the beachface or to delineate zones of beachface infiltration and discharge.

The results show for the first time the dynamics of zones of infiltration, recharge, and discharge at the swash and tidal time scale. The infiltration zone and the maximum width of the subaerial discharge zone varied with the tide, though asymmetrically: the infiltration zone was more extensive during flood tide than ebb tide and the maximum width of the subaerial discharge zone was greater during ebb tide. On a swash event time scale, the surface saturation boundary moved across the beach independently of the location of infiltration and subaerial discharge. The zone of infiltration moved together with the swash edge and was the most dynamic region on the beachface. The findings demonstrate that the maximum width of the subaerial discharge zone was controlled primarily by the tide and the infiltration zone was controlled by swash.

Lysimeter measurements beneath the saturated beach and saturation profiles in the unsaturated beach provide, for the first time, insights into the spatial distribution of infiltration across the full swash zone at the time scale of individual swash events. Average infiltration per swash event is greater across the upper unsaturated beachface in comparison to the lower saturated beachface. However, total infiltration across the upper half of the swash zone is smaller due to infrequent swash inundation across that section of the beach.

Groundwater-surface water interactions in the swash zone at swash and tidal time scales are complex and need to be considered when identifying zones of infiltration and discharge on sandy beaches. The subsurface saturation dynamics and time scales of flow in the unsaturated zone have potentially important implications for the biogeochemistry of beach aquifers and for the modeling of sediment transport processes in the swash zone. Models that incorporate beachface saturation as a proxy for infiltration and groundwater discharge will need to be reexamined to more accurately characterize the distribution of vertical flow across the sand surface.

REFERENCES

Aagaard, T., and J. Holm (1989), Digitization of wave run-up using video records, *J. Coast. Res.*, 5(3), 547–551.

Anwar, N., C. Robinson, and D. A. Barry (2014), Influence of tides and waves on the fate of nutrients in a nearshore aquifer: Numerical simulations, *Adv. Water Resour.*, 73, 203–213, doi:10.1016/j.advwatres.2014.08.015.

Ataie-Ashtiani, B., R.E. Volker, and D.A. Lockington (2001), Tidal effects on groundwater dynamics in unconfined aquifers, *Hydrol. Processes,* 15(4), 655-669.

Austin, M. J., and G. Masselink (2006), Swash–groundwater interaction on a steep gravel beach, *Cont. Shelf Res*., 20, 2503-2519.

Bakhtyar, R., A. Brovelli, D.A. Barry, and L. Li (2011), Wave-induced water table fluctuations, sediment transport and beach profile change: Modeling and comparison with large-scale laboratory experiments. *Coastal Engineering*, 58(1), 103–118, doi:10.1016/j.coastaleng.2010.08.004.

Baldock, T. E., A. J. Baird, D. P. Horn, T. Mason, (2001), Measurements and modelling of swash-induced pressure gradients in the surface layers of a sand beach, *J. Geophys. Res.*, 106(C2), 2653–2666.

Befus, K. M., M. B. Cardenas, D. V. Erler, I. R. Santos, and B. D. Eyre (2013), Heat transport dynamics at a sandy intertidal zone. *Water Resour. Res*, 49(6), 3770–3786, doi:10.1002/wrcr.20325.

Bews, B. E, S. L. Barbour, G. W. Wilson, M. A. O'Kane (1997), The design of lysimeters for a low flux cover system over acid generating waste rock, *Proceedings of the 50th Canadian Geotechnical Conference of the Canadian Geotechnical Society*, Ottawa, Ontario, October 20-22, pp. 26-33.

Boufadel, M. C., H. Li, M. T. Suidan, and A. D. Venosa (2007), Tracer Studies in a Laboratory Beach Subjected to Waves, *J. Environ. Eng.*, 133, 722–732, doi:10.1061/(ASCE)0733-9372(2007)133:7(722).

Butt, T., P. Russell, I. Turner, (2001), The influence of swash infiltration–exfiltration on beach face sediment transport: onshore or offshore?, *Coastal Engineering*, 42, 35–52.

Cartwright, N., T. E. Baldock, P. Nielsen, D.-S. Jeng, and L. Tao (2006), Swash-aquifer interaction in the vicinity of the water table exit point on a sandy beach, *J. Geophys. Res.*, 111, C09035, doi:10.1029/2005JC003149.

Charbonnier, C., P. Anschutz, D. Poirier, S. Bujan, and P. Lecroart (2013), Aerobic respiration in a high-energy sandy beach, *Mar. Chem.*, 155, 10–21, doi:10.1016/j.

Charette, M. A., and E. R. Sholkovitz (2002), Oxidative precipitation of groundwater-derived ferrous iron in the subterranean estuary of a coastal bay, *Geophys. Res. Lett.*, 29(10), 1444, doi:10.1029/2001GL014512.

Charette, M. A., and E. R. Sholkovitz (2006), Trace element cycling in a subterranean estuary: Part 2. Geochemistry of the pore water, *Geochim. Cosmochim. Acta*, 70(4), 811–826, doi:10.1016/j.gca.2005.10.019.

Gast, R. J., S. Elgar, and B. Raubenheimer (2015), Observations of transport of bacterial-like microspheres through beach sand, *Cont. Shelf Res.*, *97*, 1–6, doi:10.1016/j.csr.2015.01.010.

Geng, X., and M.C. Boufadel (2015), Numerical study of solute transport in shallow beach aquifers subjected to waves and tides, *Journal of Geophysical Research: Oceans*, 120, 1409-1428, doi:10.1002/ 2014JC010539.

Hays, R. L., and W. J. Ullman, (2007), Direct determination of total and fresh groundwater discharge and nutrient loads from a sandy beachface at low tide (Cape Henlopen, Delaware), *Limnol. Oceanogr.*, 2(1), 240–247.

Hegge, B. J., and G. Masselink (1991), Groundwater-table responses to wave run-up: an experimental study from Western Australia, *J. Coastal Res.*, 7(3), 623-634.

Heiss, J. W., and H. A. Michael (2014), Saltwater-freshwater mixing dynamics in a sandy beach aquifer over tidal, spring-neap, and seasonal cycles, *Water Resour. Res.*, 50, 6747–6766, doi:10.1002/2014WR015574.

Heiss, J. W., W. J. Ullman, and H. A. Michael (2014), Swash zone moisture dynamics and unsaturated infiltration in two sandy beach aquifers, *Estuar. Coast. Shelf Sci.*, 143, 20–31, doi:10.1016/j.ecss.2014.03.015.

Holland, K. T., R. A. Holman, (1993), The statistical distribution of swash maxima on natural beaches, *J. Geophys. Res.*, 98, 10271–10278.

Holland, K. T., R. A. Holman, T. C. Lippmann, J. Stanley, and N. Plant (1997), Practical use of video imagery in nearshore oceanographic field studies, *J. Ocean. Eng.*, 22(1), 81–92.

Holman, R. A., A. H. Sallenger Jr., T. C. Lippmann, and J. W. Haines (1993), The application of video image processing to the study of nearshore processes, *Oceanography*, 6(3), 78–85.

Horn, D. P., T. E. Baldock, A. J. Baird, and T. E. Mason (1998), Field measurements of swash induced pressures within a sandy beach, *26th International Converence on Coastal Engineering*, pp. 2812–2825.

Horn, D. P. (2002), Beach groundwater dynamics, *Geomorphology*, 48(1-3), 121–146, doi:10.1016/S0169-555X(02)00178-2.

Hoque, Md., Asano, T. (2007), Numerical study on wave-induced filtration flow across the beach face and its effects on swash zone sediment transport, *Ocean Eng*. 34, 2033–2044.

Huisman, C. E., K. R. Bryan, G. Coco, and B. G. Ruessink (2011), The use of video imagery to analyse groundwater and shoreline dynamics on a dissipative beach, *Cont. Shelf Res.*, 31(16), 1728–1738, doi:10.1016/j.csr.2011.07.013.

Jemison, J. M., and R. H. Fox (1992), Estimation of zero-tension pan lysimeters collection efficiency, *Soil Sci*,. 15, 85–94.

Jordan, C. F. (1968), A simple, tension-free lysimeter, *Soil Sci.*, 105, 81-86.

Kang H-Y, P. Nielsen, D. J. Hanslow (1994), Watertable overheight due to wave runup on a sandy beach, *Proceedings of the 24th International Conference of Coastal Engineering*, Kobe, Japan; 1994. p. 2115– 2124.

Karambas, T. V. (2003), Modelling of infiltration-exfiltration effects of cross-shore sediment transport in the swash zone, *Coastal Eng.*, 45(1), 63–82, doi:10.1142/S057856340300066X.

Kroeger, K. D., and M. A. Charette (2008), Nitrogen biogeochemistry of submarine groundwater discharge, *Limnol. Oceanogr.*, 53(3), 1025–1039, doi:10.4319/lo.2008.53.3.1025.

Li, L., D. A. Barry, and C. B. Pattiaratchi (1997), Numerical modelling of tide-induced beach water table fluctuations, *Coast. Eng.*, 30(1-2), 105–123, doi:10.1016/S0378-3839(96)00038-5.

Li, L., D. A. Barry, F. Stagnitti, and J. Y. Parlange (1999), Submarine groundwater discharge and associated chemical input to the coastal sea, *Water Resour. Res.*, (35)11, 3253-3259.

Masselink, G., and L. Li, (2001), The role of swash infiltration in determining the beachface gradient: a numerical study, *Marine Geology*, *176*, 139–156.

Masselink, G., and I. L. Turner (2012), Large-scale laboratory investigation into the effect of varying back-barrier lagoon water levels on gravel beach morphology and swash zone sediment transport, *Coast. Eng.*, 63, 23–38, doi:10.1016/j.coastaleng.2011.12.007.

McAllister, S. M., J. M. Barnett, J. W. Heiss, A. J. Findlay, D. J. Macdonald, C. L. Dow, G. W. Luther, III, H. A. Michael, and C. S. Chan (2014), Dynamic hydrologic and biogeochemical processes drive microbially enhanced iron and sulfur cycling within the intertidal mixing zone of a beach aquifer, *Limnol. Oceanogr.*, 60, 329–345. doi: 10.1002/lno.10029.

McLachlan, A., I. G. Eliot, and D. J. Clarke (1985), Water filtration through reflective microtidal beaches and shallow sublittoral sands and its implications for an inshore ecosystem in Western Australia, *Estuar. Coast. Shelf Sci.*, 21, 91–104.

Michael, H. A., M. A. Charette, and C. F. Harvey (2011), Patterns and variability of groundwater flow and radium activity at the coast: A case study from Waquoit Bay, Massachusetts, *Mar. Chem.*, 127(1-4), 100–114, doi:10.1016/j.marchem.2011.08.001.

Moore, W. S. (1999), The subterranean estuary: A reaction zone of ground water and sea water, *Mar. Chem.*, 65, 111–125.

Nielsen, P. (1990), Tidal dynamics of the water table in beaches, *Water Resources Research*, *26*(9), 2127, doi:10.1029/WR026i009p02127.

Nielsen, P. (1992), Coastal bottom boundary layers and sediment transport, *Adv. Ser. Ocean Eng.*, vol. 4, World Scientific, Singapore.

Orr, M., M. Zimmer, D. E. Jelinski, and M. Mews (2005), Wrack deposition on different beach types: spatial and temporal variation in the pattern of subsidy, *Ecology*, 86(6), 1496–1507.

Packwood, A. R., Peregrine, D. H. (1980), The propagation of solitary waves and bores over a porous bed. *Coastal Eng.*, 3, 221–242.

Peters, A., and W. Durner (2009), Large zero-tension plate lysimeters for soil water and solute collection in undisturbed soils, *Hydrology and Earth System Sciences*, 6(3), 4637–4669, doi:10.5194/hessd-6-4637-2009.

Puleo, J. A. (2009), Tidal Variability of Swash-Zone Sediment Suspension and Transport, *J. Coast. Res.*, *254*, 937–948, doi:10.2112/08-1031.1.

Riedel, T., K. Lettmann, M. Beck, and H. -J. Brumsack (2010), Tidal variations in groundwater storage and associated discharge from an intertidal coastal aquifer. *Journal of Geophysical Research - Oceans*, 115(C4), 1–10. doi:10.1029/2009JC005544

Rosenberry, D. O., Sheibley, R. W., Cox, S. E., Simonds, F. W., and Naftz, D. L. (2013). Temporal variability of exchange between groundwater and surface water based on high-frequency direct measurements of seepage at the sediment-water interface, *Water Res. Resor*, 49(5), 2975–2986, doi:10.1002/wrcr.20198.

Roy, M., J. B. Martin, J. Cherrier, J. E. Cable, and C. G. Smith (2010), Influence of sea level rise on iron diagenesis in an east Florida subterranean estuary, *Geochim. Cosmochim. Acta*, 74(19), 5560–5573, doi:10.1016/j.gca.2010.07.007.

Russell, A. E., and J. J. Ewel (1985), Leaching from a tropical andept during big storms: A comparison of three methods, *Soil Sci*., 139, 181–189.

Santoro, A. (2010), Microbial nitrogen cycling at the saltwater-freshwater interface, *Hydrogeology Journal*, 18, 187-202, dio:10.1007/s10040-009-0526-z.

Santos, I. R., W. C. Burnett, J. Chanton, B. M. Mwashote, I. G. N. A. Suryaputra, and T. Dittmar (2008), Nutrient biogeochemistry in a Gulf of Mexico subterranean estuary and groundwater-derived fluxes to the coastal ocean, *Limnol. Oceanogr.*, 53(2), 705–718, doi:10.4319/lo.2008.53.2.0705.

Sawyer, A. H., O. Lazareva, K. D. Kroeger, K. Crespo, C. S. Chan, T. Stieglitz, and H. A. Michael (2014), Stratigraphic controls on fluid and solute fluxes across the sediment-water interface of an estuary, *Limnol. Oceanogr.*, 59(3), 997–1010, doi:10.4319/lo.2014.59.3.0997.

Sous, D., A. Lambert, V. Rey, and H. Michallet (2013), Swash–groundwater dynamics in a sandy beach laboratory experiment, *Coastal Engineering*, 80, 122–136, doi:10.1016/j.coastaleng.2013.05.006.

Steenhauer, K., D. Pokrajac, T. O'Donoghue, and G. A. Kikkert (2011), Subsurface processes generated by bore-driven swash on coarse-grained beaches, *J. Geophys. Res.*, 116, C04013, doi:10.1029/2010JC006789.

Steenhauer, K., D. Pokrajac, and T. O'Donoghue (2012), Numerical model of swash motion and air entrapment within coarse-grained beaches, *Coast. Eng.*, 64, 113–126, doi:10.1016/j.coastaleng.2012.01.004.

Spiteri C, C. P. Slomp, M. A. Charette, K. Tuncay, C. Meile (2008), Flow and nutrient dynamics in a subterranean estuary (Waquoit Bay, MA, USA): field data and reactive transport modeling, *Geochim. Cosmochim. Acta.*, 72, 3398–3412.

Thompson, M. L., and R. L. Scharf (1994), An improved zero-tension lysimeter to monitor colloid transport in soils, 24, 378–383.

Talbot, C. A., and F. L. Ogden (2008), A method for computing infiltration and redistribution in a discretized moisture content domain, *Water Resour. Res.*, 44, 1–14, doi:10.1029/2008WR006815.

Turner, I. L. (1993), Water table outcropping on macro-tidal beaches: a simulation model, *Marine Geology*, 115, 227–238.

Turner, I. L. and G. Masselink (1998), Swash infiltration-exfiltration and sediment transport, *J. Geophys. Res*., 103(C13), 30813–30824.

Turner, I. L., and P. Nielsen (1997), Rapid watertable fluctuations within the beachface: implications for swash zone sediment mobility?, *Coast. Eng.*, 32, 45–59.

Turner, I. L., and G. Masselink (2012), Coastal gravel barrier hydrology - Observations from a prototype-scale laboratory experiment (BARDEX), *Coast. Eng.*, 63, 13–22, doi:10.1016/j.coastaleng.2011.12.008

Ullman, W. J., B. Chang, D. C. Miller, and J. A. Madsen (2003), Groundwater mixing, nutrient diagenesis, and discharges across a sandy beachface, Cape Henlopen, Delaware (USA), *Estuar. Coast. Shelf Sci.*, 57, 539-52.

Urish, D., and T.E. McKenna (2004), Tidal effects on ground water discharge through a sandy marine beach, *Ground Water*, 42(7), 971-982.

Waddell, E. (1976), Swash-groundwater-beach profile interactions, In: Davis, R.A., Etherington, R.L. (Eds.), Beach and Nearshore Sedimentation, *Society of Economic and Paleontological Mineralogists Special Publication 24*, Tulsa, OK, pp. 115e125.

Vousdoukas, M. I. (2014), Observations of wave run-up and groundwater seepage line motions on a reflective-to-intermediate, meso-tidal beach, *Mar. Geol.*, 350, 52–70, doi:10.1016/j.margeo.2014.02.005.

Zhu, Y., R. H. Fox, and J. D. Toth (2002), Leachate collection efficiency of zero-tension pan and passive capillary fiberglass wick lysimeters, *Soil Sci. Soc. Am. J.*, 66, 37–43.

Chapter 4

PHYSICAL CONTROLS ON BIOGEOHEMICAL PROCESSES IN THE INTERTIDAL ZONE OF BEACH AQUIFERS

ABSTRACT

Marine ecosystems are sensitive to inputs of chemicals in submarine groundwater discharge. Tidally-influenced saltwater-freshwater mixing zones in beach aquifers can act as hot spots of biogeochemical transformations that modify chemical loads prior to discharge. A numerical variable-density groundwater flow and reactive transport model was used to evaluate the physical controls on reactivity for mixing-dependent and mixing-independent reactions in beach aquifers, represented as sulfate reduction and denitrification, respectively. A sensitivity analysis was performed across typical values of tidal amplitude, hydraulic conductivity, terrestrial freshwater flux, beach slope, and dispersivity. The results provide insights into the distribution of denitrification rates and cumulative nitrate and sulfate transformation in the beach aquifer. Simulations demonstrate that reactions within beach aquifers can significantly alter land-derived solute fluxes to coastal waters and that the magnitude of alteration is strongly linked to physical hydrogeology. Tidally-driven mixing between saltwater and freshwater promotes denitrification along the boundary of the intertidal saltwater circulation cell. Denitrification rates are highest on the landward side of the circulation cell where seawater infiltrates and decrease along circulating flow paths. The physical

setting strongly influences reactivity due to influence on fluxes of reactants and the nature of saltwater circulation and mixing. Reactivity for mixing-dependent reactions increases primarily with the size of the mixing zone, while mixing-independent reactivity increases with solute supply. The results provide insights into the types of beaches most efficient for altering fluxes of chemicals prior to discharge, which may be important for protection of coastal ecosystems and estimation of chemical fluxes to the ocean.

4.1 Introduction

Nutrient loading from submarine groundwater discharge (SGD) can affect the health of near-shore marine ecosystems [Valiela et al, 1990; LaRoche et al., 1997; Slomp and Van Cappellen, 2004; Amatoe et al., 2016], leading to eutrophication, anoxic conditions, loss of habitat, and changes in the type and rate of primary production [Valiela et al., 1997; Paerl et al., 1998; Pinckney et al., 2001; Bowen et al., 2007]. Fresh groundwater flowing from upland sources into coastal surface waters is often contaminated with N in the form of NO_3^- from agricultural practices and oxidation of septic wastewater leachate. Nutrient concentrations in groundwater are typically 2-3 orders of magnitude higher than in coastal surface waters [Slomp and Van Cappellen, 2004] and global SGD may rival surface runoff [Moore, 2008]. Thus, SGD can serve as a significant pathway for nutrient delivery to estuaries and the coastal ocean [Slomp and Van Cappellen, 2004; Burnett et al., 2007; Niencheski et al., 2007; Taniguchi et al., 2008; Russoniello et al., 2016]. However, the fate of nutrients prior to entering marine ecosystems is influenced by the temporal and spatial distribution of redox zones encountered along discharging flow paths [Charette and Sholkovitz., 2002; Slomp and Van Cappellen, 2004; Kroeger and Charette, 2008; Santos et al., 2008; Santoro, 2009; Spiteri et al., 2008; Roy et al., 2011; Charbonnier et al., 2013; McAllister et al., 2015; Reckhardt et al., 2015]. As the availability of reactive solutes needed to drive redox processes hinges upon the flow system, understanding how physical hydrogeologic characteristics influence the transport and transformation of nutrients in discharging groundwater is critical for effective management of nutrients for the protection of marine ecosystems.

Groundwater flow and solute transport in coastal aquifers leads to mixing between terrestrially-derived fresh and marine-derived saline groundwater (Figure

4.1). Fresh groundwater driven by the inland hydraulic gradient flows into the beach aquifer and mixes with seawater infiltrating across the beachface due to tide [Michael et al., 2005; Robinson et al., 2006, Befus et al., 2013, Abarca et al., 2013; Heiss and Michael, 2014] and wave [Xin et al., 2014; Robinson et al., Heiss et al., 2014; Geng and Boufadel, 2015] action. The resulting hydraulic gradient leads to a pattern of circulating brackish to saline groundwater in the intertidal zone, where water flows downward from the high tide mark and seaward to discharge along the base of the beachface (Figure 4.1). The seaward extent of the brackish circulation cell is often, though not always [Evans and Wilson., 2016], bounded by a zone of fresh groundwater that discharges near the low tide mark. Farther seaward, density gradients drive circulation of saltwater along the lower saltwater-freshwater interface.

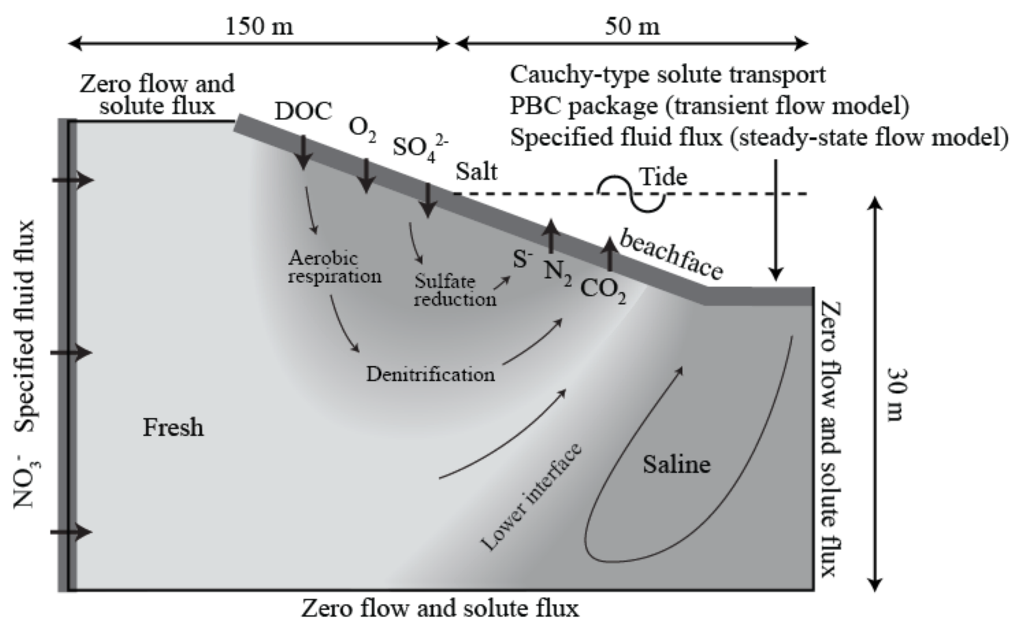

Figure 4.1 Conceptual and numerical model schematic showing reactants and products flowing into and out of the model domain, boundary conditions, and salinity distribution in a coastal aquifer.

The intertidal zone hosts geochemical gradients that form along flowpaths and as a result of mixing between the freshwater and saltwater endmembers. These gradients drive microbially mediated chemical transformations that modify solute concentrations in groundwater prior to discharge. Chemical transformations in coastal aquifers include dissolved organic carbon (DOC) degradation [Kroeger and Charette, 2008], aerobic respiration [Slomp and Van Cappellen, 2004], denitrification [Santos et al., 2009; Meile et al., 2010], nitrification [Ullman et al., 2003], anaerobic ammonium oxidation [Slomp and Van Cappellen, 2004], dissimilatory NO_3^- reduction to ammonium [Santoro, 2010], sulfate reduction [McAllister et al., 2015], and iron oxidation [Charette and Sholkovitz, 2002]. Iron oxidation leads to precipitation of iron oxides onto sediment surfaces. These iron coated sediments adsorb and sequester solutes including phosphate and arsenic along groundwater flow paths [Charette and Sholkovitz, 2002; Jung et al., 2009]. Transformation of nitrate (NO_3^-) to N_2 gas via denitrification is a particularly important process for reducing the bioavailable N load to coastal waters [Galloway et al., 2003]. Seawater infiltrating across the beachface due to wave and tidal action carries DOC and O_2 downward to the NO_3^--enriched freshwater beneath the intertidal zone [Anschutz et al., 2009; Santos et al., 2009; McAllister et al., 2015, Reckhardt et al., 2015]. Because O_2 is rapidly consumed as seawater circulates through the beach [Charbonnier et al., 2015], mixing between the DOC-rich seawater endmember and NO_3^--rich freshwater along deeper anaerobic flow paths will favor denitrification.

Sulfate (SO_4^{2-}) entering the beach with infiltrating seawater can serve as a terminal electron accepter once more efficient oxidizing agents are consumed. Reduction of SO_4^{2-} to sulfide (S^-) is important because S^- affects cycling of N and other elements. For example, denitrification can be fueled by oxidation of S^- rather than DOC [Rivett et al., 2008]. Further, S^- reacts with Fe^{2+} to generate iron sulfide (FeS), leading to precipitation and FeS coated sediments [McAllister et al., 2015]. FeS minerals sequester different elements than iron oxides [Fan et al., 2013], hence understanding sulfate reduction and S^- distributions is a first step to understanding adsorption, precipitation, dissolution, and cycling of other chemicals in intertidal aquifers.

Nutrient concentrations in nearshore aquifers are spatially variable and tied to the physical mixing between the freshwater and saltwater endmembers and the diagenetic recycling of DOC and POC [Ullman et al., 2003; Hays and Ullman, 2007; Kroeger and Charette, 2008; Spiteri et al, 2008; Gonneea and Charette, 2014; Reckhardt et al., 2015]. Seasonal variability in the supply of fresh and saltwater, and thus the supply of solutes to the reaction zone also affects the redox conditions of beach aquifers [Beck et al., 2008; Santos et al., 2008; Charbonnier et al., 2013; McAllister et al., 2015]. While the spatial and temporal patterns of biogeochemical reaction zones are becoming clearer, insight gained through field studies inherently considers the cumulative effects of multiple forcings acting on different time scales. Compounded by the complexity of flow and transport in heterogeneous systems, cumulative and potentially non-linear interactions mask the importance of the individual factors regulating nutrient cycling in these hydrologically and biogeochemically complex and dynamic coastal systems.

Numerical groundwater flow and reactive transport models can be used to investigate the individual physical controls on transport and chemical cycling in nearshore aquifers. Spiteri et al. [2008a; 2008b] demonstrated through modeling that

N and P cycling along the lower saltwater-freshwater interface is controlled by the groundwater flow field and extent of mixing between saltwater and freshwater. Model sensitivity showed that denitrification was unable to remove large quantities of NO_3^- in systems with high groundwater velocities and low rates of DOC oxidation, leading to nearly conservative transport. Conversely, low groundwater velocities and high DOC oxidation rates increased denitrification rates and significantly reduced NO_3^- fluxes across the aquifer-ocean interface [Spiteri et al., 2008a]. Meile et al. [2010] assessed the role of point-source septic systems as potential N sources by evaluating the importance of the freshwater gradient, DOC reactivity, and septic system setback distance on NO_3^- removal along the lower interface. Hydrologically more complex reactive transport models have demonstrated the importance of tides on regulating the fate of chemicals in coastal aquifers. Robinson et al. [2009] investigated the influence of tides on the degradation of BTEX compounds in discharging groundwater and showed that an increase in tidal amplitude, a decrease in freshwater flux, and a decrease in the rate of O_2 consumption all increase BTEX removal. Anwar et al. [2014] simulated the effects of tides and waves on nutrient cycling and fluxes across the beachface and showed that NO_3^- attenuation increased with oceanic forcing (tidal and wave amplitude) due to greater mixing between saltwater and freshwater. In natural systems, oceanic forcing interacts with other physical factors that control NO_3^- attenuation, including beach slope, freshwater influx, K, and dispersion. However, the effects of beach slope, freshwater influx, K, and dispersion on NO_3^- and SO_4^{2-} attenuation in tidally-influenced beach aquifers remains unclear. Additionally, changes to the distribution of denitrification rates, sulfate reduction rates, and reaction products beneath the intertidal zone in response to variation of these physical factors, including tidal amplitude, has not been investigated.

We assessed beach reactivity for mixing-dependent and mixing-independent reactions through simulation of sulfate reduction and denitrification, respectively. Reactivity was assessed based on the amount of terrestrially-derived NO_3^- and seawater-derived SO_4^{2-} removed prior to discharge. The size and location of the reaction zone and the distribution of dissolved species were also considered in our assessment. A sensitivity analysis of five physical factors including tidal amplitude, freshwater flux, hydraulic conductivity, beach slope, and dispersivity, was performed over a range of typical values to identify the physical conditions that enhance beach reactivity. The results provide insight into the NO_3^- and SO_4^{2-} attenuation capacity of a wide spectrum of sandy beaches and reveal how the physical mechanisms controlling flow and transport alter the fate and fluxes of groundwater-borne nutrients to nearshore marine ecosystems.

4.2 Numerical Simulations

Groundwater flow, salt transport, and reactive solute transport in a beach aquifer was simulated using SEAWAT v4.0 [Langevin et al., 2004] and PHT3D v2.13 [Prommer and Post, 2002]. SEAWAT v4.0 solves the coupled flow and solute transport equations using a cell-centered finite difference approximation to simulate density-dependent groundwater flow and transport. PHT3D v.2.13 is a multi-species three-dimensional reactive transport model that incorporates SEAWAT v4.0 with the aqueous geochemical model PHREEQC-2 v2.17 [Parkhurst and Appelo, 1999].

The model represented a cross-section of a homogeneous, sandy, unconfined coastal aquifer with terrestrial freshwater inflow and saltwater inflow via tidal forcing.

The model domain extended 50 meters seaward and 150 m landward of the beachface-mean sea level (MSL) intersection and 30 m below MSL (Figure 4.1). A constant sloping beachface (0.069) was set along the aquifer-ocean interface. Following Robinson et al. [2007], a nonuniform grid with 125 layers and 184 columns was used, with higher discretization (dx = 0.31 m, dy = 0.06 m) in the intertidal zone where high groundwater flow rates, strong concentration gradients, and redox processes were present.

4.2.1 Groundwater Flow and Salt Transport Model

The boundary conditions for the flow and salt transport model were set to represent natural forcing conditions acting on a beach aquifer. Tidal forcing along the aquifer-ocean interface was simulated using the Periodic Boundary Condition (PBC) package [Post, 2011]. A sinusoidal time-varying Dirichlet boundary condition was assigned to the aquifer-ocean interface nodes. The time-varying head was calculated as:

$$h_t = h_o + A\cos(\omega t - \theta) \tag{4.1}$$

where h_t (m rel. MSL) is the tidal elevation at time t, h_o (m) is a reference water level (MSL), A (m) is the tidal amplitude, ω ($= \frac{2\pi}{T}$) is the frequency in rad s^{-1}, and θ (rad) is the phase shift.

A Neumann boundary condition was set along the landward vertical boundary to represent freshwater inflow of terrestrial origin, with a constant concentration of 0 ppt. The top, bottom, and right vertical boundaries were set as zero flow and zero solute flux. A constant concentration of 35 ppt was assigned along the aquifer-ocean interface for inward flow and a zero-concentration gradient was set for outward flow.

4.2.2 Reactive Transport Model

Microbially-mediated biogeochemical processes occurring within beach aquifers were investigated using a reaction network of 7 reactive species. The model considers DOC degradation, aerobic respiration, denitrification, and sulfate reduction, reflecting the redox kinetics of DOC, O_2, NO_3^-, N_2, CO_2, SO_4^{2-}, and S^- (Tables 4.1 and 4.2). Denitrification was modeled as a 1st order reaction and sulfate reduction was modeled as a 0th order reaction.

The purpose of modeling a 1st and 0th order reaction was to explore the influence of physical factors on reaction types, focusing on denitrification and sulfate reduction as examples of a reaction that requires mixing and one that does not. We omit the production of NH_4^+ from DOC mineralization and subsequent nitrification as we are interested in quantifying NO_3^- transformation of land-derived sources only, and we discuss the implications of this omission in Section 4.4.3. Nevertheless, terrestrial NO_3^- sources provide a net flux of bioavailable N to coastal surface waters, whereas NO_3^- produced through DOC degradation to NH_4^+ and subsequent nitrification represents a recycled N load. The reaction network and rate expressions for DOC degradation, aerobic respiration and denitrification were adopted from Bardini et al. [2014] and are based on the redox kinetics in Hunter et al. [1998]. The reactions are shown in Table 1 and the corresponding reaction parameter values are provided in Table 2. DOC oxidation is assumed to be a linear 1st-order reaction with respect to the DOC concentration, with O_2 and NO_3^- as the terminal electron acceptors. The reduction of O_2 and NO_3^- proceeds from the most (O_2) to least (NO_3^-) thermodynamically favorable terminal electron acceptor and follows a modified Monod kinetic formulation where the reduction rate is limited by the availability of the electron acceptor. When the O_2 concentration is greater than the limiting value, the reduction rate is constant, whereas below the O_2 limiting concentration, the reduction rate is linearly proportional to concentration.

Sulfate reduction is modeled as a 0^{th}-order reaction with respect to SO_4^{2-} to yield S^- [Appelo and Postma, 2005]. This simplified approach assumes the sulfate reduction rate is independent of the DOC concentration, hence N and S cycling was modeled separately. Representation of sulfate reduction in this way allows us to explore another type of reaction that does not require mixing to drive reactivity.

Similar to conservative salt transport, a zero concentration gradient was set along the discharging portion of the aquifer-ocean interface and a constant concentration was set for the inflowing portion. Source concentrations along the aquifer-ocean interface and landward boundary were assigned according to literature values [Appelo and Postma, 2005; Bardini et al., 2012] that are characteristic of coastal sediment [Berner, 1986; van Cappellen and Wang, 1996]. Seawater entering the model domain across the aquifer-ocean interface served as a source of DOC (2×10^{-3} M), O_2 (3.13×10^{-4} M), and SO_4^{2-} (0.2 M). Fresh groundwater inflow from the landward boundary contained NO_3^- (1.29×10^{-4} M).

Simulations were performed in three steps. First, variable-density flow and salt transport under the influence of tides was simulated for 500 d to ensure that dynamic steady state had been reached with respect to hydraulic heads and salt concentrations. Tidally-averaged fluid fluxes and salt concentrations across the aquifer-ocean interface were then used to simulate steady-state groundwater flow and transport dynamics. Finally, the reactive solutes were superimposed on the phase-averaged flow field from step two and PHT3D was run for 500 d to allow the reactive solutes to reach equilibrium. Reactive transport was modeled using the phase-averaged flow field to improve numerical convergence.

Table 4.1 Reaction network and kinetic rate expressions. DOC degradation, aerobic respiration, and denitrification adopted from Bardini et al., 2012, and sulfate reduction adopted from Appelo and Postma [2005].

Name	Reaction	Rate expression
DOC degradation	DOC → no product	Rate = k_{fox}[DOC];
Aerobic respiration	$DOC + O_2 \rightarrow CO_2 + H_2O$	If $[O_2]$ > kmo2; Rate = k_{fox}[DOC]; If $[O_2]$ < kmo2; Rate = k_{fox}[DOC] ($[O_2]$/kmo2)
Denitrification	$5DOC + 4NO_3^- + 4H^+ \rightarrow 5CO_2 + 2N_2 + 7H_2O$	If $[O_2]$ > kmo2; Rate = 0; If $[O_2]$ < kmo2 and $[NO_3^-]$ > kmno3; Rate = k_{fox}[DOC] (1 –$[O_2]$/kmo2); If $[O_2]$ < kmo2 and NO_3^- < kmo3; Rate = k_{fox}[DOC] (1 – $[O_2]$/kmo2) ($[NO_3^-]$/kno3)
Sulfate reduction	$SO_2^- \rightarrow S^-$	Rate = k_{sox}

Table 4.2. Reaction parameter values.

Parameter	Units	Description	Value
k_{fox}	s^{-1}	Rate constant for decomposition of DOC	1.5×10^{-6} [a]
k_{sox}	s^{-1}	Rate constant for sulfate reduction	1.07×10^{-8} [bc]
kmo2	M	Limiting concentration of O_2	3.125×10^{-5} [ad]
kmno3	M	Limiting concentration of NO_3^-	8.065×10^{-6} [ad]

[a]van Cappellen and Wang [1996]
[b]Appelo and Postma [2005]
[c]Berner [1981]
[d]Bardini et al. [2012]

4.2.3 Sensitivity Analysis

A total of 330 flow and reactive transport simulations were performed around a base case parameter set to assess the effects of tidal amplitude, freshwater flux (Q_f), hydraulic conductivity (K), beach slope, dispersivity, and DOC degradation rate on nutrient distributions and fluxes across the sediment-water interface.

The relative effectiveness of mass transport by advection and hydrodynamic dispersion in the intertidal circulation cell can be quantified using the Péclet number, $Pe = L/\alpha_L$, where L is the length of the beachface and α_L is the longitudinal dispersivity [L]. The Péclet number was varied from 0.8-3.2 by adjusting longitudinal dispersivity. It is generally accepted that transport by advection dominates when $Pe > 2$ and dispersion dominates for $Pe < 2$.

The dimensionless Damköhler number (Da) relates the chemical reaction time scale to the transport time scale within and across systems [Zarnetske et al., 2012] and has been used to relate denitrification rates to advective transport rates [Briggs et al., 2015; Gu et al., 2007; Ocampo et al., 2006]. The Da number is defined as

$$\mathrm{Da} = \mathrm{k_{fox}} * \mathrm{V_s}/\mathrm{Q_i} \tag{4.2}$$

where $\mathrm{k_{fox}}$ is the rate constant for DOC degradation [T^{-1}] and $\mathrm{V_s}/\mathrm{Q_i}$ is the saltwater residence time [T] in the intertidal circulation cell, where V_s [L^3] is the volume of the saltwater in the intertidal circulation cell, and Q_i [L^3/T] is the tidally-averaged influx across the sediment-water interface per unit length of shoreline. A Da of 1 implies that the supply of reactive solutes is balanced by reactive demand. As Da increases over 1 through either a decrease in the advective transport rate or an increase in the reaction rate, solute supply is unable to match reactive demand and the system becomes advection limited. As advective transport increases or the reaction rate decreases, Da decreases and supply outpaces demand resulting in a system that is rate limited. Thus, Da greater than 1 correspond to advection-limited systems while Da less than 1 indicate rate-limited systems.

The Da number for a set of parameters is unknown *a priori* because residence time is calculated within the simulations. Trial and error was used to establish a base case model where Da was approximately 1 and Pe = 2. Parametric sensitivity was conducted around the base case over which tidal amplitude (0.25 – 1.35 m), hydraulic conductivity (2-50 m/d), freshwater flux (0.4-4 m^3/d), beach slope (0.0375-0.1), and dispersivity (1-7.5 m) were varied. In the base case scenario, the tidal amplitude = 0.75 m, K = 25 m/d, freshwater flux = 2 m^3/d, beach slope = 0.068, and longitudinal dispersivity = 3.0 with a transverse dispersivity ratio of 0.1 constant across all models.

Reactivity was assessed based on the quantity of NO_3^- removed in the intertidal zone and the amount of NO_3^- removed as a percent of terrestrial influx. Removal was calculated as the difference between the total flux into the model domain across the landward boundary and the total flux across the aquifer-ocean interface, in moles per day.

4.3 Results

4.3.1 Solute and Reactivity Distributions – Base Case

Tidal forcing across the aquifer-ocean interface in the base case scenario formed a saltwater circulation cell in the intertidal zone where saltwater infiltrated near the high tide mark, flowed downward and seaward, and then discharged near the low tide mark, consistent with previous field and numerical modeling studies [Figure

4.2a; Lebbe, 1999; Boufadel, 2000; Michael et al., 2005; Robinson et al., 2006; Abarca et al., 2013; Heiss and Michael, 2014]. Infiltrating seawater served as a source of labile DOC and O_2 to the intertidal zone leading to elevated DOC and O_2 concentrations immediately below the upper beachface (Figure 4.2b-c). Aerobic respiration rates were highest immediately below the sand surface between the MSL-beachface intersection and the high tide mark because DOC and O_2 inputs were highest across that section of the beach (Figure 4.3a). The aerobic respiration rate decreased with depth as O_2 was consumed. Once O_2 was completely consumed, the remaining DOC continued along flow paths and entered the mixing zone along the boundary of the circulation cell where it encountered NO_3^-. This lead to anoxic conditions at depth and set up favorable conditions for denitrification.

The reactants involved in denitrification, NO_3^- and DOC, originated in different waters; thus the reaction was mixing-dependent. The transition from aerobic respiration to denitrification occurred along the 10 ppt contour (Figure 4.3a). The denitrification rate was highest beneath the high tide mark and decreased along circulating flow paths to the low tide mark, forming an arc-shaped denitrification zone on the boundary of the circulation cell between 1 and 10 ppt, while aerobic respiration took place between 10 and 35 ppt. (Figure 4.3a). Thus, the aerobic respiration and denitrification zones were located on the inner and outer cell, respectively. Denitrification resulted in lower NO_3^- concentrations around the margins of the circulation cell than would occur due to conservative mixing (Figure 4.2a and e). N_2 was highest along the landward boundary of the saltwater circulation cell where denitrification rates were highest and decreased along circulating flow paths on the perimeter of the circulation cell (Figure 4.2f).

As SO_4^{2-} is the only reactant in this formulation of sulfate reduction, the reaction is not dependent on mixing with fresh water. SO_4^{2-} and S^- distributions reflect the reduction of SO_4^{2-} to S^- along circulating intertidal flowpaths (Figure 4.2g-h). SO_4^{2-} entered the aquifer across the beachface due to tidal forcing and immediately began to transform to S^-, which accumulated along circulating flow paths on the inside of the circulation cell (Figure 4.2g-h). Following 0^{th}-order kinetics, the sulfate reduction rate was uniform throughout the sulfate reduction zone and equal to 0.92 M/d as set by the rate constant for sulfate reduction (Figure 4.3b). In the base case scenario and in the sensitivity tests, sulfate reduction was confined to the inside of the circulation cell in groundwater with salinity greater than 10 ppt. The accumulation of S^- was highest along the 20 ppt salinity contour leading from the upper beachface to the low tide mark where the concentration of discharging S^- was highest. In contrast, N_2 accumulated along the 10 ppt salinity contour and discharged in a narrow zone 3 m seaward of the low tide mark. S^- was discharged farther landward because it was produced along shorter more saline circulating flow paths while N_2 was produced in the deeper mixing zone and was thus transported farther seaward.

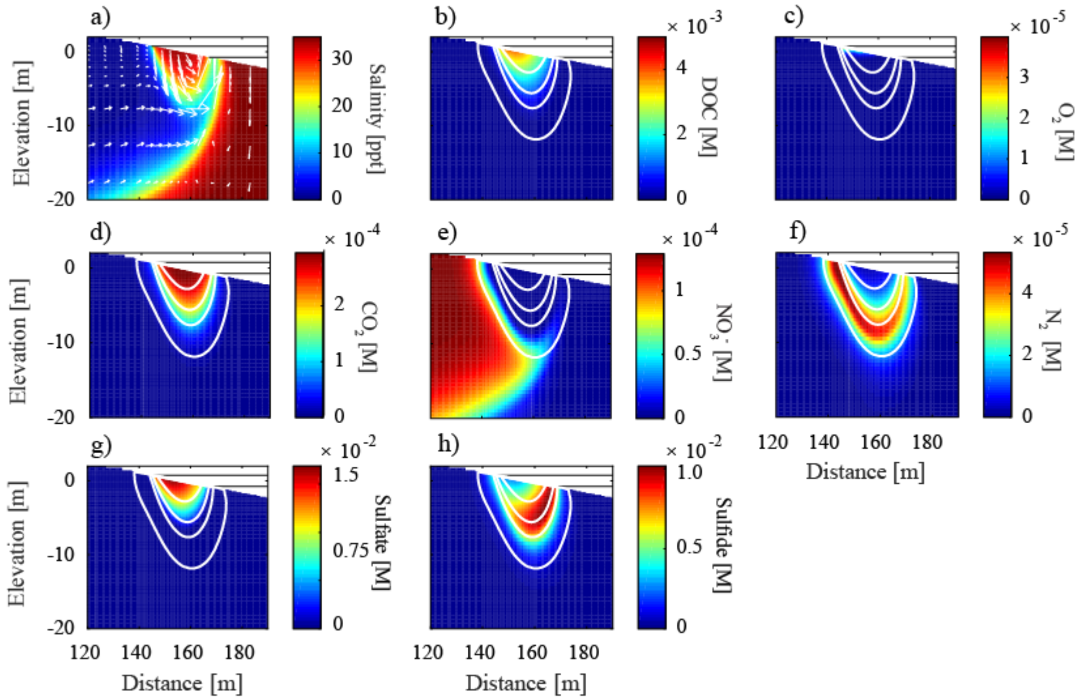

Figure 4.2 Solute distributions for the base case scenario. a) salinity and flow vectors, b) DOC, c) O_2, d), CO_2, e) NO_3^-, f) N_2, g) SO_4^{2-}, and h) S^-. The 1, 10, 20, and 30 ppt salinity contours for the circulation cell are shown in b-g.

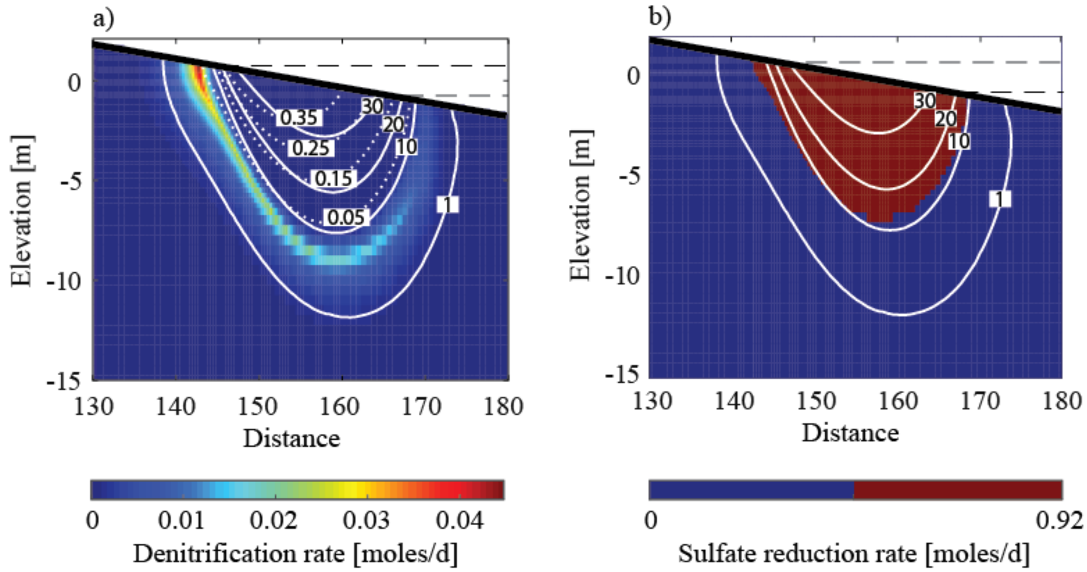

Figure 4.3 Reaction rates and zones for mixing-dependent and mixing-independent reactions. a) Denitrification rate (colorbar), aerobic respiration rate (moles/d; dotted contours), and intertidal salinity (solid contours), b) sulfate reduction zone and intertidal salinity (solid contours). Both panels show the base case. The horizontal dotted lines are the high and low tide elevations.

4.3.2 Sensitivity Analysis

4.3.2.1 Solute and Reactivity Distributions

Each of the 4 physical factors modified the location and rates of denitrification and sulfate reduction, and NO_3^-, N_2, SO_4^{2-}, and S^- concentrations in the intertidal zone. Hereafter, the part of the intertidal aquifer where NO_3^- was transformed to N_2 is defined as the denitrification zone, and the part of the beach where SO_4^{2-} was transformed to S^- is defined as the sulfate reduction zone.

The size of the reaction zones were most sensitive to tidal amplitude (Figure 4.4, row 1). As size of the mixing zone increased with tidal amplitude, the denitrification zone expanded and extended from the high tide mark, downward to the base of the circulation cell, and upward to the low tide mark. For tidal amplitudes below 0.55 m, the denitrification zone occupied the entire intertidal circulation cell. The sulfate reduction zone expanded with the circulation cell as SO_4^{2-} flux increased with tidal amplitude. The seaward extent of the sulfate reduction zone shifted landward from the fresh discharge zone as total transformation approached 100% for the case with a tidal amplitude of 1.35 m (Figure 4.4, column 5).

Similar overlap between the denitrification zone and circulation cell is evident for variations in freshwater flux, however for low freshwater fluxes the denitrification zone was located on the landward side of the mixing zone and did not extend to the discharge zone (Figure 4.4, row 2). This was due to the low freshwater flux across the left vertical boundary. Because the NO_3^- concentration along the left vertical boundary was constant across models, low freshwater fluxes resulted in lower NO_3^- fluxes. Therefore, all NO_3^- was consumed in a narrow band of denitrifying groundwater beneath the upper beachface. The thickness of the band increased with freshwater flux due more dispersion and intensified mixing. Complete NO_3^- removal is evident by the absence of an NO_3^- discharge zone for cases with 0.5 m^3/d and 1 m^3/d freshwater flux (Figure 4.5, row 4). The distribution of denitrification rates demonstrates that much of the removal for this case and other parameter sets with high amounts of removal occurred on the up-gradient side of the circulation cell (Figure 4.5, row 5). More seawater and SO_4^{2-} entered the aquifer at low freshwater fluxes to support large sulfate reduction zones (Figure 4.4, row 2). Thus, the distribution of the sulfate reduction zone was controlled strictly by the flux of SO_4^{2-} across the beachface while the distribution of the denitrification zone was controlled by mixing and the supply of NO_3^- in freshwater.

The size of the denitrification and sulfate reduction zones increased with increasing K, but for different reasons. Higher K values resulted in larger mixing and wider denitrification zones due to increased hydrodynamic dispersion as a result of higher flow velocities (Figure 4.4, row 3). In contrast, the size of the sulfate reduction zone increased with K as more seawater and SO_4^{2-} infiltrated across the more permeable beachface. Thus, K controlled the size of the denitrification zone through its effect on dispersion, and moderated the size of the sulfate reduction zone by influencing the infiltration rate.

Beach slope also affected the size and shape of the denitrification and sulfate reduction zones. The depths to the bottom of the circulation cell, denitrification zone, and sulfate reduction zone were constant across models while their horizontal extents almost doubled as the beach slope decreased (Figure 4.4, row 4). The thickness of the denitrification zone increased with beach slope because steeper beaches supported stronger hydraulic gradients that enhanced dispersion and mixing. The effect of higher flow rates on mixing for steeper beaches did not impact the size or shape of the sulfate reduction zone. As the slope of the beach decreased, a larger tidal excursion led to a wider infiltration zone which allowed the sulfate reduction zone to expand horizontally.

N_2 concentrations were generally correlated with the distribution of denitrification rates. The highest N_2 concentrations were located on the landward side of the circulation cell where denitrification rates were highest and decreased along circulating flow paths due to dispersion. This is particularly evident for large tidal amplitudes, low freshwater fluxes, and high K values where longer flow paths and higher flow rates led to greater hydrodynamic dispersion and lower concentrations of discharging N_2 (Figure 4.5). In contrast, S^- was highest on the seaward side of the circulation cell for all model runs (Figure 4.6). N_2 produced in the narrow mixing zone allowed it to disperse perpendicular to circulating flow paths, so concentrations decreased to the discharge zone. S^- was unable to disperse because it was produced inside the circulation cell and instead accumulated to the point of discharge. The accumulation is most noticeable for large tidal amplitudes, low freshwater fluxes, high K values, and gentle sloping beachfaces (Figure 4.6).

In summary, the size and structure of the denitrification zone depended on the intensity of mixing and the relative supply of NO_3^- and DOC, while the part of the beach undergoing sulfate reduction was tied to the supply of SO_4^{2-} only.

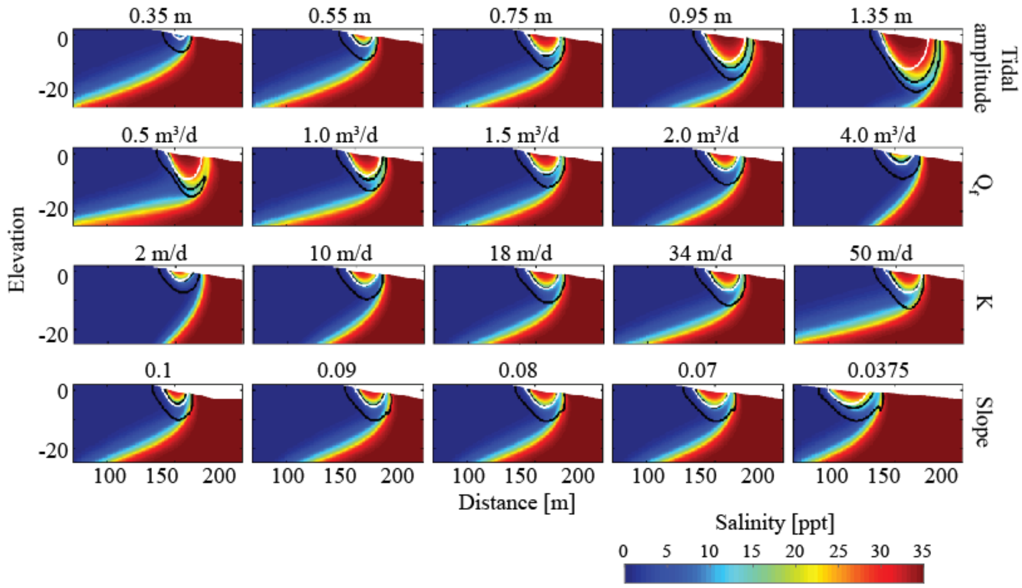

Figure 4.4 Denitrification (black contour) and sulfate reduction (white contour) zones with varying tidal amplitude, freshwater flux, hydraulic conductivity, and beach slope.

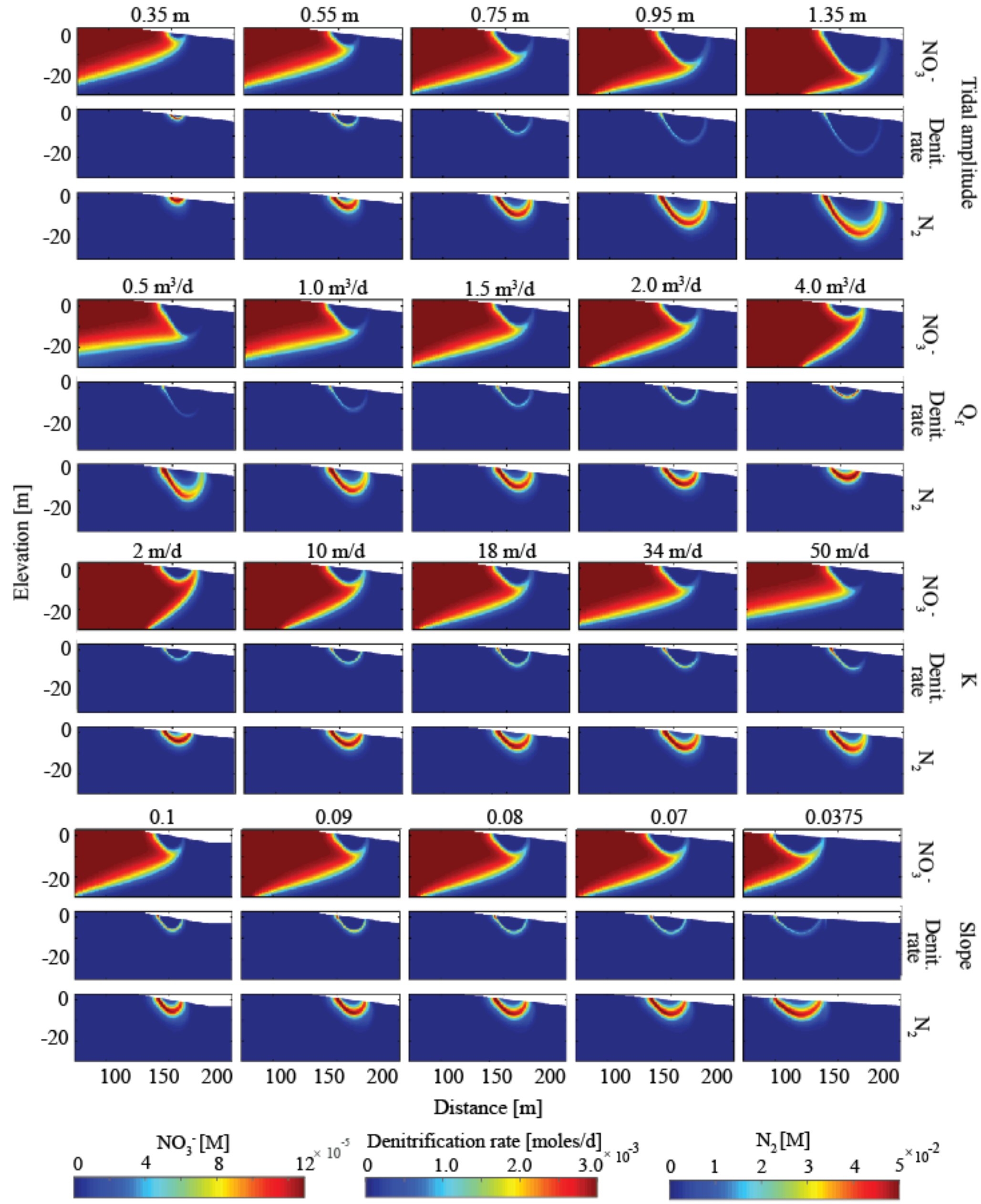

Figure 4.5 Denitrification rates and N_2 concentrations for sensitivity to tidal amplitude, freshwater flux, hydraulic conductivity, and beach slope.

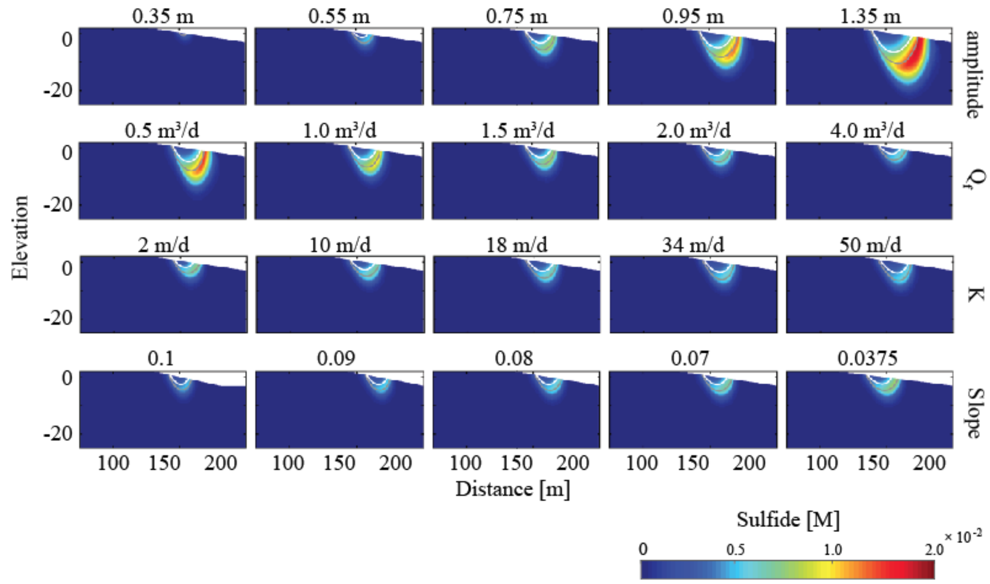

Figure 4.6 SO_4^{2-} (contours are 10% (gray) and 50% (white) maximum SO_4^{2-} concentration) and S^- (colorbar) concentrations for sensitivity to tidal amplitude, freshwater flux, hydraulic conductivity, and beach slope.

4.3.2.2 Nitrate and Sulfate Attenuation

The five physical parameters were varied to determine their importance on affecting the attenuation of land-derived NO_3^- and seawater derived SO_4^{2-} in the intertidal zone.

Tidal amplitude significantly altered the total and percent of NO_3^- removed prior to discharge. NO_3^- removal increased from 0-100% with increasing tidal amplitude up to 0.75 m as stronger tidal forcing created larger mixing zones (Figure 4.7a). For tidal amplitudes larger than 0.75 m (Da = 1), NO_3^- removal declined as the system became advection limited. The decline in reactivity was due to the reduction in the supply of DOC to the denitrification zone. As the size of the circulation cell grew, a larger proportion of DOC degraded along longer flow paths and less DOC reached the deeper sections of increasingly larger circulation cells. Thus, although the mixing zone was larger and more DOC infiltrated across the beachface for larger tidal amplitudes, the supply of DOC to the mixing zone became limited and total denitrification declined (Figure 4.7a), indicating that larger circulation cells do not always correlate with increased NO_3^- removal. A moderately sized tidal amplitude and mixing zone is optimal for NO_3^- removal due to the balance between the transport of DOC to the mixing zone and the size of the area with conditions suitable for denitrification.

The Da = 1 threshold also signified a reversal in the percent of SO_4^{2-} transformed over the range of tidal amplitudes. As the tidal amplitude increased to 0.75 m, the percent of SO_4^{2-} transformed decreased (Figure 4.8a). Above an amplitude of 0.75 m (Da = 1), the system became advection limited due to long residence times, which allowed for more transformation relative to the supply of SO_4^{2-}. On a per moles basis, total transformation increased with tidal amplitude as more SO_4^{2-} was introduced into the aquifer.

Hydraulic conductivity was the second most important physical factor controlling NO_3^- removal (Figure 4.7b). NO_3^- removal increased from 40% to 100% as K increased due to more dispersion resulting from higher flow velocities. Thus, despite high K values leading to shorter residence times that reduce reactivity, the effects of increased mixing dominated.

The total amount of SO_4^{2-} transformed displayed a similar trend to total denitrification as K increased (Figure 4.8b). At low K values (Da>1), the total amount of SO_4^{2-} transformed was limited because infiltration of SO_4^{2-} was restricted by the less permeable beachface. This indicates that, despite low K values resulting in long residence times that promote reactivity, a reduction in SO_4^{2-} supply was more important for SO_4^{2-} transformation.

The slope of the beach also affected NO_3^- attenuation with removal between 68-100% across beach slopes (Figure 4.7c). In contrast to the effects of tidal amplitude and K on forming larger mixing zones, which increased reactivity, it was the quantity of DOC infiltrating across the beachface that regulated denitrification over the range of beach slopes. Steep beaches supported stronger hydraulic gradients that drove more DOC into the subsurface, which increased reactivity (Figure 4.7c).

Sulfate reduction responded opposite to denitrification over the values for beach slope (Figure 4.8c). The total and percent of SO_4^{2-} transformed decreased as beach slope increased. In this case, the short residence times in steep beaches allowed SO_4^{2-} to circulate through the intertidal zone more conservatively.

High freshwater fluxes weakened tidally-driven flows and resulted in small mixing zones. This led to a decrease in the percent of NO_3^- removed from 51-100% (Figure 4.7d, Pe=2). NO_3^- was completely removed for low freshwater fluxes in large mixing zones. However, low freshwater fluxes did not result in the largest quantity of NO_3^- removed (Figure 4.7d). The quantity of NO_3^- removed was lowest for low freshwater fluxes because there was less available NO_3^- for consumption, while high freshwater fluxes supplied more NO_3^- to the mixing zone.

Variations in freshwater flux also modified sulfate reduction rates. High freshwater fluxes reduced the quantity of seawater and SO_4^{2-} infiltrating across the beachface which restricted the total amount of SO_4^{2-}transformed (Figure 7.8d). Freshwater flux had minimal effect on a percentage basis because additional transformation at low freshwater fluxes cells was balanced by supplemental input across the beachface.

Longitudinal and transverse dispersivity controls the intensity of mixing between freshwater and saltwater along the boundary of the circulation cell. Large mixing zones formed for high longitudinal and transverse dispersivity values (low Pe) and led to higher denitrification rates as expected (Figure 4.7). Dispersion had a negligible impact on sulfate reduction rates (not shown).

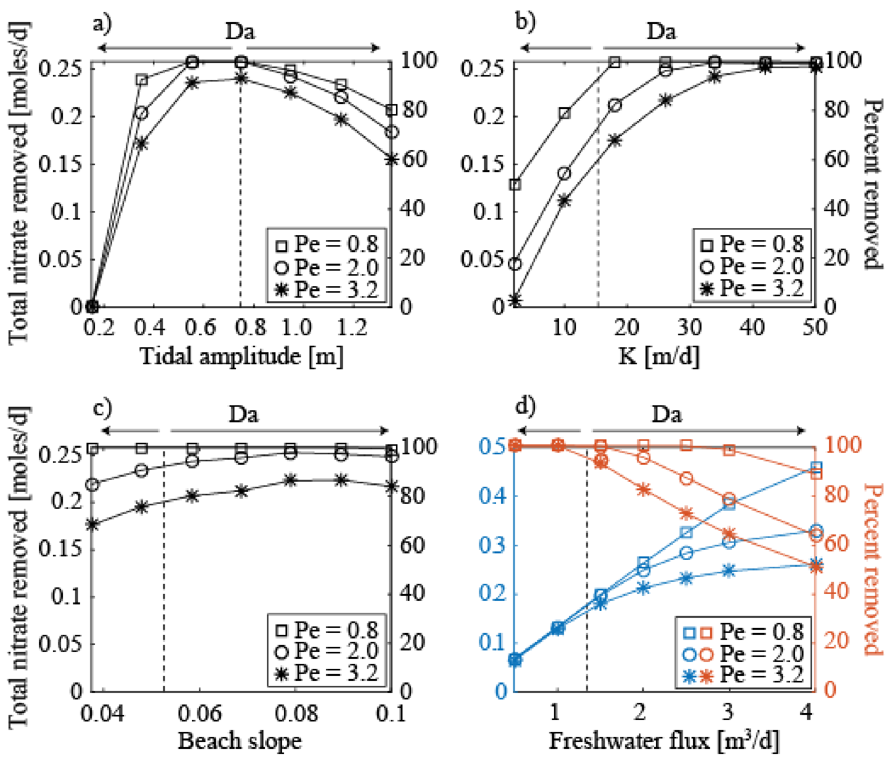

Figure 4.7 Sensitivity of total and percent NO3- removed to a) tidal amplitude, b) K, c) freshwater flux, and e) beach slope. Removal for 3 Pe values (solid lines) are shown for each physical parameter. The arrows along the top x-axes indicates where the Da number is increasing (to the right) or decreasing (to the left) relative to Da = 1 (vertical dotted line).

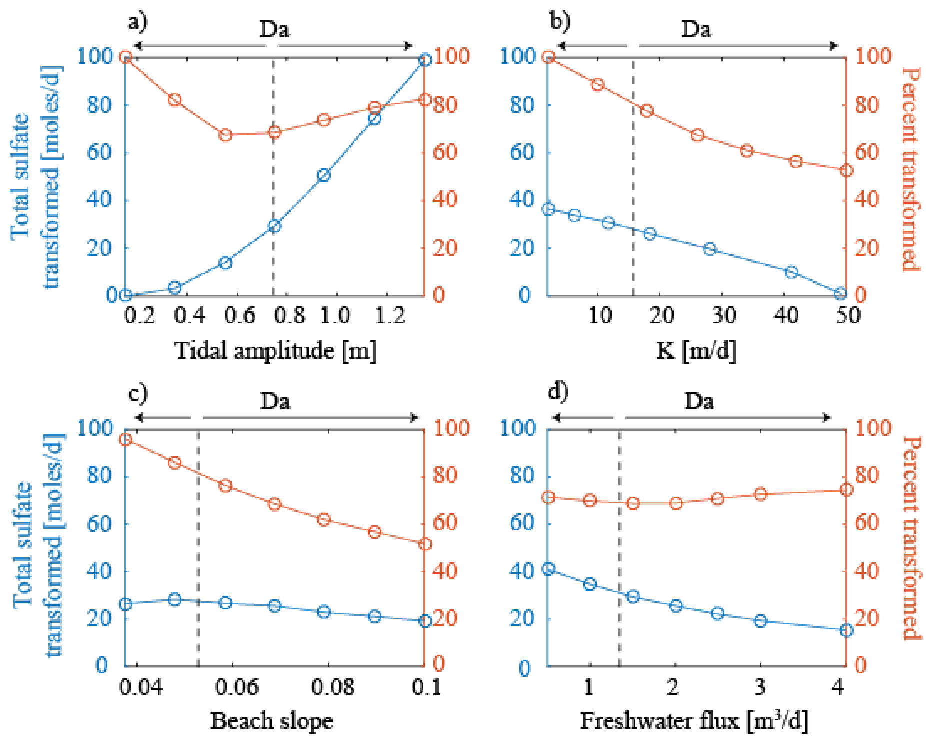

Figure 4.8 Sensitivity of total and percent sulfate transformed to a) tidal amplitude, b) K, c) freshwater flux, and e) beach slope. Results are shown for models with Pe = 2 for comparison to Figure 4.7. The arrows along the top x-axes indicates where the Da number is increasing (to the right) or decreasing (to the left) relative to Da = 1 (vertical dotted line).

4.3.2.3 Effects of DOC Reactivity

To assess the importance of DOC reactivity on NO_3^- attenuation, the DOC rate constant was varied between 1.5×10^{-5} s^{-1} and 1.5×10^{-7} s^{-1} across the range of parameter values for each physical factor (Figure 4.9). With the exception of the lowest rate constant, NO_3^- removal increased as DOC reactivity decreased for the tested values of tidal amplitude, K, freshwater flux, and beach slope (Figure 4.9a-4.9d).

At low DOC rate constants, less DOC degraded along circulating flow paths and hence more labile DOC was transported to the mixing zone. At high DOC rate constants, rapid DOC degradation limited the supply of DOC to the mixing zone to drive denitrification. However, the lowest DOC rate constant, $1.5x10^{-7}$ s^{-1}, did not correspond to the largest amount of NO_3^- removed for all 4 physical factors (Figure 4.9). In this case the effect of a marginal increase in the supply of DOC to the mixing zone was less important than the low DOC rate constant in controlling bulk NO_3^- transformation. The results demonstrate the importance of DOC reactivity on NO_3^- cycling in the intertidal zone and illustrate the interplay between the reaction rate and the physical flow system on affecting nutrient transport and fate in beach aquifers.

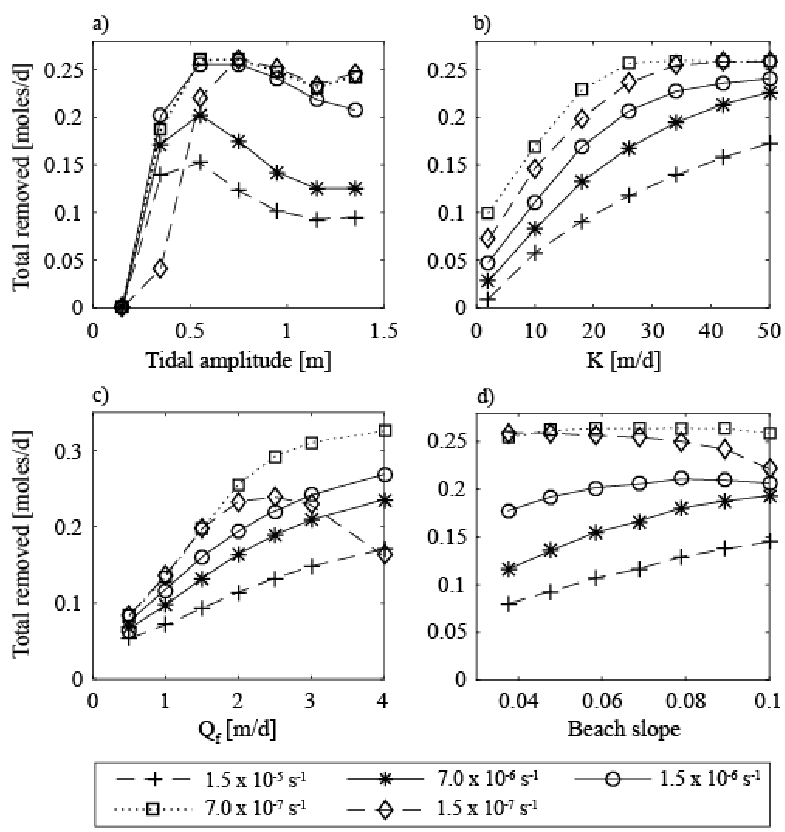

Figure 4.9. Total NO_3^- removed as a function of a) tidal amplitude, b) K, c) Q_f, and d) beach slope for a range of DOC rate constants.

4.4 Discussion

4.4.1.1 Physical and Biogeochemical Relationships

Several relationships were drawn between the physical and chemical characteristics of the beach aquifer. The size of the mixing zone increased with the size of the circulation cell, representing an average of 79% of its area (Figure 4.10a). The denitrification zone also increased with the size of the mixing zone and occupied an average of 49% of the mixing zone (Figure 4.10b), indicating that salinity alone is insufficient for identifying locations of NO_3^- removal. Although NO_3^- attenuation became more widespread in larger mixing zones, the mean reaction rate on a per unit area basis decreased as mixing intensified (Figure 4.10c). Large mixing zones removed more NO_3^- and as removal approached 100%, the supply of reactants and hence mean reactivity on a per unit area basis declined. Thus, percent removal can be inferred based on the size of the mixing zone (Figure 4.10d). However, reactivity also depends on groundwater velocity, which governs residence time, the extent of mixing, and the rate of solute supply. Larger quantities of NO_3^- were removed as the average Darcy velocity in the reaction zone increased (Figure 4.10e). Higher velocities led to greater mixing and increased solute supply to drive higher rates of NO_3^- removal.

Although Figure 4.10 demonstrates several relationships between physical characteristics and beach reactivity, there is no strong correlation between removal efficiency or total NO_3^- or S removed for a wide assortment of other parameters, including non-dimensional numbers from literature that have successfully been used to predict physical properties of flow and transport in these systems [e.g. Robinson et al., 2007; Evens and Wilson, 2016; Greskowiak, 2014] (Figure B-1 and Figure B-2).

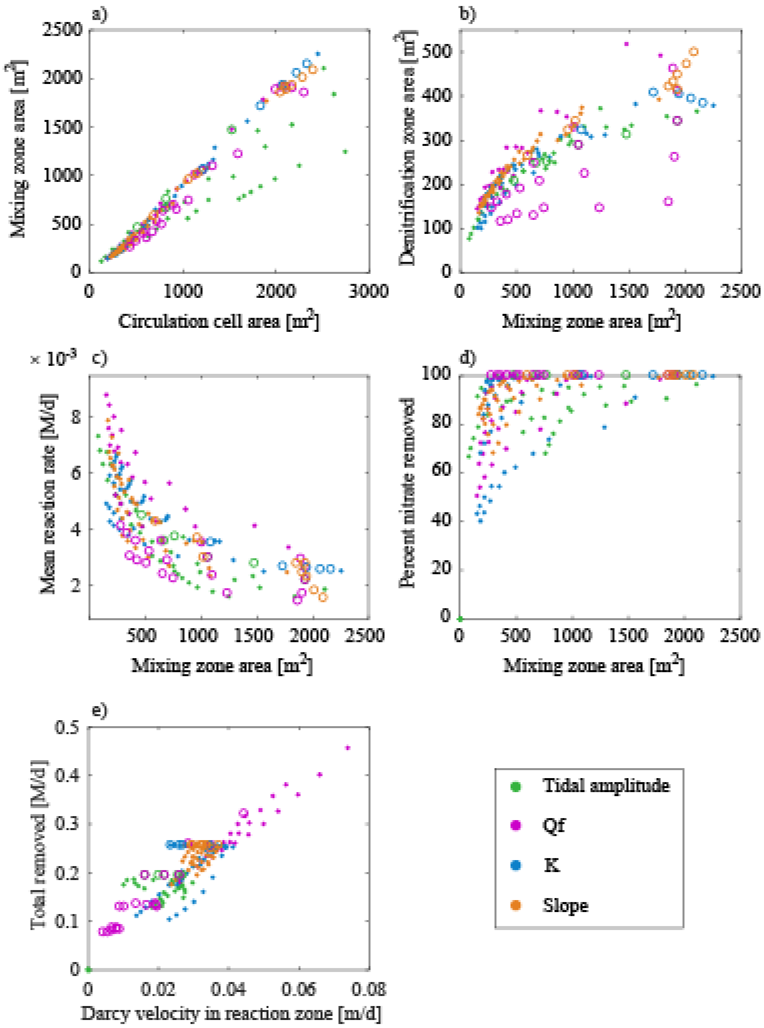

Figure 4.10 Relationships between phyiscal characteristics of the aquifer and denitrification. a) Mixing zone area as a function of the size of the ciruclation cell, b) reaction zone area, c) mean reaction rate, d) percent NO_3^- removed as a function of the area of the mixing zone, and e) percent of NO_3^- removed as a function of the ratio of freshwater flux to the area of the mixing zone. Open circles indicate simulations with 100% removal.

In contrast to denitrification, the percent of SO_4^{2-} transformed was not correlated with the size of the mixing zone (Figure 4.11a), rather the amount of SO_4^{2-} transformed generally increased with the size of the circulation cell, which included groundwater greater than 10 ppt (Figure 4.11b). There was also a positive correlation between the amount of sulfate transformed and the Da number and tidally-driven circulation (Figure 4.11c-4.11d). The correlations between the size of the circulation cell, the Da number, and tidally-driven circulation share a similar explanation. A greater quantity of SO_4^{2-} entered the beach with an increase in tidally-driven flow, which lead to larger circulation cells, longer residence times, and hence larger Da numbers. Thus, the increase in total SO_4^{2-} transformed was due to an increase in supply of SO_4^{2-} and longer residence times.

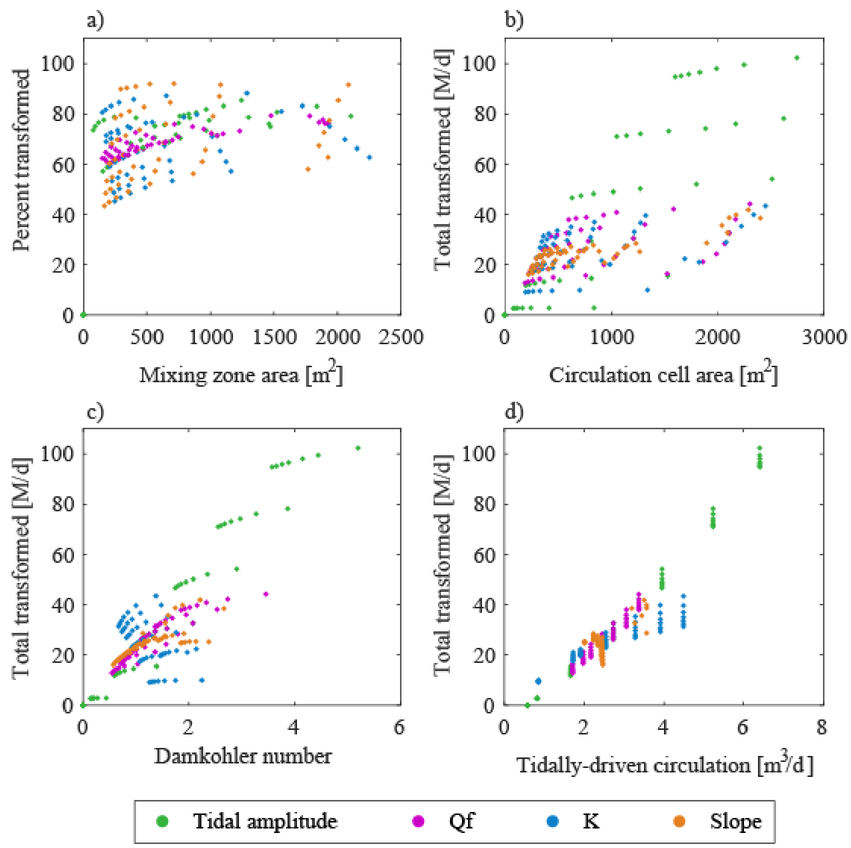

Figure 4.11. Relationships between phyiscal characteristics of the aquifer and sulfate reduction. a) Percent SO_4^{2-} removed as a function of the area of the mixing zone, b) total SO_4^{2-} removed as a function of area of the ciruclation cell, c) total SO_4^{2-} removed as a function of the Damkohler number, d) total SO_4^{2-} removed as a function of the volume of ciruclating seawater.

4.4.2 Mixing-dependent and Mixing-independent Reactions

This study focused on the importance of five key physical factors on controlling the reactivity of solutes involved in reactions that require mixing and those involved in reactions that do not require mixing. To test the importance of these controls, denitrification was modeled as an example 1st-order reaction that required mixing and sulfate reduction was modeled as an example 0th-order reaction that did not require mixing. Although sulfate reduction was modeled as a 0^{th} order reaction, we recognize that it would not occur in sections of the aquifer where oxygen and NO_3^- is present. This simple modeling approach for sulfate reduction is used as a basis for understanding the physical controls on reactions that do not require mixing. Despite the simplified kinetics, the simulated variations in flow and transport regimes led to distinct patterns in solute removal for each physical factor that are used here to identify the set of hydrologic and hydrogeologic parameters that result in the most reactive beach for mixing-dependent and mixing-independent reactions.

The interplay between mixing intensity, residence time, and solute supply for denitrification, a mixing-dependent reaction, as shown in this study demonstrates that a system with a moderate tidal amplitude, high K, high freshwater flux, and a steep beach with high dispersion are likely to attenuate the largest quantity of land-derived NO3- prior to discharge.

Reactions that do not require mixing have physical controls that differ from reactions that require mixing. A large tidal amplitude, low K, and gentle sloping beach will promote transformation of solutes involved in non-mixing reactions. The results suggest that any combination of physical factors that results in the largest influx of reactive solute across the beachface and produces the longest residence time will yield the most reactive beach for these types of reactions.

Anthropogenic disturbances that modify one or more of the 5 physical factors should be considered when evaluating the reactivity of beach aquifers, in particular their efficiency as a NO_3^- sink for bioavailable N for nearshore ecosystems and for altering S cycling in coastal aquifers. These disturbances include but are not limited to beach nourishment, scraping, dune building, construction of ponds, and land use changes. Such disturbances alter intertidal slope, terrestrial freshwater flux, and sediment permeability and distribution within the beach. A more comprehensive understanding of the interplay between these physical factors as gained in this study may be used to engineer beaches to promote reactivity for different types of reactions. Adverse effects of altering the physical controls should also be considered. For example, beach scraping lowers the beach slope which would reduce reactivity for mixing-dependent reactions. However, gentle sloping beaches simultaneously increase mixing-independent reactions. Moreover, beach nourishment projects may produce a more homogenous and poorly mixed aquifer, thus reducing mixing-dependent reactions while not affecting mixing-independent reactions. It is recommended that beach managers take into account the effects of these human disturbances on reactivity when formulating best coastal zone management practices.

4.4.3 Model Simplifications

The mean of the highest denitrification rates for all simulations, 0.3 mmol m^{-2} d^{-1} (SD 0.02 mmol m^{-2} d^{-1}), is at the lower end of the range (0.1-5.9 mmol m^{-2} d^{-1}) for subtidal sediments [Huettel et al., 2014], and outside of the range for denitrification rates (2.1-9 mmol m^{-2} d^{-1}) in the Wadden Sea intertidal sandflat [Gao et al., 2012] and those estimated by Schutte et al. [2015] for a sandy beach (3.3-19 mmol m^{-2} d^{-1}). The lower NO_3^- consumption rates simulated in this study can be explained by several factors and are discussed in this section along with simplifying assumptions of our modeling approach.

We considered denitrification as the primary pathway for NO_3^- attenuation, however alternative NO_3^- transformation mechanisms and other N cycling pathways may play a role in affecting fluxes of bioavailable N to the water column. We chose to omit N mineralization and nitrification as the focus of this study is on the effects of physics on mixing-dependent and mixing-independent reactions, and denitrification satisfied the requirements of a mixing-dependent reaction. Nitrification increases the availability of NO_3^- for discharge and thus actual NO_3^- fluxes in SGD may be higher than our estimates in real-word systems. Where that is the case, our simulations would overestimate removal rates as a percentage of the combined DOC- and terrestrially-derived NO_3^- flux through the intertidal zone. However, nitrification promotes denitrification by producing NO_3^- and lowering O_2 concentrations, and thus our models may be underestimating total and percent removal rates. In either case, NO_3^- loading supported by nitrification of ammonium produced by marine-derived DOC mineralization is recycled bioavailable N from surface water rereleased back into the marine ecosystem, and we are therefore confident that our results represent removal rates and NO_3^- fluxes central to altering net marine ecosystem productivity.

Alternative NO_3^- reduction processes may also influence the fate and fluxes of NO_3^- in coastal aquifers. Dissimilatory NO_3^- reduction to ammonium (DNRA) occurs under the same redox conditions as denitrification and competes with denitrification as an additional NO_3^- reduction mechanism. Microbial oxidation of reduced sulfur (S^-), typically in the form of iron sulfide (pyrite), to SO_4^{2-} can also provide a viable electron donor for denitrification [Schutte et al., 2015; Cardoso et al., 2006], as can oxidation of reduced Fe^{2+} [Korom, 1992]. In sediments where labile DOC is limited, these alternative NO_3^- reduction processes may increase NO_3^- attenuation [Korom, 1992; Robertson, 1996; Kelso et al., 1997; Moncaster et al., 2000; Tesoriero et al., 2000].

We assumed homogenous media in our models to provide a first-order estimate of the efficiency of shallow coastal aquifers in attenuating solutes involved in mixing-dependent and mixing-independent reactions. Nevertheless, heterogeneity can significantly increase NO_3^- removal in aquatic sediments [Sawyer, 2014], suggesting that our results represent a lower bound for NO_3^- removal.

Wave swash and setup, diurnal and spring-neap variability in tidal amplitude, seasonal variability in recharge, storm events, and climate cycles alter flow paths and residence times, and control the extent and intensity of mixing in nearshore aquifers [Ataie-Ashtiani et al., 1999; Li et al., 1999; Michael et al., 2005; Robinson et al., 2007; Abarca et al., 2013; Bakhtyar et al., 2013; Gonneea et al., 2013; Anwar et al., 2014; Gonneea and Charette, 2014; Heiss et al., 2014; Heiss and Michael, 2014; Robinson et al., 2014; Xin et al., 2014; Heiss et al., 2015]. These hydrologic forcing mechanisms operate across a wide range of temporal and spatial scales and interact to form complex and highly dynamic flow regimes and mixing patterns more complicated those brought about by the constant freshwater flux boundary and sinusoidal tidal signal used in this study. The oscillatory flows and movement of redox boundaries resulting from transient hydrologic forcing mechanisms is likely to be important for determining the distribution and type of microbial communities in the aquifer. For example, if the length of time that microorganisms require to become active when conditions are favorable is longer than the interval of time over which the geochemical environment changes due to moving redox boundaries, then the rate of N and S cycling and other chemical transformations may be diminished. Alternatively, interaction between land-ocean hydrologic forcings may lead to more dispersed and stable mixing zones where denitrifying communities may thrive, enhancing NO_3^- removal [Santoro et al., 2010].

Nutrient cycling along the lower saltwater-freshwater interface can attenuate nitrogen loads in submarine groundwater discharge [Kroeger and Charette, 2008; Spiteri et al., 2008; Anwar et al., 2014]. This study was designed to investigate mixing-dependent and mixing-independent reactions in the saltwater circulation cell and therefore omits biogeochemical processes occurring along the lower interface. Simultaneous consideration of nutrient transformations in the intertidal mixing zone and the lower interface should be addressed in future studies to put our estimates into context with nutrient transformations in other regions of the coastal aquifer.

4.5 Conclusion

A sensitivity analysis was conducted on the effects of tidal amplitude, hydraulic conductivity, freshwater flux, beach slope, and dispersivity on nutrient cycling in tidally-influenced beach saltwater-freshwater mixing zones. The importance of these five key physical factors on reactivity was assessed for mixing-dependent and mixing-independent reactions. To explore the linkages between physics and these two types of reactions, labile dissolved organic carbon, dissolved oxygen, nitrate, sulfate, nitrite, and sulfide, representing the key chemical species involved in aerobic respiration, denitrification, and sulfate reduction were simulated. The simulations demonstrate that variability in the 5 physical factors, in addition to DOC reactivity, over a range of real-world values can significantly modify fluxes of nitrate and sulfate to the coastal ocean by altering residence times, the supply and transport of reactive species through the beach aquifer, and the intensity of mixing between fresh and saline groundwater endmembers.

Denitrification occurred at the boundary of the intertidal circulation cell in an-arc shaped denitrifcation zone of groundwater between 1 and 10 ppt. Nitrate consumption was highest on the landward side of the circulation cell and decreased along circulating flow paths from the high to low tide marks. Sensitivity tests showed that the size of the mixing zone was the primary physical characteristic controlling nitrate removal. In contrast, sulfate reduction took place on the inside of the circulation cell where groundwater was greater than 10 ppt. Sulfate reduction was highest immediately beneath the beach surface where seawater recharged the aquifer and was controlled primarily by the supply of sulfate entering the aquifer across the beachface.

Nitrate and sulfate removal varied significantly over the range of real-world hydrologic and beach conditions. Tidal amplitude was the most important factor moderating nitrate transformation (0-100% removed), followed by hydraulic conductivity (40-100%), freshwater flux (51-100%), beach slope (68-100%), and dispersivity (82-100%). The transformation of sulfate to sulfide was most affected by K (50-100% removed) and beach slope (50-100%), while tidal amplitude (68-100% removal) and freshwater flux (69-74%) were of secondary importance. These results demonstrate that mixing-dependent and mixing-independent reactions occur in different locations and have different hydrologic and hydrogeologic controls.

The size of the mixing zone and residence time are correlated to reactivity for mixing-dependent reactions while solute supply and residence time are responsible for controlling reactivity for mixing-independent reactions. There is a lack of correlation between reactivity and numerous other physical characteristics and non-dimensional numbers published in literature, emphasizing the complexity of the interactions between the physical and biogeochemical factors controlling nutrient removal in these systems.

The results of this study may be useful to coastal managers aiming to moderate nutrient loads to nearshore ecosystems. Beaches can be engineered to promote reactivity to reduce groundwater nutrient loads, however in the same sense reactivity may diminish and nutrient loading can increase if engineering measures fail to consider the adverse effects of altering the 5 physical factors investigated in this study. Nevertheless, the findings demonstrate that sandy beaches play a vital role in cycling sulfur and removing terrestrial NO_3^- as a new N source to coastal surface waters prior to discharge, suggesting that intertidal zones provide a valuable yet unseen ecological service that may be ubiquitous along much of the world's coastline.

REFERENCES

Abarca, E., H. Karam, H. F. Hemond, and C. F. Harvey (2013), Transient groundwater dynamics in a coastal aquifer: The effects of tides, the lunar cycle, and the beach profile, *Water Resour. Res.*, *49*, 1–16, doi:10.1002/wrcr.20075.

Anschutz, P., T. Smith, A. Mouret, J. Deborde, S. Bujan, D. Poirier, and P. Lecroart (2009), Tidal sands as biogeochemical reactors, *Estuar. Coast. Shelf Sci.*, *84*(1), 84–90, doi:10.1016/j.ecss.2009.06.015.

Ataie-Ashtiani, B., R. E. Volker, and D. A. Lockington (1999), Tidal effects on sea water intrusion in unconfined aquifers, *J. Hydrol.*, *216*(1-2), 17–31, doi:10.1016/S0022-1694(98)00275-3.

Anwar, N., C. Robinson, and D. A. Barry (2014), Influence of tides and waves on the fate of nutrients in a nearshore aquifer: Numerical simulations, *Adv. Water Resour.*, *73*(2014), 203–213, doi:10.1016/j.advwatres.2014.08.015.

Appelo, C. A. J., and D. Postma (2005), Geochemistry, Groundwater and Pollution, Second Edition, CRC Press, Leiden, The Neatherlands.

Amato, D. W., J. M., Bishop, C. R. Glenn, H. Dulai, and C. M. Smith (2016), Impact of Submarine Groundwater Discharge on Marine Water Quality and Reef Biota of Maui, *PLoS ONE*, 11(11), e0165825, https://doi.org/10.1371/journal.pone.016582.

Bardini, L., F. Boano, M. B. Cardenas, R. Revelli, L. Ridolfi (2012). Nutrient cycling in bedform induced hyporheic zones, *Geochimica et Cosmochimica Acta*, 84(2012), 47–61. http://doi.org/10.1016/j.gca.2012.01.025.

Beck, M., O. Dellwig, G. Liebezeit, B. Schnetger, and H. -J. Brumsack (2008), Spatial and seasonal variations of sulphate, dissolved organic carbon, and nutrients in deep pore waters of intertidal flat sediments, *Estuarine, Coastal and Shelf Science*, 79(2), 307–316. doi:10.1016/j.ecss.2008.04.007.

Berner, R. A. (1981), Authigenic minerals resulting from organic matter decomposition in modern sediments, *Fortschritte Der Mineralogie*, 59, 117–135.

Boufadel, M. C. (2000), A mechanistic study of nonlinear solute transport in a groundwater – surface water system under steady state and transient hydraulic conditions, *Water Resour.*, *36*(9), 2549–2565.

Briggs, M. A, F. D. Day-lewis, J. P. Zarnetske, and J. W. Harvey (2015), A physical explanation for the development of redox microzones in hyporheic flow, *Geophys. Res. Lett.*, 1–9, doi:10.1002/2015GL064200.

Burnett, W. C., G. Wattayakorn, M. Taniguchi, H. Dulaiova, P. Sojisuporn, S. Rungsupa, T. Ishitobi (2007), Groundwater-derived nutrient inputs to the Upper Gulf of Thailand, *Cont. Shelf Res*, 27,176–90.

Cardoso, R. B., R. Sierra-Alvarez, E. R. Flores, J. Gómez, and J. A. Field (2006), Sulfide oxidation under chemolithoautotrophic conditions, Biotechnol. Bioeng., 95(6), 1148–1157.

Charbonnier, C., P. Anschutz, D. Poirier, S. Bujan, P. Lecroart (2013), Aerobic respiration in a high-energy sandy beach, *Marine Chemistry,* 155, 10–21, doi:10.1016/j.

Charette, M. A., and E. R. Sholkovitz (2002), Oxidative precipitation of groundwater-derived ferrous iron in the subterranean estuary of a coastal bay, *Geophys. Res. Lett*., 29(10), 1444, doi:10.1029/2001GL014512.

Evans, T. B., and A. M. Wilson, (2016), Groundwater transport and the freshwater – saltwater interface below sandy beaches, *Journal of Hydrology*, 538, 563–573. http://doi.org/10.1016/j.jhydrol.2016.04.014.

Fan, D., R. P. Anitori, B. M. Tebo, and P. G. Tratnyek (2013), Reductive sequestration of pertechnetate ($^{99}TcO_4^-$) by nano zerovalent iron (nZVI) transformed by abiotic sulfide, *Environ. Sci. Technol*., 47, 5302–5310, doi:10.1021/es304829z.

Galloway, J. N., J. D. Aber, and J.W. Erisman (2003), The nitrogen cascade, *BioScience*, 53(4), 341–356.

Gao, H. M. Matyka, B. Liu, A. Khalili, J. E. Kostka, G. Collins, S. Jansen, M. Holtappels, M. M. Jensen, T. H. Badewien, M. Beck, M. Grunwald, D. de Beer, G. Lavik, and M. M. M. Kuypers (2012), Intensive and extensive nitrogen loss from intertidal permeable sediments of the Wadden Sea, *Limnol. Oceanogr.*, *57*(1), 185–198, doi:10.4319/lo.2012.57.1.0185.

Geng, X., and M. C. Boufadel (2015), Numerical study of solute transport in shallow beach aquifers subjected to waves and tides, *J. Geophys. Res. Ocean.*, 120(2), doi:10.1002/2014JC010539.

Gonneea, M. E., A. E. Mulligan, and M. A. Charette (2013), Climate-driven sea level anomalies modulate coastal groundwater dynamics and discharge, *Geophys. Res. Lett.*, 40(11), 2701–2706, doi:10.1002/grl.50192.

Gonneea, M. E., and M. A. Charette (2014), Hydrologic Controls on Nutrient Cycling in an Unconfined Coastal Aquifer, *Environ. Sci. Technol.*, 48, 14178–14185.

Greskowiak, J. (2014), Tide-induced salt-fingering flow during submarine groundwater discharge, *Geophys. Res. Lett.*, *41*, 6413–6419, doi:10.1002/2014GL061184.

Gu, C.H., G. M. Hornberger, A. L.Mills, J. S. Herman, and S.A. Flewelling (2007), Nitrate reduction in streambed sediments: Effects of flow and bio-geochemical kinetics, *Water Resour. Res*., *43*(12), W12413, doi:10.1029/ 2007WR006027.

Heiss, J. W., J. A. Puleo, W. J. Ullman, and H. A. Michael (2015), Coupled surface-subsurface hydrologic measurements reveal infiltration, recharge, and discharge dynamics across the swash zone of a sandy beach, *Water Resour. Res.*, 1, doi:10.1002/2015WR017395.

Heiss, J. W., and H. A. Michael (2014), Saltwater-freshwater mixing dynamics in a sandy beach aquifer over tidal, spring-neap, and seasonal cycles, *Water Resour. Res.*, *50*, 6747–6766, doi:10.1002/2014WR015574.

Heiss, J. W., W. J. Ullman, and H. A. Michael (2014), Swash zone moisture dynamics and unsaturated infiltration in two sandy beach aquifers, *Estuar. Coast. Shelf Sci.*, *143*, 20–31, doi:10.1016/j.ecss.2014.03.015.

Huettel, M., P. Berg, and J. E. Kostka (2014), Benthic exchange and biogeochemical cycling in permeable sediments, *Annu. Rev. Mar. Sci*., *6*, 23–51, doi:10.1146/annurev-marine-051413-012706.

Hunter, K. S., Y. Wang, and P. Van Cappellen (1998), Kinetic modeling of microbially-driven redox chemistry of radionuclides in subsurface environments: Coupling transport, microbial metabolism and geochemistry, *J. Contam. Hydrol.*, *209*, 53–80, doi:10.1016/S0169-7722(00)00158-3.

Jung, H. B., M. A. Charette, and Y. Zheng (2009), Field, laboratory, and modeling study of reactive transport of groundwater arsenic in a coastal aquifer, *Environ. Sci. Technol*., *43,* 5333–5338. doi:10.1021/es900080q.

Kelso, B. H. L., R. V. Smith, R. J. Laughlin, S. D. Lennox (1997), Dissimilatory nitrate reduction in anaerobic sediments leading to river nitrite accumulation. *Appl. Environ. Microb*., *63*(12), 4679–4685.

Korom, S. F. (1992), Natural denitrification in the saturated zone: a review, *Water Resour. Res*. *28*(6), 1657–1668.

Kroeger, K. D., and M. A. Charette (2008), Nitrogen biogeochemistry of submarine groundwater discharge, *Limnol. Oceanogr*., *53*(3), 1025–1039, doi:10.4319/lo.2008.53.3.1025.

Kuan, W. K., G. Jin, P. Xin, C. Robinson, B. Gibbes, L. Li (2012), Tidal influence on seawater intrusion in unconfined coastal aquifers, *Water Resources Research*, 48(2), 1–11. https://doi.org/10.1029/2011WR010678.

Langevin, C.D., Thorne, D.T., J., Dausman, A.M., Sukop, M.C., Guo, W., 2007. Seawat version 4: a computer program for simulation of multi-species solute and heat transport. Technical Report, U.S. Geological Survey Techniques and Methods Book 6, Chapter A22, 39 pp.

Lebbe, L. (1999), Parameter identification in fresh-saltwater flow based on borehole resistivities and freshwater head data, *Adv. Water Resour.*, *22*(8), 791–806.

McAllister, S. M., J. M. Barnett, J. W. Heiss, A. J. Findlay, D. J. Macdonald, C. L. Dow, G. W. Luther, H. A. Michael, and C. S. Chan (2015), Dynamic hydrologic and biogeochemical processes drive microbially enhanced iron and sulfur cycling within the intertidal mixing zone of a beach aquifer, *Limnol. Oceanogr.*, *60*(1), 329–345, doi:10.1111/lno.10029.

Meile, C., W. P. Porubsky, R. L. Walker, and K. Payne (2010), Natural attenuation of nitrogen loading from septic effluents: Spatial and environmental controls., *Water Res.*, *44*(5), 1399–408, doi:10.1016/j.watres.2009.11.019.

Michael, H. A., Mulligan, A. E., and Harvey, C. F. (2005), Seasonal oscillations in water exchange between aquifers and the coastal ocean, *Nature*, 436, 1145–1148.

Moore, W. S., J. L. Sarmiento, and R. M. Key (2008), Submarine groundwater discharge revealed by ^{228}Ra distribution in the upper Atlantic Ocean, *Nat. Geosci*., 1, 309–311, doi:10.1038/ngeo183.

Moncaster, S. J., S. H. Bottrell, J. H. Tellam, J. W. Lloyd, K. O. Konhauser (2000), Migration and attenuation of agrochemical pollutants: insights from isotopic analysis of groundwater sulphate, *J. Contam. Hydrol*., 43(2), 147–163.

Niencheski, L. F. H , H. L. Windom, W. S. Moore, R. A. Jahnke (2007), Submarine groundwater discharge of nutrients to the ocean along a coastal lagoon barrier, southern Brazil, *Marine Chem*, 106,546–61.

Ocampo, C. J., C. E. Oldham, and M. Sivapalan (2006), Nitrate attenuation in agricultural catchments: Shifting balances between transport and reaction, *Water Resour. Res*., 42, W01408, doi:10.1029/2004WR 003773.

Paerl, H., J. Pinckney, J. Fear, B. Peierls (1998), Ecosystem responses to internal and watershed organic matter loading: consequences for hypoxia in the eutrophying Neuse River Estuary, North Carolina, USA, *Marine Ecology Progress Series*, 166, 17–25.

Parkhurst, D. L., and C. A. J. Appelo, User's guide to PHREEQC (version 2) - A computer program for speciation, batch-reaction, one dimensional transport, and inverse geochemical calculations. US Department of the Interior, Water Resources Investigations Report 99-4259, 1999.

Post, V. E. A. (2011), A new package for simulating periodic boundary conditions in MODFLOW and SEAWAT, *Computers and Geosciences*, 37(11), 1843-1849. doi:10.1016/j.cageo.2011.01.012.

Prommer H, Post V. A reactive multicomponent transport model for saturated porous media. Contaminated Land Assessment and Remediation Research Centre, The University of Edinburgh, UK; 2002.

Reckhardt, A., M. Beck, M. Seidel, T. Riedel, A. Wehrmann, A. Bartholomä, B. Schnetger, T. Dittmar, and H.-J. Brumsack (2015), Carbon, nutrient and trace metal cycling in sandy sediments: A comparison of high-energy beaches and backbarrier tidal flats, *Estuar. Coast. Shelf Sci.*, *159*, 1–14, doi:10.1016/j.ecss.2015.03.025.

Rivett, M. O., S. R. Buss, P. Morgan, J. W. N. Smith, and C. D. Bemment (2008), Nitrate attenuation in groundwater: A review of biogeochemical controlling processes, *Water Res.*, *42*(16), 4215–4232, doi:10.1016/j.watres.2008.07.020.

Robertson, W. D., Russell, B.M., Cherry, J.A., 1996. Attenuation of nitrate in aquitard sediments of southern Ontario, *J. Hydrol*., 180(1), 267–281.

Robinson, C., B. Gibbes, H. Carey, and L. Li (2007a), Salt-freshwater dynamics in a subterranean estuary over a spring-neap tidal cycle, *J. Geophys. Res.*, *112*(C9), 1–15, doi:10.1029/2006JC003888.

Robinson, C., L. Li, and D. A. Barry (2007b), Effect of tidal forcing on a subterranean estuary, *Advances in Water Resources*, 30(4), 851–865. https://doi.org/10.1016/j.advwatres.2006.07.006

Robinson, C., P. Xin, L. Li, and D. A. Barry (2014), Groundwater flow and salt transport in a subterranean estuary driven by intensified wave conditions, *Water Resour. Res.*, *50*, 165–181, doi:10.1002/2013WR013813.

Robinson, C., B. Gibbes, and L. Li (2006), Driving mechanisms for groundwater flow and salt transport in a subterranean estuary, *Geophys. Res. Lett*., 33, L03402, doi:10.1029/2005GL025247.

Robinson, C., A. Brovelli,, D.A. Barry, and L. Li (2009), Tidal influence on BTEX biodegradation in sandy coastal aquifers, *Advances in Water Resources*, *32*(1), 16–28. doi:10.1016/j.advwatres.2008.09.008.

Robinson, C., P. Xin, L. Li, and D. A. Barry (2014), Groundwater flow and salt transport in a subterranean estuary driven by intensified wave conditions, *Water Resour. Res.*, *50*, 165–181, doi:10.1002/2013WR013813.

Roy, M., J. B. Martin, C. G. Smith, and J. E. Cable (2011), Reactive-transport modeling of iron diagenesis and associated organic carbon remineralization in a Flori*Da* (USA) subterranean estuary, *Earth Planet. Sci. Lett.*, *304*(1-2), 191–201, doi:10.1016/j.epsl.2011.02.002.

Russoniello, C. J., L. F. Konikow, K. D. Kroeger, C. Fernandez, A. S. Andres, and H. A. Michael (2016), Hydrogeologic controls on groundwater discharge and nitrogen loads in a coastal watershed, *Journal of Hydrology, 538*, 783–793.

Santoro, A. (2010), Microbial nitrogen cycling at the saltwater-freshwater interface, *Hydrogeology Journal*, 18, 187-202, dio:10.1007/s10040-009-0526-z.

Santos, I. R., W. C. Burnett, J. Chanton, B. Mwashote, I G. N. A. Suryaputra, and T. Dittmar, (2008), Nutrient biogeochemistry in a Gulf of Mexico subterranean estuary and groundwater-derived fluxes to the coastal ocean, *Limnology and Oceanography*, 53(2), 705-718, doi:10.4319/lo.2008.53.2.0705.

Santos, I. R., W. C. Burnett, T. Dittmar, I. G. N. a. Suryaputra, and J. Chanton (2009), Tidal pumping drives nutrient and dissolved organic matter dynamics in a Gulf of Mexico subterranean estuary, *Geochim. Cosmochim. Acta*, *73*(5), 1325–1339, doi:10.1016/j.gca.2008.11.029.

Santos, I. R., Burnett, W. C., Misra, S., Suryaputra, I. G. N. A., Chanton, J. P., Dittmar, T., … Swarzenski, P. W. (2011). Uranium and barium cycling in a salt wedge subterranean estuary: The influence of tidal pumping. *Chemical Geology*, *287*(1–2), 114–123.

Sawyer, A. H. (2014), Enhanced removal of groundwater-borne nitrate in heterogeneous aquatic sediments, *Geophysical Research Letters*, 403–410.

Schutte, C. A., S. B. Joye, A. M. Wilson, T. Evans, W. S. Moore, and K. Casciotti (2015), Intense nitrogen cycling in permeable intertidal sediment revealed by a nitrous oxide hot spot, *Global Biogeochem. Cycles*, *29*(10), 1584–1598, doi:10.1002/2014GB005052.

Slomp, C. P. and P. Van Cappellen (2004), Nutrient inputs to the coastal ocean through submarine groundwater discharge: controls and potential impact, *Journal of Hydrology* 295:64-86.

Spiteri, C., C. P. Slomp. K. Tuncay, C. Meile (2008a), Modeling biogeochemical processes in subterranean estuaries: Effect of flow dynamics and redox conditions on submarine groundwater discharge of nutrients. *Water Resources Research*, *44*(2), doi:10.1029/2007WR006071

Spiteri, C., C. P. Slomp, M. A. Charette, K. Tuncay, and C. Meile (2008b), Flow and nutrient dynamics in a subterranean estuary (Waquoit Bay, MA, USA): Field data and reactive transport modeling, *Geochim. Cosmochim. Acta*, *72*(14), 3398–3412, doi:10.1016/j.gca.2008.04.027.

Taniguchi, M., W. C. Burnett, H. Dulaiova, F. Siringan, J. Foronda, G. Wattayakorn, S. Rungsupa, E. A. Kontar, T. Ishitobi (2008), Groundwater discharge as an important land-sea pathway into Manila Bay, Philippines, *Journal of Coastal Research*, 24,15–24.

Tesoriero, A.J., H. Liebscher, S. E. Cox (2000), Mechanism and rate of denitrification in an agricultural watershed: electron and mass balance along groundwater flow paths, *Water Resour. Res.*, 36(6), 1545–1559.

Ullman, W. J., B. Chang, D. C. Miller, and J. A. Madsen (2003), Groundwater mixing, nutrient diagenesis, and discharges across a sandy beachface, Cape Henlopen, Delaware (USA), *Estuarine, Coastal and Shelf Science*, 57, 539-52.

Van Cappellen, P., and Y. Wang (1996), Cycling of iron and manganese in surface sediments: A general theory for the coupled transport and reaction of carbon, oxygen, nitrogen, sulfur, iron, and manganese, *Am. J. Sci.*, *296*(3), 197–243, doi:10.2475/ajs.296.3.197.

Valiela, I., J. McClelland, J. Hauxwell, P.J. Behr, D. Hersh, and K. Foreman (1997), Macroalgal blooms in shallow estuaries: Controls and ecophysiological and ecosystem consequences. *Limnology and Oceanography*, 42, 1105–1118.

Xin, P., S. S. J. Wang, C. Robinson, L. Li, Y.-G. Wang, and D. A. Barry (2014), Memory of past random wave conditions in submarine groundwater discharge, *Geophys. Res. Lett.*, *41*, doi:10.1002/2014GL059617.

Zarnetske, J. P., R. Haggerty, S. M. Wondzell, V. a. Bokil, and R. González-Pinzón (2012), Coupled transport and reaction kinetics control the nitrate source-sink function of hyporheic zones, *Water Resour. Res.*, *48*(11), 1–15, doi:10.1029/2012WR011894.

Chapter 5

CONCLUSION

These studies focus on the hydrologic and biogeochemical frameworks of sandy beach aquifers where terrestrially-derived freshwater and marine-derived saltwater mix in the intertidal subsurface due to tide and wave action. The hydrologic and biogeochemical frameworks of these systems are characterized through investigation of groundwater flow, solute transport, and biogeochemistry in response to multiple hydrologic driving mechanisms. Field and numerical modeling experiments demonstrate the effects of seasonality in aquifer recharge, tides, waves, and other hydrologic drivers on intertidal salinity dynamics and patterns of groundwater recharge and discharge across the beachface at Cape Henlopen, Delaware. The improved understanding of the response of the physical flow and transport system to tides was used to explore linkages between the physical and biogeochemical processes occurring in intertidal mixing zones. The combined hydrologic-biogeochemical investigative approach has allowed for a more comprehensive understanding of the interplay between physical processes of flow and transport, and biogeochemical reactivity in beach aquifers. Tides and waves significantly modify groundwater flow paths, residence times, and the intensity and extent of mixing between fresh and saline groundwater in coastal aquifers across time scales ranging from seconds to months. Chemical cycling and the fate and fluxes of nutrients across the aquifer-ocean interface is controlled strongly by these physical flow and transport processes, and in turn is dependent on the hydrologic forcing mechanisms acting on these systems.

5.1 Transience of Beach Aquifers under Tidal and Wave Influence

Groundwater flow and salinity in the Cape Henlopen beach aquifer is highly dynamic, responding to seasonal recharge variations, spring-neap cycling, tidal stage, and precipitation events. The structure and size of the intertidal circulation cell varies monthly in response to seasonal fluctuations in the freshwater hydraulic gradient. Salinity is highest and the intertidal saltwater-freshwater mixing zone is largest during summer months when groundwater recharge and the freshwater hydraulic gradient is low, and an increase in recharge and a stronger freshwater hydraulic gradient in spring months leads to freshwater dilution, lower salinities, and a small mixing zone in the spring. Within the seasonal salinity pattern, regular, pulsed injections of seawater across the upper beachface at biweekly and monthly spring tides leads to oscillations in the size of the intertidal mixing zone as the additional mass of saltwater introduced at spring tide circulates through the beach before discharging. Storm events, beach topography, and tidal stage are less controlling relative to seasonal and spring-neap effects. Seasonal sea-level anomalies have no observable effect on groundwater flow and transport patterns at Cape Henlopen.

Infiltration, recharge, and discharge zones form in the intertidal zone due to spatial and temporal variability in groundwater-surface water exchange due to wave swash and tides. A region of elevated saturation forms in the shallow unsaturated zone as a result of swash infiltration and serves as a source of seawater to the water table as it flows vertically downward through the unsaturated zone. The presence of a region of sediment with high water content and downward flow in the shallow unsaturated zone is responsible for the shiny and saturated appearance on the sand surface typically accepted in literature as a zone of groundwater discharge. Moreover, the exit point, marking the cross-shore location on the beachface below which groundwater discharges, is located farther seaward relative to its apparent location identified based on common practice of using beachface saturation as a proxy for the direction of vertical flow across the sand surface. The coupled surface-subsurface measurements show for the first time the transience and variability in the size and location of zones of infiltration, recharge, and discharge at swash and tidal time scales. The widths of the infiltration and recharge zones are controlled primarily by wave swash while the locations are controlled by the tide. The zone of groundwater discharge on the beachface is also controlled by the tide; the discharge zone is narrow on rising tide as the tide level moves up the beach more rapidly than the water table can respond, resulting in a narrow discharge zone and net flow into the aquifer. Swash events easily extend landward of the water table-beachface intersection at this stage in the tidal cycle, hence infiltration and recharge zones form across the unsaturated portion of the beachface. On ebb tide the tide level falls more rapidly than the beach water table so the discharge zone widens and there is a net flow of water out of the beach into the surface water.

5.2 Biogeochemical Response

Numerical modeling sensitivity tests were performed to evaluate the influence of tidal amplitude, terrestrial freshwater flux, hydraulic conductivity, beach slope, and dispersivity on nutrient cycling in the intertidal circulation cell. The simulations show that changes to groundwater flow paths, residence times, and the extent and intensity of mixing between saline and freshwater due to changes in these physical factors significantly alters the distribution and fate of nutrients in the circulation cell. Denitrification occurs on the boundary of the circulation cell where fresh and saltwater mix and aerobic respiration takes place in the interior of the circulation cell near the sand surface where salinity is highest. Removal efficiencies of terrestrially-derived nitrate vary the most across a range of typical tidal amplitudes, followed by typical values of hydraulic conductivity, freshwater flux, beach slope, and dispersivity. Nitrate removal is highest for beaches with a moderately sized tidal amplitude, high hydraulic conductivity, low freshwater flux, and a gentle sloping beach with high dispersion. This set of parameters yields the largest intertidal saltwater-freshwater mixing and reaction zone while maintaining a residence time that is long enough to allow complete removal of oxygen, but short enough for DOC not to fully degrade. The remaining DOC drives nitrate reduction along the boundary of the circulation cell. The bulk sulfate reduction rate in the intertidal zone also depends on the physical flow system; sulfate reduction generally increases with the size of the mixing zone.

5.3 Implications

Quantification of chemical loads in SGD is crucial for predicting ecosystem health, but reliably quantifying SGD and associated chemical loads is difficult in practice. Among other issues, seepage meter deployments are labor intensive and thus the number of observation points are often limited in space and time. This can lead to extrapolation of fluid and solute fluxes across large and often geologically complex areas in an attempt to estimate total chemical loads to surface water bodies. Extrapolation may also be done over time without considering hydrologic variability, mixing dynamics, or biogeochemical complexities. This study shows that mixing between salt and fresh water in beach aquifers and SGD varies across the intertidal and subtidal zone, responding to forcings that modify subsurface hydrology from the centimeter to decameter scale. Moreover, the findings show that because waves, tides, and the seasonal variations in the terrestrial freshwater gradient operate on different time scales, flow and mixing is these systems is highly dynamic. Thus, our results indicate that measurements of SGD, solute fluxes, solute distributions, redox conditions, and reaction rates should be cautiously extrapolated across space and through time.

Submarine groundwater discharge is ubiquitous along the U.S. coastline [Sawyer et al., 2016], yet research on chemical delivery to the ocean and public interest and awareness is focused primarily on streams and rivers due to the visibility and accessibility of surface water and the relative ease at which measurements can be collected. However, SGD is an important nutrient transport pathway [Johannes, 1980; Capone and Bautista, 1985; Garrison et al., 2003; Slomp and Van Capellan, 2004; Santos et al., 2008; Russoniello et al., 2016] and therefore must be considered when evaluating total chemical fluxes to estuarine and marine environments. A crucial step in this process is understanding how the physical driving mechanisms of flow and transport affect the hydrologic framework of coastal aquifers, and in turn the transformations that chemicals in SGD may undergo prior to discharge. This study takes that step by demonstrating the role of tides and waves in altering flow and transport behavior and shows the importance of beach aquifers in attenuating solutes in SGD. Transformation of chemicals prior to discharge is becoming increasingly recognized as a valuable ecological service as researchers place more emphasis on understanding linkages between hydrology, oceanography, biogeochemistry, climatology, and geology – disciplines that have traditionally investigated coastal groundwater systems independently from one another. This study is the first to include many of these disciplines to reveal the extent to which hydrologic forcings establish and alter groundwater flow and transport patterns, and biogeochemical processes that affect marine ecosystem health. Hence the interdisciplinary efforts in this study illustrate that surface water, groundwater, and biogeochemistry are tightly coupled and should be investigated together when estimating chemical loads to the coastal ocean.

5.4 Recommendations for Future Work

Important research gaps remain unanswered concerning the influence of tides and waves on the biogeochemical significance of sandy beaches in moderating chemical fluxes to the ocean. These gaps may be filled through future work by considering more hydrologically, geologically, and biogeochemically complex systems, as discussed below.

The highly transient nature of intertidal flow and saltwater-freshwater mixing across a range of time scales has been well-documented in this study. However, other hydrologic and geologic factors are likely at play that have not been considered, yet are important to groundwater flow, transport, and reactivity at the coastline. Laboratory and numerical modeling experiments aimed at understanding pore-scale flow through the unsaturated zone and water content dynamics surrounding individual sediment grains in response to wave swash and tides would reveal information about the hydrologic habitat of microbes in the shallow beach, as well as information about how DOC and other surface water solutes are transported, filtered, sorbed, and chemically transformed once they enter the subsurface. At longer time scales, it is uncertain how the intertidal circulation cell responds to sea level rise and coastal morphological change, or decadal shifts in aquifer recharge due to climate change.

Long-term continuous monitoring and models that implement these processes and consider the combined effects of more hydrologic driving mechanisms acting on coastal groundwater systems would provide further assessment of the transience and resiliency of intertidal mixing zones to a wider range of conditions and would help answer questions such as: Can the circulation cell keep pace with a rising sea level and a changing climate? What type of beach aquifers are most susceptible to rising sea level, considering different sea level rise projections? How do microbial communities in the beach respond to transient redox conditions that vary from the tidal to climatic time scale? Are the ecological services provided by beach aquifers threatened by coastal erosion due to encroaching seas?

Geologic heterogeneity likely has a profound impact on flow and transport processes in the intertidal zone, however the effects of heterogeneity on these systems are unknown. Numerical models that incorporate heterogeneity at different spatial scales and that consider hydraulic conductivity fields with various degrees of connectedness can be used to further our understanding of the importance of geology on groundwater dynamics and nutrient cycling and determine if homogenous models can be used to represent the hydrogeology of real-word systems.

Groundwater-surface water exchange also has implications for sediment transport across the beach. Numerical models that couple groundwater and surface water flow with sediment transport would be useful for understanding how groundwater salinization due to wave overwash becomes more or less likely depending on the frequency of storm surges as dunes are eroded and the topography of the coastline changes with each overtopping event. Such studies would be able to assess how water table depth and moisture conditions in the unsaturated zone impact erosion and deposition in these environments.

The intertidal mixing zone can host many biogeochemical reactions with complex chemical transformation pathways that cycle nutrients other than those considered in this study. Future modeling studies would benefit from implementation of more chemical cycling pathways as well as more complex representations of chemical reactions. To better understand how mixing affects N, Fe, P, S, and C cycling, reaction networks should consider DOC mineralization and assimilation, nitrification, DNRA, Anammox, redox half-reactions, Fe reduction and oxidation, P adsorption and desorption, and pyrite oxidation and denitrification. More complex rate expressions that include the full Monod equation for the growth of microorganisms and different types of DOC representing a continuum of labile and semi-labile compounds would provide a better indication of how solutes are transformed along flow paths.

The temporal variability of the intertidal mixing zone shown in this study should be incorporated in to biogeochemical reactive transport models. Redox gradients that move with the mixing zone will undoubtedly be linked to the spatial distribution of reactivity at a given point in time. The growth and activation of microbial communities likely hinges on the mixing time scales between groundwater endmembers. Consideration of waves, tidal stage, spring-neap cycling, seasonal variability in recharge, and other transient forcing mechanisms that drive oscillatory flows and mixing across time scales should be considered in reactive transport models to reveal time lags that may exist between microbial activity and moving redox gradients. If time lags exist, solute fluxes and attenuation efficiencies may differ from those in this study.

The importance of several hydrologic forcing mechanisms on controlling nutrient fluxes in SGD has been demonstrated, however it is unclear how large-scale nutrient fluxes in SGD compare to those in streams and rivers along the same stretch of coastline. Thus, to put the nutrient fluxes presented in this study into broader context, total nutrient discharge via SGD along the U.S. coastline should be estimated and compared to nutrient loads in streams and rivers. This will greatly assist in determining the ecological value of coastal aquifers, as well as the importance of SGD as a contributor to the global ocean chemical budget relative to surface water sources.

REFERENCES

Capone D. G., and M. F. Bautista (1985), A groundwater source of nitrate in nearshore marine-sediments, *Nature*, 313:214–6.

Garrison G. H., C. R. Glenn, G. M. McMurtry (2003), Measurement of submarine groundwater discharge in Kahana Bay, O'ahu, Hawai'i, *Limnol. Oceanogr.*, 48, 920–8, http://dx.doi.org/10.4319/lo.2003.48.2.0920

Johannes, R. E. (1980), The ecological significance of the submarine discharge of groundwater, *Mar. Ecol. Prog. Ser., 3*, 365–373.

Santos, I.R., W. C. Burnett, J. Chanton, B. Mwashote, I G. N. A. Suryaputra, T. Dittmar, (2008), Nutrient biogeochemistry in a Gulf of Mexico subterranean estuary and groundwater-derived fluxes to the coastal ocean., *Limnology and Oceanography* 53, 705-718, doi:10.4319/lo.2008.53.2.0705.

Russoniello, C. J., L. F. Konikow, K. D. Kroeger, C. Fernandez, A. S. Andres, and H. A. Michael (2016), Hydrogeologic controls on groundwater discharge and nitrogen loads in a coastal watershed. *Journal of Hydrology, 538,* 783–793. http://doi.org/10.1016/j.jhydrol.2016.05.013.

Sawyer, A. H., David, C. H., and J. S. Famiglietti (2016), Continental patterns of submarine groundwater discharge reveal coastal vulnerabilities, *Science*, 1058.

Slomp, C. P. and P. Van Cappellen (2004), Nutrient inputs to the coastal ocean through submarine groundwater discharge: controls and potential impact, *Journal of Hydrology* 295:64-86.

Appendix A

SUPPLIMENTARY MATERIAL FOR CHAPTER 2

This supplementary material contains a figure to compare the concentrations and migration of the measured and simulated tracer plumes. The figure may help readers gain a better understanding of the quality of the match between the measured and simulated tracer plumes. The manuscript contains the details explaining when and how these data were obtained.

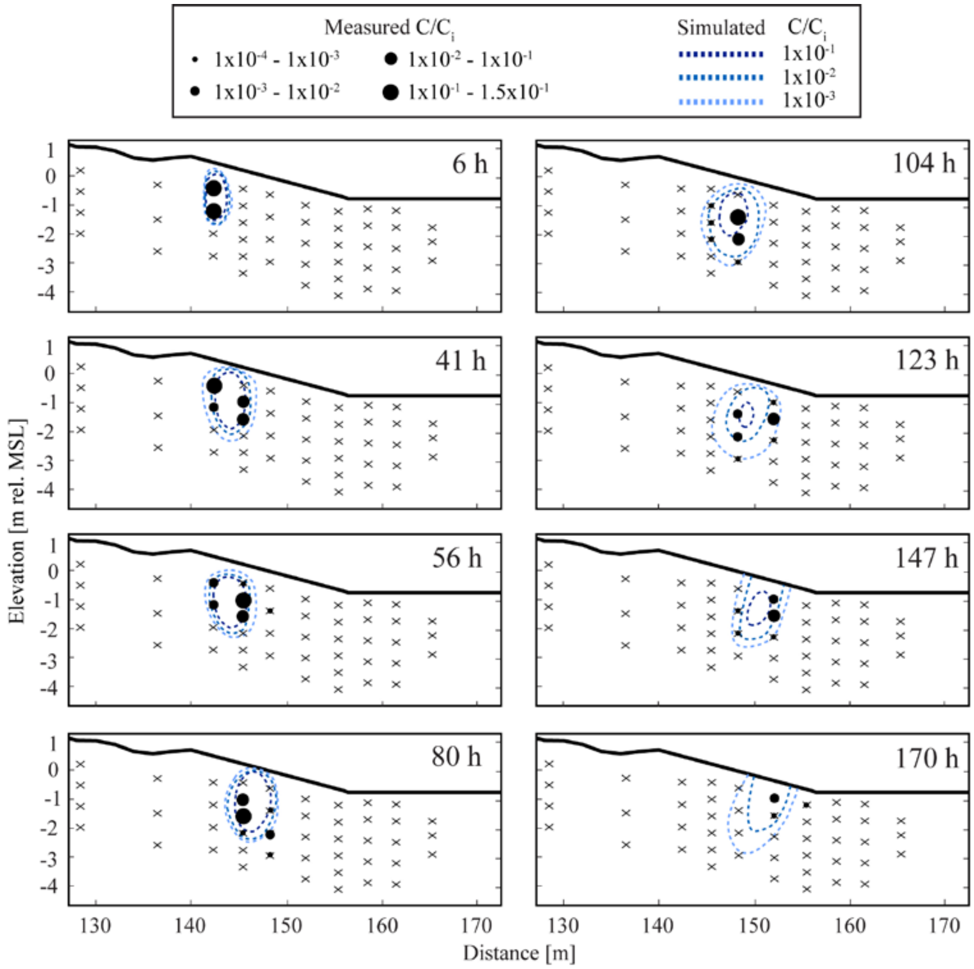

Figure A-1. Measured and simulated tracer plume following injection. The measured and simulated concentrations (C) are normalized to the injection concentration (C_i).

Appendix B

SUPPLIMENTARY MATERIAL FOR CHAPTER 4

A.1 Introduction

This supplementary material contains text and Figures describing relationships between physical characteristics of the beach and flow system to nitrate and sulfate removal. The text and Figures may help readers gain a better understanding of the complexity of the interactions between the physical and biogeochemical processes occurring in the intertidal mixing zone.

A.2 Calculation of Physical Characteristics

a) Tidally-driven circulation was calculated as the total volume of seawater infiltrating across the beachface landward of the low tide mark per tidal cycle.

b) As shown in the main text, the Damköhler (*Da*) number was calculated as:

$$Da = k_{fox} * V_s/Q_i$$

c) The saline plume salinity gradient is the salinity gradient one meter below the sand surface between the freshwater discharge zone and the center of the intertidal circulation cell [*Evans and Wilson*, 2016]

d) The area of the circulation cell was calculated as the cross-sectional area where porewater was between 1 and 35 ppt.

e) The inland hydraulic gradient was calculated as:

$$\frac{dh}{dl} = \frac{Q_f}{K * aquifer\ thickness}$$

f) The perturbation parameter was calculated according to *Robinson et al*., 2007 and *Greskowiak*, 2016:

$$e = \frac{A}{S_b}\sqrt{\frac{n_e \omega}{2KB}}$$

where A is the tidal amplitude, S_b is the slope of the beach, ω is the tidal frequency, K is hydraulic conductivity, and B is the aquifer thickness.

g) The pi number was calculated according to *Greskowiak*, 2016:

$$\pi = \frac{K\Delta\rho}{q_f \rho_f}$$

where K is the hydraulic conductivity, $\Delta\rho$ is the difference of the specific densities of freshwater ρ_f and ρ_s saltwater, and $q_f$is the mean Darcy flux in the reaction zone.

h) The ratio of the tidal amplitude to size of the mixing zone. The size of the mixing zone is defined as the cross-sectional area between 1 and 10 ppt.

i) Ratio of freshwater flux to mixing zone size.

j) The Darcy velocity in the reaction zone was calculated using the mean Darcy velocity in the reaction zone.

A.3 Relationships Between Physical Characteristics and Solute Removal

Numerous physical characteristics and non-dimensional parameters published in literature were compared to the percent of NO_3^- and SO_4^{2-} removed and total NO_3^- and SO_4^{2-}removed. Of the 10 relationships tested for denitrification, the relationship between mixing zone area and percent of nitrate removed, and the relationship between Darcy velocity and total nitrate removed provided the best correlation (see main text). The same set of physical characteristics and non-dimensional parameters compared with sulfate removal show that total sulfate removed can be roughly inferred from the size of the circulation cell, the Da number, and tidally-driven circulation (see main text). The remaining relationships were less reliable indicators of nitrate and sulfate removal (Figures B1-B4).

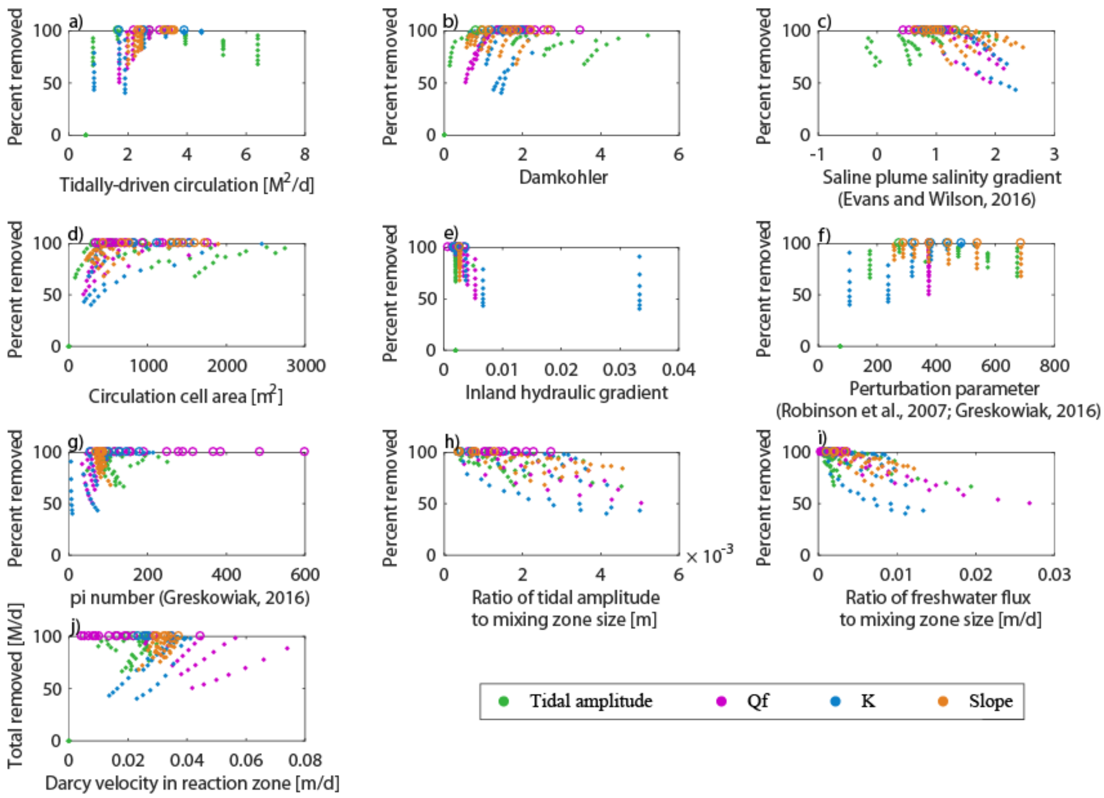

Figure B-1. Percent removed for a suite of physical and non-dimensional numbers. Open circles indicate simulations with 100% removal.

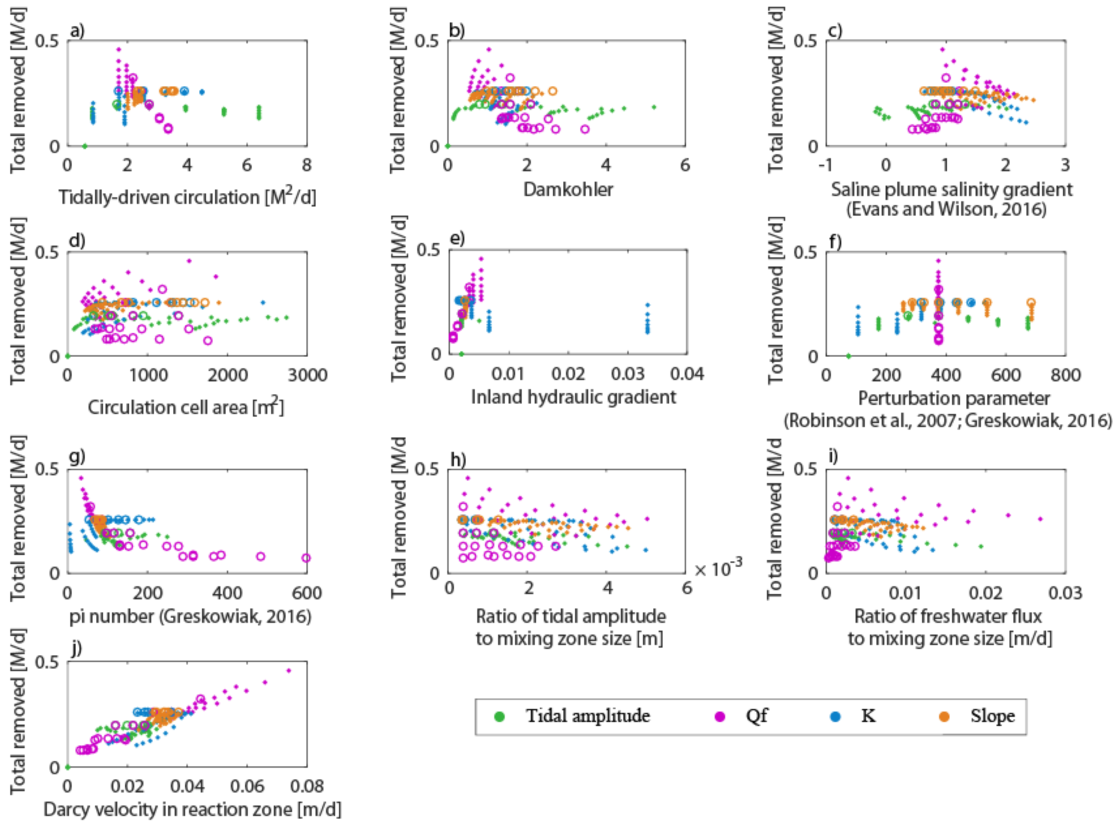

Figure B-2. Total nitrate removed for a suite of physical and non-dimensional numbers. Open circles indicate simulations with 100% removal.

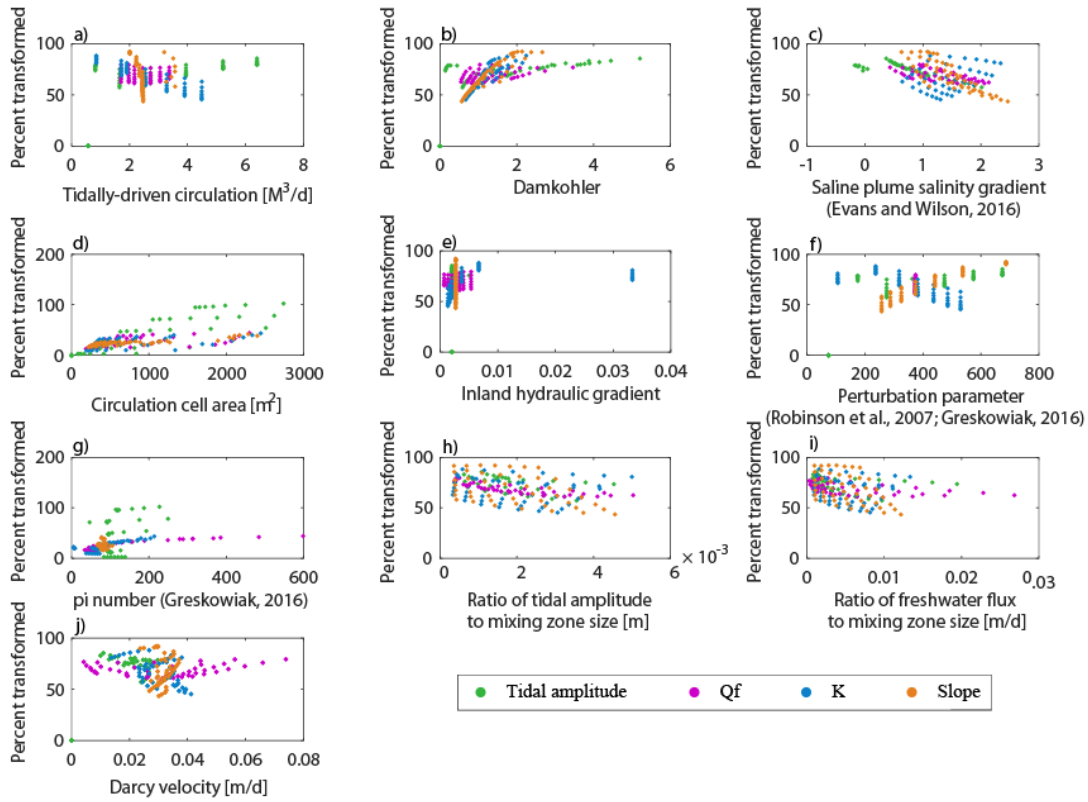

Figure B-3. Percent sulfate transformed for a suite of physical and non-dimensional numbers.

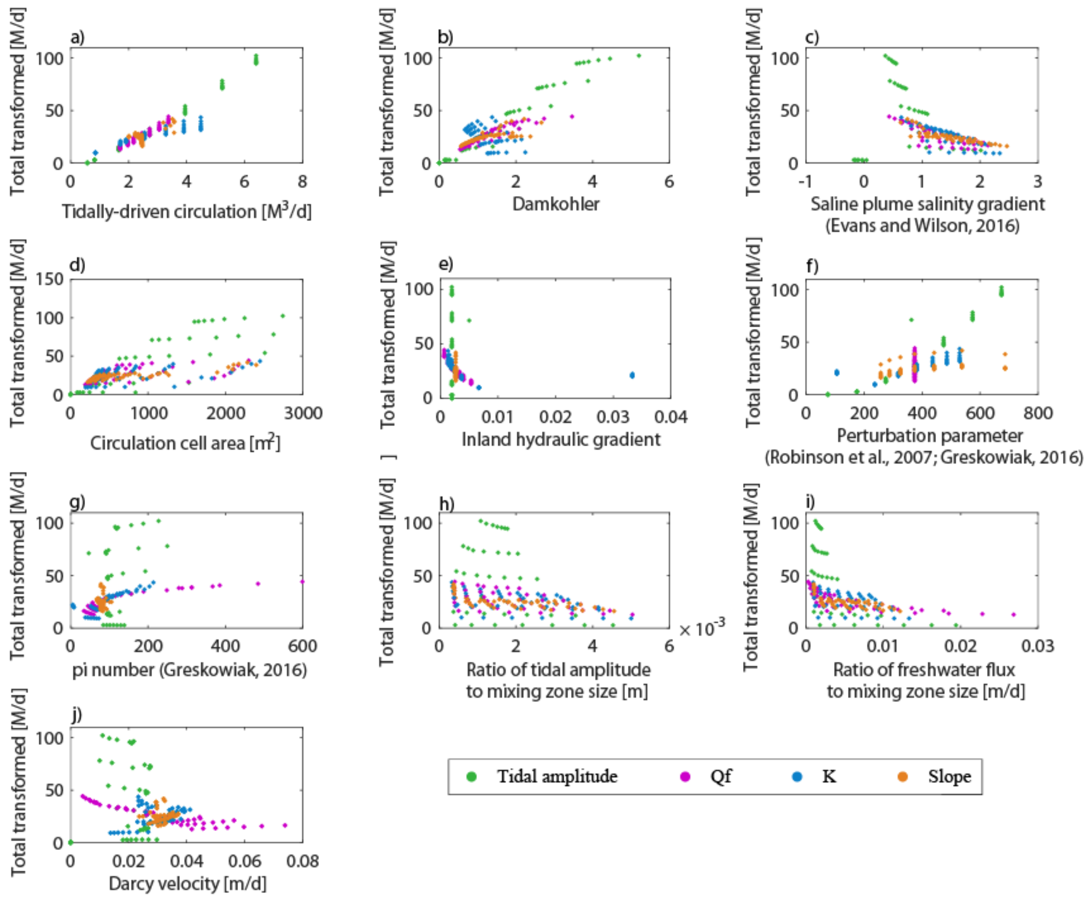

Figure B-4. Total sulfate transformed for a suite of physical and non-dimensional numbers.

Appendix C

COPYRIGHT INFORMATION

Chapter 2 is reproduced with permission from Heiss, J. W., and H. A. Michael (2014), Saltwater-freshwater mixing dynamics in a sandy beach aquifer over tidal, spring-neap, and seasonal cycles, *Water Resources Research*, 50, 6747–6766, doi:10.1002/2014WR015574.

Chapter 3 is reproduced with permission from Heiss, J. W., J. A. Puleo, W. J. Ullman, and H. A. Michael (2015), Coupled surface-subsurface hydrologic measurements reveal infiltration, recharge, and discharge dynamics across the swash zone of a sandy beach, *Water Resources Research*, 51, 8834–8853, doi:10.1002/2015WR017395.

JOHN WILEY AND SONS LICENSE
TERMS AND CONDITIONS

Jan 18, 2017

License Number	4013180092179
License date	Dec 20, 2016
Licensed Content Publisher	John Wiley and Sons
Licensed Content Publication	Water Resources Research
Licensed Content Title	Saltwater-freshwater mixing dynamics in a sandy beach aquifer over tidal, spring-neap, and seasonal cycles
Licensed Content Author	James W. Heiss,Holly A. Michael
Licensed Content Date	Aug 21, 2014
Licensed Content Pages	20
Type of use	Dissertation/Thesis
Requestor type	Author of this Wiley article
Format	Electronic
Portion	Full article
Will you be translating?	No
Title of your thesis / dissertation	WAVE, TIDAL, AND SEASONAL DYNAMICS OF GROUNDWATER FLOW, SALTWATER-FRESHWATER MIXING, AND REACTIVE TRANSPORT IN BEACH AQUIFERS
Expected completion date	Jan 2017
Expected size (number of pages)	200
Requestor Location	James W Heiss 255 Academy St NEWARK, DE 19711 United States Attn: James W Heiss
Publisher Tax ID	EU826007151
Billing Type	Invoice
Billing Address	James W Heiss 255 Academy St NEWARK, DE 19711 United States Attn: James W Heiss
Total	0.00 USD

JOHN WILEY AND SONS LICENSE
TERMS AND CONDITIONS

Jan 18, 2017

License Number	4013180306102
License date	Dec 20, 2016
Licensed Content Publisher	John Wiley and Sons
Licensed Content Publication	Water Resources Research
Licensed Content Title	Coupled surface-subsurface hydrologic measurements reveal infiltration, recharge, and discharge dynamics across the swash zone of a sandy beach
Licensed Content Author	James W. Heiss,Jack A. Puleo,William J. Ullman,Holly A. Michael
Licensed Content Date	Nov 6, 2015
Licensed Content Pages	20
Type of use	Dissertation/Thesis
Requestor type	Author of this Wiley article
Format	Electronic
Portion	Full article
Will you be translating?	No
Title of your thesis / dissertation	WAVE, TIDAL, AND SEASONAL DYNAMICS OF GROUNDWATER FLOW, SALTWATER-FRESHWATER MIXING, AND REACTIVE TRANSPORT IN BEACH AQUIFERS
Expected completion date	Jan 2017
Expected size (number of pages)	200
Requestor Location	James W Heiss 255 Academy St NEWARK, DE 19711 United States Attn: James W Heiss
Publisher Tax ID	EU826007151
Billing Type	Invoice
Billing Address	James W Heiss 255 Academy St NEWARK, DE 19711 United States Attn: James W Heiss
Total	0.00 USD

Figure C-1. Copyright licenses.